Optical Metasurfaces Based on Nano-scale Dielectric Resonators

by

Chengjun Zou

B Eng (Electrical and Electronic Engineering, First Class Honours),
The University of Adelaide, 2012

B Eng (Electrical Engineering and Automation),
China University of Mining and Technology, 2013

Thesis submitted for the degree of

Doctor of Philosophy

in

School of Electrical & Electronic Engineering
Faculty of Engineering, Computer & Mathematical Sciences
The University of Adelaide

2017

Supervisors:

Prof. Christophe Fumeaux, School of Electrical & Electronic Engineering

Dr. Withawat Withayachumnankul, School of Electrical & Electronic Engineering

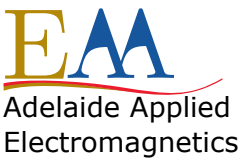

Contents

Abstract

This thesis summarises my PhD research towards applying nano-scale dielectric resonators (DRs) to optical metasurfaces for achieving various functionalities, high efficiency, and reconfigurability. Additionally, the thesis also provides brief introductions to dielectric resonator antennas, plasmonics, and a short review of optical metasurfaces. The major contributions are briefly summarised as follows:

In Chapter 3, resonance properties of cylindrical nano-scale DRs on metallic substrates are analysed. At optical frequencies, subwavelength DRs with metallic substrates can support horizontal magnetic dipole resonance, which can be used for efficient coupling of surface plasmons. However, two types of resonance breakdown can occur in such DRs, and the cause for both types are analysed in detail. Of particular interest is the negatively-matched resonance breakdown, which occurs when real parts of the permittivities of a DR and its metallic substrate are negatively matched. The negatively-matched resonance breakdown is undesired for optical metasurfaces and can be avoided by inserting a low-permittivity dielectric spacer between the DR and its metallic substrate.

In Chapter 4, unidirectional launching of surface plasmons based on non-uniform arrays of DRs is proposed and investigated. By comparing the principles of DR-based anomalous reflection and surface plasmon unidirectional launching, it is concluded that the optimal launching can be achieved by avoiding the first-order diffraction. The optimal launching condition is verified with numerical simulations and linear array theory.

In Chapter 5, a narrowband plasmonic absorber made of a uniform array of nano-scale DRs on metallic substrates is experimentally demonstrated at visible frequencies. It relies on the surface plasmon standing waves coupled by the locally resonant nano-scale DRs for the high absorption. The simulation and measurement results are presented and analysed with coupled mode theory.

In Chapter 6, a mechanically tunable DR metasurface is experimentally demonstrated at visible frequencies. The tunable metasurface is realised by embedding a uniform array of DRs into an elastomeric encapsulation. The transmission responses of the metasurface can be tuned when the encapsulation is deformed with an external strain.

Measurement results confirm the predictions of simulations and shows a remarkable tuning range. A Lagrangian model is developed to rigorously analyse the simulation and measurement results. Such a design provides a preliminary concept usable in reconfigurable optical devices, and after further development can also be potentially commercialised for smart contact lenses.

In Chapter 7, metasurfaces made of metal-loaded DR arrays are proposed to realise the functionality of selective thermal emission. Two metasurface designs are presented. The first design is based on a uniform array of square metal-loaded DRs, which are made of doped silicon. Theoretical and numerical analysis demonstrate stable emission peaking at nearly 8 μm across a wide temperature range. The second further-developed thermal emission metasurface is designed to have broadband emission from 8 to 13 μm atmosphere window range and low emission at all other wavelengths. In this way, it can realise the function of radiative cooling.

These studies along with corresponding simulations or experimental validations demonstrate various functionalities can be realised with DR metasurfaces at optical frequencies. Furthermore, these nanostructure designs suggest a promising route for achieving the next generation highly-efficient integrated optical systems based on nano-scale DRs.

Originality Declaration

I certify that this work contains no material which has been accepted for the award of any other degree or diploma in my name, in any university or other tertiary institution and, to the best of my knowledge and belief, contains no material previously published or written by another person, except where due reference has been made in the text. In addition, I certify that no part of this work will, in the future, be used in a submission in my name, for any other degree or diploma in any university or other tertiary institution without the prior approval of the University of Adelaide and where applicable, any partner institution responsible for the joint-award of this degree.

I give consent to this copy of the thesis, when deposited in the University Library, being available for loan, photocopying, and dissemination through the library digital thesis collection, subject to the provisions of the Copyright Act 1968.

I also give permission for the digital version of my thesis to be made available on the web, via the Universitys digital research repository, the Library Search and also through web search engines, unless permission has been granted by the University to restrict access for a period of time.

April 16, 2017

Signed Date

Acknowledgments

I would like to express my deep gratitude to my supervisors Prof. Christophe Fumeaux and Dr. Withawat Withayachumnankul. Prof. Fumeaux accepted me as a PhD student in the Applied Electromagnetic Group in April 2013, when I just completed my undergraduate study in electrical engineering with little knowledge of optics and nanophotonics. Since then, Prof. Fumeaux has been very patiently guiding me into the research of nanophotonics and taught me how to carry out optical experiments step by step. We had meetings weekly, from which not only I gained deeper understandings of my research field, but also I learnt the methods of and a rigourous altitude towards research. Prof. Fumeaux has been always very supportive for anything that improve my expertise on nanophotonics. He detailedly corrected my manuscripts, encouraged me to give seminars, supported me to attend conferences and apply for scholarships. His comprehensive knowledge, extensive experiences, and rigorous altitudes towards research have always inspired me. Dr. Withayachumnankul is my co-supervisor and an outstanding scholar with broad knowledge in terzhertz technology, plasmonics, and metamaterials. I often would come to Dr. Withayachumnankul's office when I had queries on my research projects and many of our discussions turned out to be the contents in this thesis. He always pointed out critical places in our discussions and encouraged me to go to fundamentals of any problems I met. He patiently corrected all my manuscripts and emphasised the need to write with rigorous arguments. The responsible care and guidance from my supervisors have impacted me deeply and transformed me from a curious student to a researcher. I treasure my PhD study under their supervision and our friendship forever.

I also would like to thank the Functional Materials and Microsystem Research Group (FMM), led by Assoc. Prof. Madhu Bhaskaran and Assoc. Prof. Sharath Sriram in RMIT University. They carried out the nanofabrication of all my metasurface designs and provided valuable suggestions. I would like to thank Assoc. Prof. Madhu and Assoc. Prof. Sharath for hosting me for a three-month research visit in RMIT University. I want to thank Dr. Philipp Gutruf from FMM for valuable discussions and taking most of the fabrication tasks. I want to thank Ms. Shruti Nirantar from FMM for patiently training me of photolithography and with Dr. Guanghui Ren for carrying out the fabrication of the radiative cooling metasurface.

I want to thank for the support and help from my friends and colleagues in our Applied Electromagnetics Group at the University of Adelaide, Dr. Thomas Kaufmann, Dr. Longfang Zou, Dr. Zhi Xu, Dr. Pouria Yaghmaee, Dr. Ali Karami Horestani, Dr. Zahra Shaterian, Dr. Tiaoming Niu, Dr. Amir Ebrahimi, Dr. Fengxue Liu, Dr. Cheng Zhao, Weixun Wu, Shengjian Chen, Nghia Nguyen, Sree Pinapati, Wendy Suk Ling Lee, Andrew Udina and Deshan Govender. I enjoyed the time of our group meetings and discussions. I also would like to acknowledge help from my colleagues and friends in the School of Electrical and Electronic Engineering, Prof. Chen-Chew Lim, Dr. Brian W-H Ng, Dr. Yuexian Wang, Mr. Daniel Headland, Mr. Peng Wang, Mr. Yansong Gao, Mr. Henry Ho, Mr. Stephen Guest, Mr. Mark Innes, Mr. Pavel Simcik, Mr. David Bowler, Mrs. Rose-Marie Descalzi and Mrs. Laura McNamara.

I would like to acknowledge The University of Adelaide for providing me the Adelaide Graduate Research Scholarship for the completing my PhD studies, and thank the funding support from the Australian Nanotechnology Network for my research visiting to RMIT University.

Last but not least, my deep gratefulness and love goes to my mother and father, who always love and encourage me to be confident of myself and be brave to face any challenges. Their infinite support enables me to complete my study. No words can express my love to them.

Thesis Conventions

The following conventions have been adopted in this Thesis:

Typesetting

This document was compiled using LaTeX2e. TeXnicCenter was used as text editor interfaced to LaTeX2e. Inkscape 0.92.1 was used to produce schematic diagrams and other drawings.

Spelling

Australian English spelling conventions have been used, as defined in the Macquarie English Dictionary (A. Delbridge (Ed.), Macquarie Library, North Ryde, NSW, Australia, 2001).

Referencing

The Harvard style is used for referencing and citation in this thesis.

System of Units

The units comply with the international system of units recommended in an Australian Standard: AS ISO 1000-1998 (Standards Australia Committee ME/71, Quantities, Units and Conversions 1998).

Publications

Journals

Zou C., Withayachumnankul W., Shadrivov I. V., Kivshar Y. S., and Fumeaux C. (2015). Directional excitation of surface plasmons by dielectric resonators, *Physical Review B*, 91(8), art. no. 085433.

*Gutruf P., ***Zou C.**, Withayachumnankul W., Bhaskaran M., Sriram S., and Fumeaux C. (2016). Mechanically tunable dielectric resonator metasurfaces at visible frequencies, *ACS Nano*, 10(1), pp. 133–141. (*Equal contribution)

Zou C., Gutruf P., Withayachumnankul W., Zou L., Bhaskaran M., Sriram S., and Fumeaux C. (2016). Nanoscale TiO_2 dielectric resonator absorbers, *Optics Letters*, 41(15), pp. 3391–3394.

Conferences

Zou C., Withayachumnankul W., Zou L., and Fumeaux C. (2014). Plasmonic Absorber Based on Nano-scale Dielectric Resonator Antennas, in *Light, Energy and the Environment*, Canberra, 2014, OSA Technical Digest (online), paper JW6A-24.

Fumeaux C., **Zou C.**, Withayachumnankul W., Zou L., Bhaskaran M., and Sriram S. (2015). Nano-scale dielectric resonator antennas as building blocks for efficient manipulation of light, in *2015 IEEE International Symposium on Antennas and Propagation & USNC/URSI National Radio Science Meeting*, Vancouver, pp.603–604.

Zou C., Withayachumnankul W., Zou L., and Fumeaux C. (2015). Resonance breakdown of dielectric resonator antennas on ground plane at visible frequencies, *Proc. SPIE Micro+Nano Materials, Devices, and Systems*, 9668(966820).

Zou C., Gutruf P., Withayachumnankul W., Zou L., Bhaskaran M., Sriram S., and Fumeaux C. (2016). Dielectric resonator metasurfaces at visible wavelengths, In *International Conference on Nanoscience and Nanotechnology (ICONN)* Canberra, Australia, 2016.

FUMEAUX C., **ZOU C.**, HEADLAND D., NIRANTAR S., GUTRUF P., ZOU L., BHASKARAN M., SRIRAM S., AND WITHAYACHUMNANKUL W. (2016). Terahertz and optical dielectric resonator antennas: Potential and challenges for efficient designs, in *2016 10th European Conference on Antennas and Propagation (EuCAP)*, Davos, Switzerland, pp. 99–102.

List of Figures

List of Tables

Chapter 1

Introduction

AS the start of the thesis, this chapter briefly discusses the concept of optical metasurfaces for light manipulation. Based on the discussion, the motivation of this thesis is presented. The chapter also presents the structure of the thesis and summarises the original contributions.

1.1 Introduction and motivation

The research in optics and photonics has been significantly contributing to progress in the world we live in today. From household gadgets to high-technology industries, research in optics and photonics has created tremendous applications in telecommunications, manufacturing, renewable energy, sensing, biomedical engineering and so on. As an important aspect, nanophotonics research combines nanotechnology and photonics so as to study light-matter interactions at the nanometre scale (Prasad 2004, Kirchain and Kimerling 2007). As famously stated by Feynman (1960) "there's plenty of room at the bottom". By expanding the dimension into the nano-scale, nanophotonics can provide both challenges for fundamental scientific research and new technologies that are more compact, energy-efficient, environmentally-safe, and fast-responding (Prasad 2004). In the current research in nanophotonics, a key objective is to achieve efficient subwavelength light manipulation. Realising this objective promises a number of new exciting applications in areas such as imaging (Ni *et al.* 2013), sensing (Yang *et al.* 2014a), telecommunication, and computation based on integrated photonics (Shalaev and Kawata 2006).

Conventionally, light manipulation relies on bulky optical components such as lenses and waveplates. As exemplified in Fig. 1.1(a), light can be focused by a convex lens according to the Fermat's Principle (Saleh *et al.* 1991). By using lenses, light wavefronts are shaped in a propagation distance that are much greater than a wavelength, and essentially, the process is diffraction-limited. Consequently, both the operation principle and the size of bulky components create an impassable obstacle to apply conventional optical components to light manipulation at the micro- or nano-scale.

In the recent decade, research in optical nanostructures, especially metamaterials, has provided a new route of subwavelength light manipulation. Optical metamaterials are artificial materials with engineered optical properties. They are usually composed of periodically arranged subwavelength resonators (Cai and Shalaev 2010) and have enabled a number of new physical phenomena such as negative refraction (Smith *et al.* 2004), perfect lens (Pendry 2000), and invisible cloaking (Cai *et al.* 2007a). However, due to the structure complexity, the fabrication processes of metamaterials are expensive and time-consuming. Moreover, optical metamaterials usually are highly dissipative and dispersive. These limitations are difficult to overcome, making optical metamaterials still currently impractical to real-world applications. Since 2011, the concept

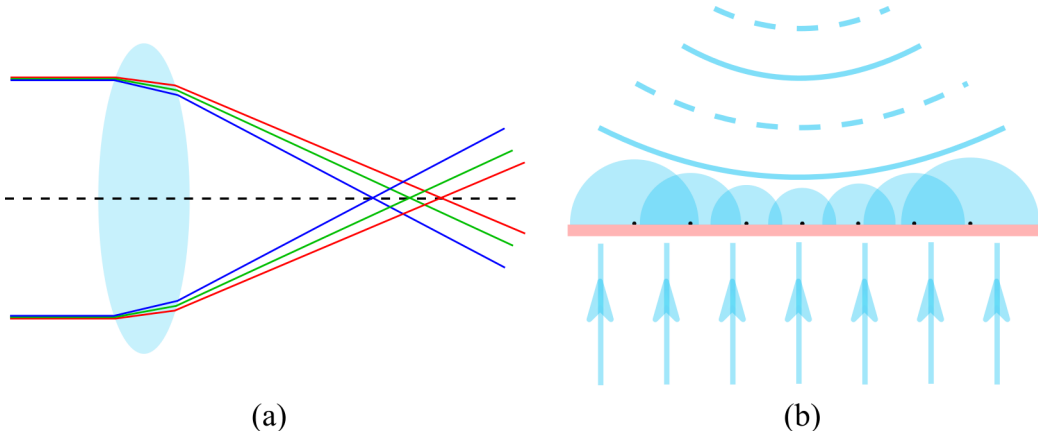

Figure 1.1. Concepts of conventional lens and metasurface lens. (a) An illustration of conventional convex lens that focuses light by accumulative phase difference over a propagation distance. Aberration is unavoidable. (b) A metasurface flat lens that shapes the wavefront by local progressive phase gradients.

of two-dimensional (2D) metamaterial, i.e. optical metasurfaces, has attracted significant research interests. Optical metasurfaces are artificial 2D sheet materials made of periodic subwavelength resonators (Yu *et al.* 2011). Different from three-dimensional (3D) metamaterials, the fabrication cost and complexity are significantly reduced due to the reduced dimension, which renders metasurfaces more realistically attainable than metamaterials for practical applications.

Figure 1.1(b) conceptually present a flat focusing lens metasurface. Different from the conventional lens in Fig. 1.1(a), the optical metasurface flat lens can induce local progressive phase gradients using resonant elements to shape the wavefront. According to Yu *et al.* (2011), metasurfaces generally show three distinctive features. Firstly, the wavefront shaping is accomplished within a subwavelength distance in the propagation direction. Secondly, the periodic nanostructure of metasurfaces enable us to engineer the spatial amplitude, phase and polarisation responses. And thirdly, metasurfaces support strong interactions between nano-scale objects and the electric or magnetic components of the incident waves. These features greatly promote the development of and enable new applications in controlling light-matter interactions in the subwavelength domain.

So far, most of the reported optical metasurfaces have been based on metallic resonators (Yu *et al.* 2011, Sun *et al.* 2012b, Sun *et al.* 2012a), as influenced by the strong research momentum of plasmonic nanostructures and metallic resonator metamaterials in the recent decade. For instance, Fig. 1.2(a) presents the firstly-reported anomalous transmission metasurfaces made of V-shape gold resonators at telecommunication wavelength

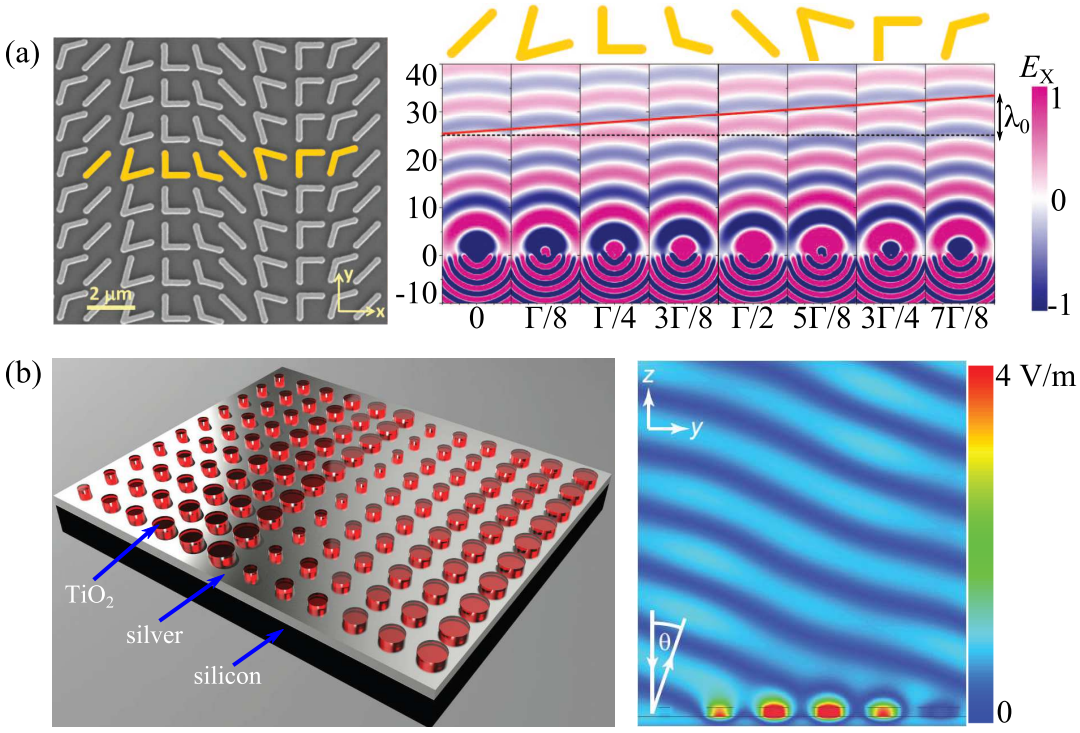

Figure 1.2. Metallic resonator metasurface and dielectric resonator metasurface. (a) Anomalous transmission (refraction) metasurface based on V-shape metallic resonators (Yu *et al.* 2011). (b) Anomalous reflection metasurface based on dielectric resonators (Zou *et al.* 2013).

(Yu *et al.* 2011). The V-shape resonators can demonstrate symmetric and asymmetric electric resonances and their sizes are at around half of the resonance wavelengths. By changing the opening angle and the orientation of a V-shape resonator, a 2π phase range, tunable amplitude and polarisation state of the transmitted light can be achieved. Properly arranging the local phases (i.e. V-shape resonators) can result an anomalous refraction wavefront as shown in the right graph of Fig. 1.2(a). Although adopted by many researchers in various metasurface designs, metallic resonators have certain disadvantages that limit their performance. Free electron oscillations in metals at optical frequencies lead to strongly plasmonic loss. To see this intuitively, Fig. 1.3 plots the dielectric function based on Drude-model of silver and the corresponding skin depth from 1 THz to 500 THz. As the frequency increases from terahertz to the infrared, and to the visible range, though the calculated skin depth reduced from 85 nm to nearly 25 nm, the ratio between the skin depth and its corresponding wavelength increased by two orders of magnitude. The results imply a significantly increased dissipation of electric energy in metals from terahertz to visible frequencies, and such a high dissipation is

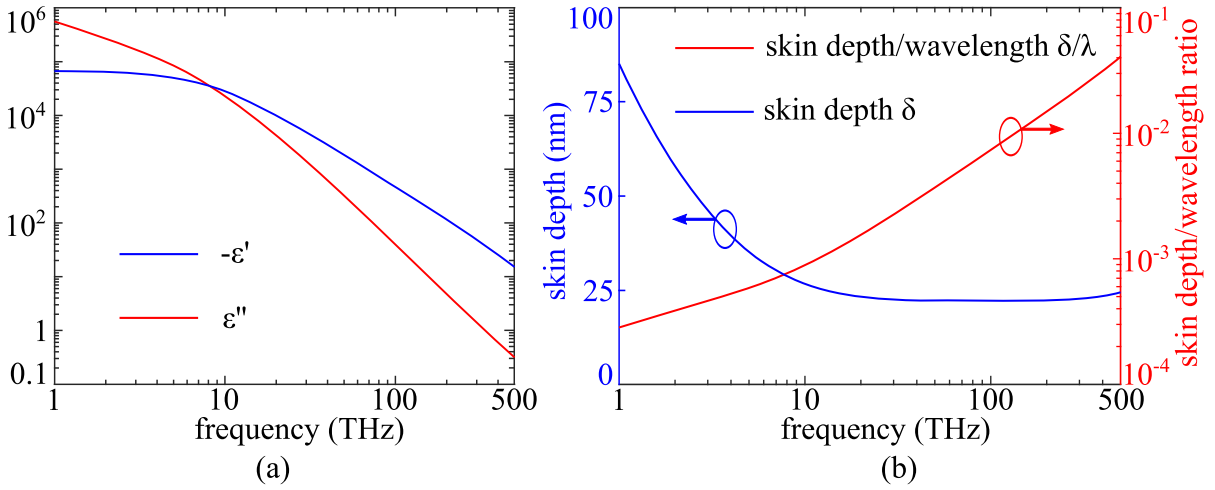

Figure 1.3. Silver permittivity based on Drude model and calculated skin depth. (a) Real part (absolute value for logarithmic plotting purpose) and imaginary part of silver permittivity based on Drude-model (Thoreson *et al.* 2010). (b) The calculated skin depth ($1/e$ decay of E-field amplitude) and ratio of skin depth to wavelength.

undesired for high-efficiency operation of optical metasurfaces. Additionally, different resonant modes cannot be efficiently supported by metallic resonators of simple structures. For instance, magnetic resonances can only be supported by stacked metallic resonators with dielectric spacers, thus yielding high fabrication costs. These problems have largely limited the potential of optical metasurfaces in terms of functionalities and practical applications.

To extend the functionalities of optical metasurfaces towards real-world applications, efficiency is of critical importance. In the recent past, research efforts were invested on improving metal quality (Biagioni *et al.* 2012, Wild *et al.* 2012) to reduce loss or introducing gain materials (Stockman 2011) to balance the plasmonic loss. However, the effects on improving efficiency are limited and are not conveniently adopted into different designs. In the recent years, the concept of nano-scale dielectric resonators (DRs) (Zou *et al.* 2013) was suggested as a promising route to high-efficiency optical nanostructures. Low-loss dielectric materials operate via displacement current, making them virtually free from plasmonic loss. Moreover, DRs with low-loss and moderate permittivities ($\epsilon_r > 5$) can efficiently support various orders of Mie resonances at optical frequencies (Kuznetsov *et al.* 2012, Evlyukhin *et al.* 2012). Based on this concept, Zou *et al.* (2013) demonstrated an anomalous reflection metasurface made of cylindrical TiO_2 DRs on a silver substrate at 633 nm, as presented in Fig. 1.2(b). TiO_2 offers an average permittivity of around 7.5 and the resonators sizes in the proposed design were

ranging from 66 nm to 264 nm. In this design, the DRs resonate as horizontal magnetic dipole modes, covering a phase range over 300°. Due to the low-loss DRs, the field concentration is largely confined to the dielectric part and thus the loss in the metal part is reduced.

The discussion above outlines the motivation of the thesis, namely to apply low-loss moderate permittivity nano-scale DRs to optical metasurface designs and thereby achieve high operation efficiencies. Additionally, different resonance modes, in particular magnetic resonances, are utilised for different functionalities in various designs. The outline of the thesis structure and a brief summary of each part are presented in Section 1.2.

1.2 Thesis structure

The structure of this thesis is outlined in Fig. 1.4. The thesis consists of eight chapters, which are divided into four parts. **Part I** includes Chapter 1 and Chapter 2. Chapter 1 presents the motivation and an overview of the thesis. Chapter 2 summarises the necessary background knowledge for the investigations described in this thesis. Chapters 3 and 4 (**Part II**) are the theoretical analysis of DR-based nanostructures. Chapters 5 to 7 (**Part III**) present DR-based metasurface designs. Finally, chapter 8 (**Part IV**) concludes the thesis and presents an outlook of optical metasurfaces. The detailed descriptions of Part I, II and III are presented as follows:

Part I - Background presents the motivation and research topic of the thesis in Chapter 1, and provides an introduction of necessary fundamental knowledge in Chapter 2. Chapter 2 includes (i) an introduction to dielectric resonator antennas (DRAs) and their applications from microwave extending to optical frequencies; (ii) an introduction to plasmonics covering the basics of optical properties of metals, surface plasmon polaritons (SPPs) and localised surface plasmon resonances (LSPRs); and (iii) a review of recent research of optical metasurfaces.

Part II - Theoretical work summarises the studies in the thesis based on theoretical and numerical analysis. In this part, Chapter 3 summarises the operation principle of DRs on metallic substrates. It lays out a theoretical foundation for the studies presented in the later chapters of the thesis. Chapter 4 proposes to use non-uniform arrays of nano-scale DRs on metallic substrates for SPP unidirectional launching and studies the optimal launching condition.

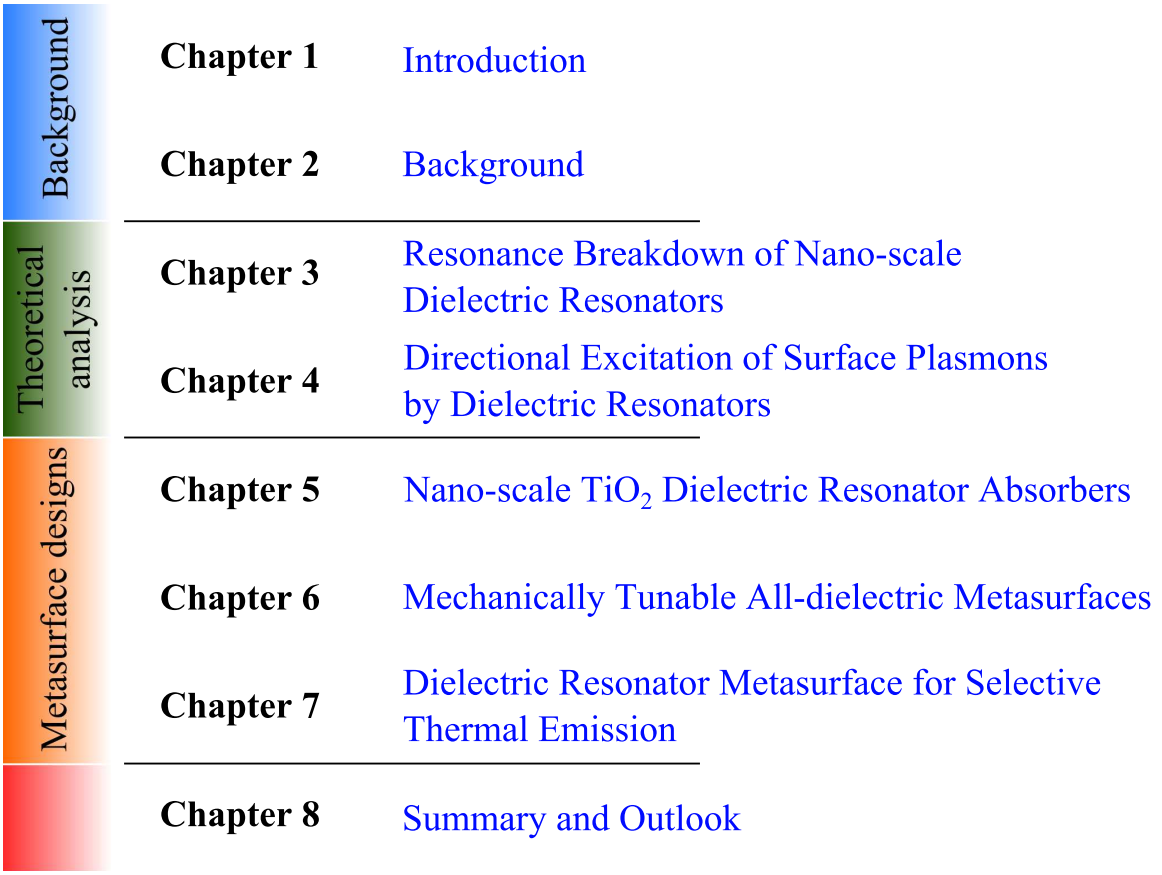

Figure 1.4. Thesis outline. The thesis is composed of eight chapters, which are divided into four parts as background, theoretical analysis, metasurface designs, and conclusion. All chapters are virtually self-contained.

Part III - Metasurface design presents three DR-based metasurface designs including (i) a narrowband plasmonic absorber in Chapter 5, (ii) a mechanically tunable all-dielectric metasurface in Chapter 6, and metasurfaces with selective thermal emission in Chapter 7.

1.3 Summary of original contributions

This thesis involves several original contributions in the field of optical metasurfaces, as declared in this section.

In Chapter 3, the resonance property of nano-scale DRs on a metallic substrate at visible frequencies is analysed in detail. The analysis shows that two types of resonance breakdown can occur. For DRs with very low permittivities, the incident electromagnetic energy can hardly resonate in the DR structure. This is the first type of resonance

breakdown. While for a DR with a high permittivity, if the real part of the permittivity of the DR negatively matches with the real part of the metal permittivity, another negatively-matched resonance breakdown can occur. The study in this Chapter suggests limited operation ranges of DR permittivity and frequency, which is important for designing metallo-dielectric nanostructures at optical frequencies. The content of this Chapter is published in *SPIE Proceeding* **9668**, no. 966820, 2015.

In Chapter 4, nano-scale cylindrical DRs on metallic substrates are proposed for efficient SPP coupling. Non-uniform arrays of such DRs are proposed for SPP unidirectional launching by manipulating SPPs interferences. However, even if designed for SPP unidirectional launching, a non-uniform array of DRs can potentially create diffractions in free space. By examining the principles of diffraction and SPP launching, it is concluded that the optimal SPP coupling and launching can be achieved by avoiding the first-order diffraction. This optimal launching condition is further confirmed with linear array antenna theory. Verification with simulations that compare SPP unidirectional launching with and without the first-order diffraction are presented. The study in this Chapter is published in *Physical Review B* **91**(8), art. no. 085433, 2015.

In Chapter 5, a narrowband plasmonic absorber at 633 nm based on an array of cylindrical nano-scale DRs on a metallic surface is experimentally demonstrated. The simulation and measurement results are analysed with coupled mode theory. The absorption principle is different from existing cavity absorbers based on Fabry-Pérot resonances or on purely localised surface plasmon resonances. Instead, the high absorption relies on the SPP standing waves stimulated by the locally resonant nano-scale DRs. Further studies on the resonator sizes, periodicity, and incident angles in relation to absorption performance are also discussed. The study in this Chapter is published in *Optics Letters* **41**(15), pp. 3391-3394, 2016.

In Chapter 6, a mechanically tunable visible-frequency dielectric resonator metasurface is experimentally demonstrated. Such a tunable metasurface is made by embedding an array of nano-scale TiO_2 DRs into elastomeric material, namely polydimethylsiloxane (PDMS). By applying a uniaxial external strain to the PDMS encapsulation, the near-field interactions among DRs are altered, and thereby reconfigurable electromagnetic properties are achieved. The measurement shows a remarkable tuning range. All the results are rigorously analysed with a Lagrangian model that describe the near-field interactions amongst DRs. Such a design can be used as reconfigurable optical devices in integrated optics, and also has potential for commercial application in smart contact

lenses for filtering out unwanted frequencies. The study in this Chapter is published in *ACS Nano* **10**(1), pp. 133-141, 2016. This study has attracted extensive media coverage soon after publication: Altmetric–`https://wiley.altmetric.com/details/5635929`.

In Chapter 7, metasurfaces for selective thermal emission are proposed based on metal-loaded DRs. Such metasurfaces can be realised by etching phosphorous-doped silicon wafers. As such the structures can be easily integrated with silicon-based photonic devices. In this Chapter, two selective thermal emission metasurfaces are presented. A uniform array of cylindrical metal-loaded DRs demonstrates stable thermal emission peaked at around 8 μm from 300 K to 900 K. The second metal-loaded DR metasurface is designed with the functionality of radiative cooling by realising a broadband power absorption (emission) from 8 to 13 μm, which matches the main infrared atmospheric window. As the atmospheric absorption is minimum in this range, the thermal emission can be maximised and an efficient passive cooling power can be achieved. An experimental validation has been conducted for the second design. This study will be prepared for journal publication in the near future.

Chapter 2

Background

THIS chapter introduces relevant concepts related to the research of this thesis. It starts in the first section with a summary of the basics of dielectric resonator antennas (DRAs), and a description of the scalability and efficiency of DRAs from microwave to optical frequencies. The second section introduces the fundamentals of plasmonics. Plasmonic resonances are mainly supported by metallic nanostructures at optical frequencies, which are directly related to the studies in Chapter 4 and Chapter 5. Finally, the third section reviews existing optical metasurfaces and their functionalities.

2.1 Dielectric resonator antennas (DRAs)

2.1.1 Microwave DRAs

The concept of dielectric resonator antennas (DRAs) utilises the radiation loss of resonators made of low-loss (with typically loss tangent $< 10^{-2}$) dielectric materials with moderate to high permittivities ($5 < \epsilon_r < 100$). The study of radiation properties of DRs can be dated back to 1939, when open dielectric resonators (DRs) were theoretically proven to radiate into free-space (Richtmyer 1939). However, for a very long period afterward, DRs were not used for antenna applications. On the contrary, low-loss and high relative permittivity DRs were shielded by metals and have been used widely in microwave circuits as filters. The first experimentally demonstration and systematic studies of DRAs were reported in 1983 by Long *et al.* (Long *et al.* 1983, McAllister *et al.* 1983, McAllister and Long 1984). Since then, a significant number of studies on DRAs have been reported, particularly for microwave operation. Compared with other types of microwave antennas, DRA offers many advantages (Mongia and Bhartia 1994), as discussed briefly in the following.

Compact size. DRAs are widely used for low-profile and compact antenna designs. The dimensions of a DRA are proportional to $\lambda_0/\sqrt{\epsilon_r}$, where λ_0 is the free-space resonance wavelength of the DRA and ϵ_r is the relative permittivity of the dielectric material. Therefore, compact designs can be achieved by choosing materials with large relative permittivities ($10 < \epsilon_r < 100$) (Kingsley and O'Keefe 1999, Lehmus *et al.* 1999, Wang *et al.* 2006). Many techniques were proposed for compact DRA designs. DRAs are usually combined with a metal ground plane, which can reduce the DRA size by half according to the image theory (Balanis 2016). Another commonly used technique involves partly truncating the DRA structure (Tam and Murch 1999). By carefully removing certain parts of its volume and ensuring proper boundary conditions, a DRA can still resonate efficiently in a particular mode.

High efficiency. As DRAs operate via displacement current, low-loss DRAs are inherently free from conduction loss. This feature promises a high radiation efficiency, and can be especially attractive for millimetre wave (Lai *et al.* 2008, Perron *et al.* 2009), terahertz (Headland *et al.* 2015), and optical antennas (Zou *et al.* 2013), because metallic antennas in these wavelength ranges suffer relatively high loss from conduction.

Convenient coupling. DRAs can be excited with a number of coupling schemes. The most common schemes include coaxial probes (Long *et al.* 1983, McAllister *et al.* 1983,

McAllister and Long 1984), apertures (Ittipiboon *et al.* 1993, Leung *et al.* 1994), microstrip lines (Kranenburg and Long 1988, Leung *et al.* 1997), and coplanar waveguides (Kranenburg *et al.* 1991, Sze *et al.* 2003). The dimensions of a feed can be tuned to match the input impedance of the antenna structure. A coaxial probe introduces an electric current that excites and matches the *E*-field of a particular resonance mode of a DRA. The probe can be put either inside or outside a DRA. Microstrip lines with an aperture or microstrip lines alone are commonly used for excitation when DRAs are loaded onto metal substrates. An aperture can create a virtual horizontal magnetic current to excite a DRA. Microstrip lines have advantage of convenient matching with the DRA input impedance by simply tuning the feeding position. Coplanar waveguides can work as electric monopoles to excite DRAs. There are also many other coupling schemes such as slots and conformal strips. Together with aforementioned coupling schemes, further options are thoroughly discussed in books by Petosa (2007) and Luk *et al.* (2002).

Bandwidth flexibility. DRAs can be realised for either narrowband or wideband applications. The bandwidth of a DRA is inversely proportional to the relative permittivity ϵ_r of the DRA material. Aforementioned compact DRAs made of high ϵ_r dielectrics normally demonstrate narrow bandwidths. On the other hand, wideband DRA designs are usually made of moderate-permittivity (e.g. $\epsilon_r \approx 10$) dielectric materials (Li and Leung 2005, Leung and Leung 2003). There are many bandwidth enhancement techniques. For example, a single DRA can be made of materials with different permittivities

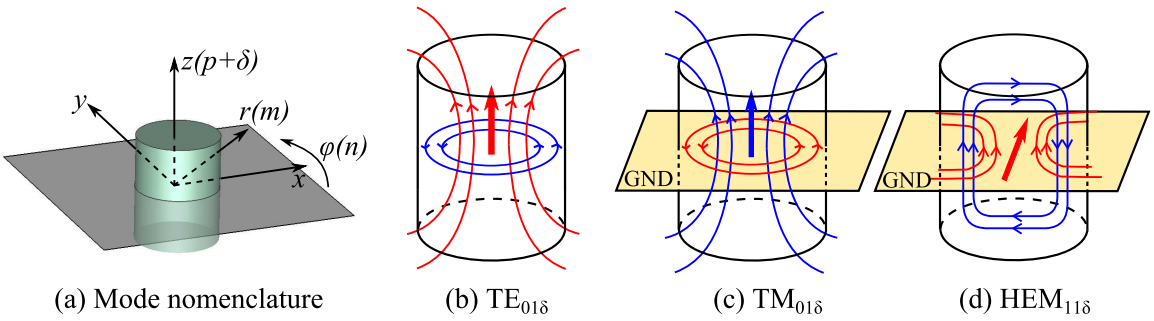

(a) Mode nomenclature (b) $TE_{01\delta}$ (c) $TM_{01\delta}$ (d) $HEM_{11\delta}$

Figure 2.1. Mode nomenclature and fundamental resonance modes of a cylindrical DRA. (a) A cylindrical DRA sitting on a metal ground plane, which creates an image of the DRA. The standard DRA modes nomenclature is illustrated. n, m, and $p + \delta$ denote the sinusoidal variations along the azimuthal (φ), the radial (r), and the vertical (z) directions, respectively. (b-d) Illustration of field distributions of fundamental modes $TE_{01\delta}$, $TM_{01\delta}$, and $HEM_{11\delta}$. Red lines and blue lines denote the magnetic fields and electric fields respectively. The thick arrows indicate the equivalent magnetic (red) or electric (blue) dipoles.

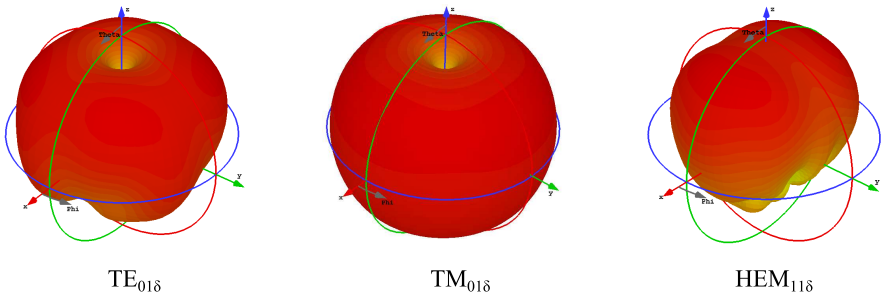

Figure 2.2. Radiation patterns of cylindrical DRAs in $TE_{01\delta}$, $TM_{01\delta}$, and $HEM_{11\delta}$ modes.

stacked together (Kishk *et al.* 1989, Ge *et al.* 2006) or by embedding a DR into another dielectric material (Kishk 2005) to improve the bandwidth. These configurations essentially increase the electrical size of an antenna. The bandwidth can also be improved by using new feeding structures (Chu *et al.* 2009). Moreover, multiple resonances can be combined in a DRA to increase its bandwidth (Almpanis *et al.* 2008).

Multiple resonance modes. DRAs can support multiple resonance modes and each mode has its unique internal field distribution and radiation pattern (Petosa 2007). Therefore, different radiation characteristics can be achieved in one design. The resonance modes of a DRA of canonical shape (hemispherical, cylindrical, rectangular) can be analytically predicted in good accuracy by assuming electric and magnetic wall boundary conditions. In general, three types of resonance modes can be excited in a canonical shaped DRA, and they are TE modes, TM modes and hybrid modes, with respect to the z-axis in Fig. 2.1(a). The standard DRA mode nomenclature was systematically described by Mongia and Bhartia (1994) and is briefly illustrated in Fig. 2.1(a) based on the fundamental modes of a cylindrical DRA.

The resonance modes and corresponding radiation patterns of a cylindrical DRA are very helpful as examples to understand the characteristics of DRAs, as the cylinder is a simple and canonical shape that is amenable to fabrication across a wide range of frequency. For a cylindrical DRA, three fundamental resonance modes can be excited and they are $TM_{01\delta}$, $TE_{01\delta}$, and $HEM_{11\delta}$. Schematics of these fundamental modes are depicted in Fig. 2.1(b-d). It is seen that $TE_{01\delta}$ mode and $TM_{01\delta}$ mode can be viewed as a vertical magnetic dipole and a vertical electric dipole respectively, while $HEM_{11\delta}$ mode resonates as a horizontal magnetic dipole. Radiation patterns of the three fundamental resonance modes excited in a cylindrical DRA on a perfect electric conductor (PEC) substrate (or ground plane) are presented in Fig. 2.2. The $TM_{01\delta}$ mode is usually used for omnidirectional radiation, and the $HEM_{11\delta}$ mode is usually used for broadside

radiation, while the $TE_{01\delta}$ mode has been traditionally used in microwave circuits due to its high Q-factor.

2.1.2 Extending DRA applications to optical frequencies

With the advance in nanofabrication technology, applying DRAs to optical applications can be readily realised nowadays. At optical frequencies, the concept of DRA is usually referred as dielectric resonator (DR). Additionally, at optical frequencies, the resonance modes are typically referred to with Mie resonances. Thereby it is clarified here that the terminology ***dielectric resonator***, or ***DR*** is broadly used when referring to optical applications in this thesis.

Metallic resonators are lossy, and to support magnetic resonances they have to be designed as multilayer structures that are complex for fabrication at optical frequencies. On the contrary, low-loss nano-scale DRs operating via displacement current are virtually free from Ohmic loss and can efficiently support various orders of Mie resonance (Kuznetsov *et al.* 2012, Evlyukhin *et al.* 2012). To illustrate Mie-resonances of nano-scale DRs, Fig. 2.3 presents simulation results of a subwavelength silicon cylindrical DR under a plane-wave excitation. From low to high frequencies, the extinction spectrum of the DR clearly demonstrates magnetic dipole, electric dipole, magnetic quadrupole, and electric quadrupole resonances, which can be well-predicted by calculating the light scattering from a subwavelength particle (Bohren and Huffman 2008) according to Mie theory. The resonance modes are identified by observing the electric and magnetic field distributions, shown in Fig. 2.3(b). By comparing the field distributions in Fig. 2.3(b) to the resonance modes of a microwave DRA in Fig. 2.1, it is found the resonance modes of a DR are similar between the microwave and optical frequencies. To be specific, Mie resonance modes correspond to the hybrid modes of microwave DRAs under symmetrical excitations. Study of the scalability and efficiency of DRAs from microwave to optical frequencies is discussed as the following.

Down-scaling DRA for efficient optical antennas

Optical antennas are analogous to microwave antennas in the sense that both of them convert freely propagating optical radiation into localised oscillating field, and vice versa (Novotny and Van Hulst 2011). The significance of optical antennas is that they greatly enhance the efficiency of nano-scale light manipulation and light-matter interaction (Novotny and Hecht 2012). Although DRs originated at microwave frequencies,

they can be scaled down to the micro- or nano-scales as terahertz or optical antennas. Figure 2.4(a) presents a DR scalability study obtained by simulating a cylindrical DR of a material with fixed permittivity on a silver substrate under a plane-wave excitation (Zou *et al.* 2014). The graph demonstrates the normalised resonance size (D/λ_0) of the DR versus wavelength. It is observed that the DRA shows linear scalability up to terahertz frequencies. However, as the plasmonic effect of the metallic ground plane becomes increasingly stronger for increasing frequency, the corresponding normalised

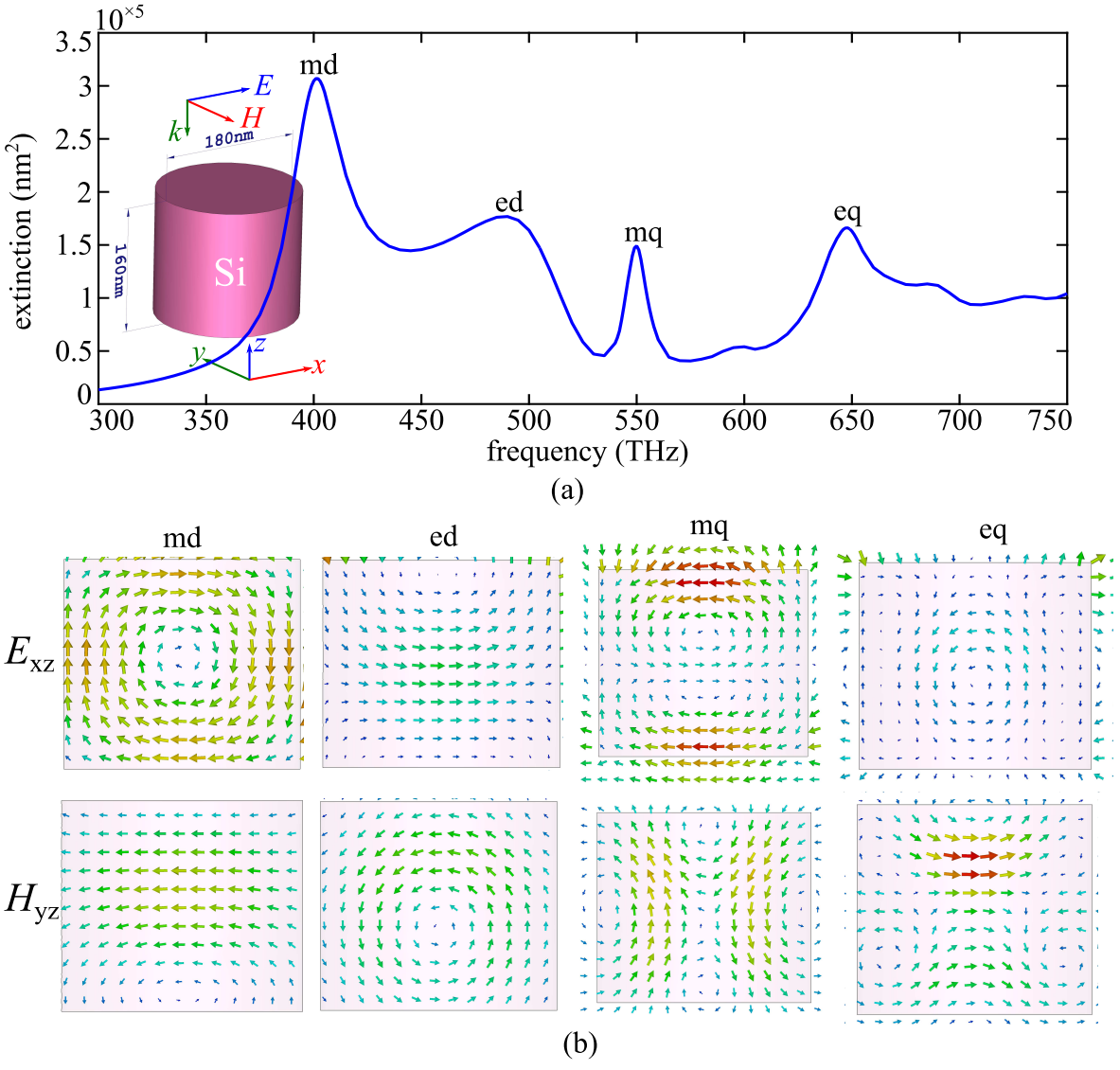

Figure 2.3. Mie-resonance modes of a nano-scale silicon dielectric resonator. (a) Simulated extinction spectrum of a cylindrical Si DR. Magnetic dipole (md), electric dipole (ed), magnetic quadruple (mq), and electric quadruple (eq) resonances are labelled on the curve. (b) The simulated electric (x-y cross-section) and magnetic (y-z cross-section) field distributions of the corresponding resonance modes.

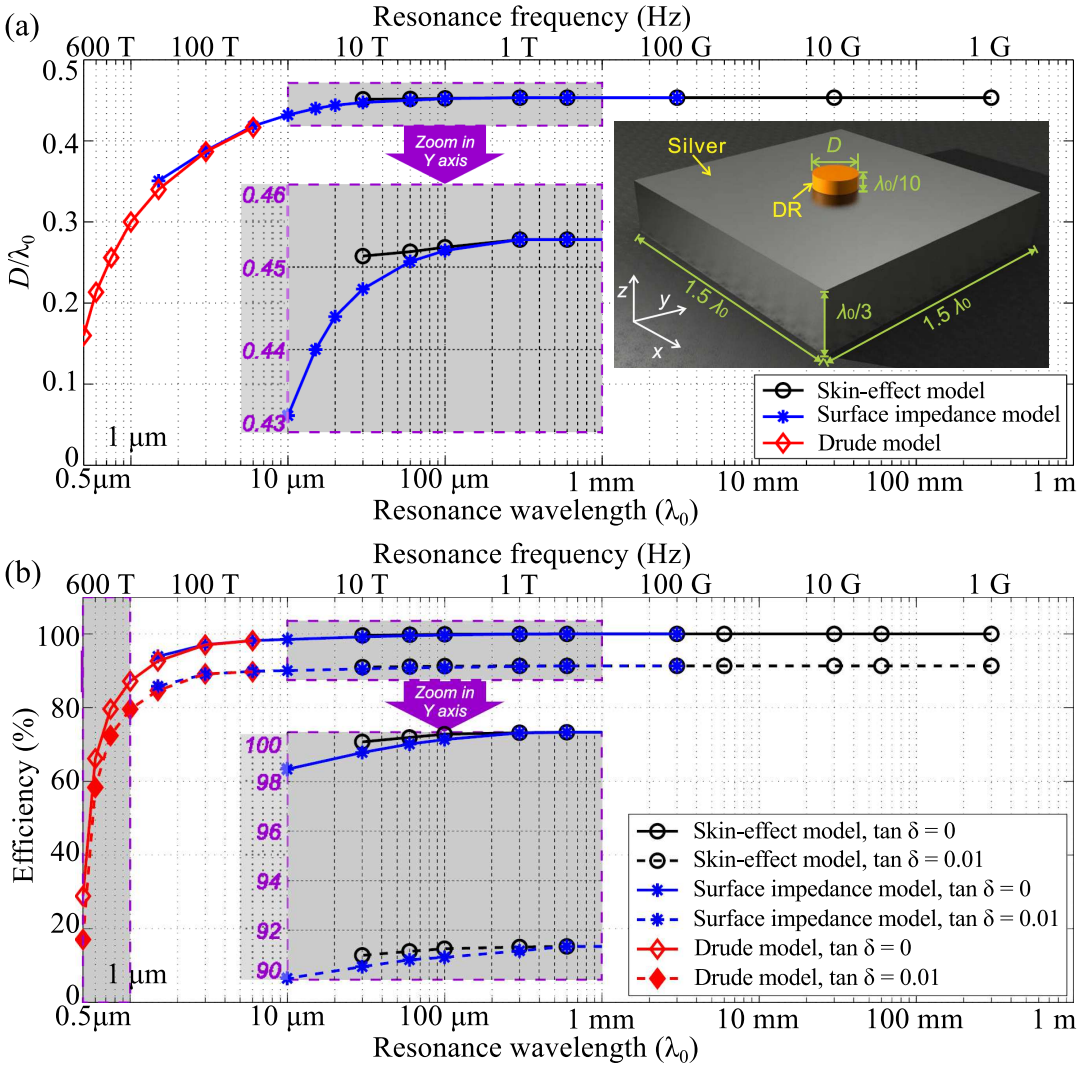

Figure 2.4. DRA scalability and efficiency study. (a) DRA scalability study from microwave to visible frequencies. A TiO_2 DR on a silver substrate is simulated under a plane-wave excitation. The markers indicate the simulated wavelengths. The inset shows the studied DRA structure. (b) DRA efficiency study based on the same structure as in (a). Results adapted from Zou *et al.* (2014).

resonance size decreases. The radiation efficiency was also studied based on the same structure, as presented in Fig. 2.4(b). The radiation efficiency remains higher than 90% up to the wavelength of 10 μm. Even extending into near-infrared and red light frequencies, the radiation efficiency is still relatively high. As plasmonic loss increases towards shorter wavelengths, the radiation efficiency decreases dramatically in the visible range. It can be expected that all-dielectric nanostructures, *i.e.* without a metal ground plane, can demonstrate even higher efficiencies.

2.2 Plasmonics

Plasmonics is closely related to optical metasurfaces. In this thesis, nano-scale DRs are proposed to be integrated into plasmonic nanostructures for reducing loss. Therefore, a discussion of plasmonics can demonstrate the characteristics and appropriate applications of metallic resonators and suggest advantages of nano-scale DRs for the realisation of efficient optical metasurfaces. In this section, an introduction to the basics of plasmonics is presented. In the first part, a brief discussion on the optical properties of metals based on the Drude model is given. The second part introduces the fundamentals of surface plasmon polaritons (SPPs) and localised surface plasmon resonances (LSPRs).

2.2.1 Optical properties of metals described by Drude model

Metals at the microwave range can be considered as nearly PECs where the interaction with electromagnetic waves can be described by the skin effect. This is because free electrons in metals closely follow the oscillation of incident electromagnetic field, and thus the skin depth is very small compared with the wavelength. As a consequence, the induced current disctribution is largely limited to the metal surfaces. However, at optical frequencies, the quasi-PEC assumption is no longer valid. The mass of an electron causes a much stronger damping effect when electrons couple with electromagnetic waves at optical frequencies, and thereby metals become poor conductors. The interaction between metals and electromagnetic waves at optical frequencies can be understood based on the classical framework of Maxwell's equations. Most commonly, the Drude-based complex dielectric function is adopted to describe the optical properties of metals (Drude 1900). In the Drude model, metals are characterised by a cloud of electrons moving under the influence of fixed positive nuclei. Accordingly, the complex permittivity $\epsilon(\omega)$ of a metal can be expressed as Eq. 2.1 based on the time factor $e^{-i\omega t}$ (Grosso and Pastori Parravicini 2000):

$$\epsilon(\omega) = 1 - \frac{\omega_p^2}{\omega^2 + i\gamma\omega}, \tag{2.1}$$

where $\omega_p = \frac{ne^2}{\epsilon_0 m}$ is the plasma frequency, and e is the elementary charge. ω_p is only determined by the number of free carriers n and the effective mass m of the carrier. $\gamma = 1/\tau$ is the collision frequency and τ is the relaxation time. They describe the electron motion damping via collisions. τ is typically on the order of 10^{-14} s at room

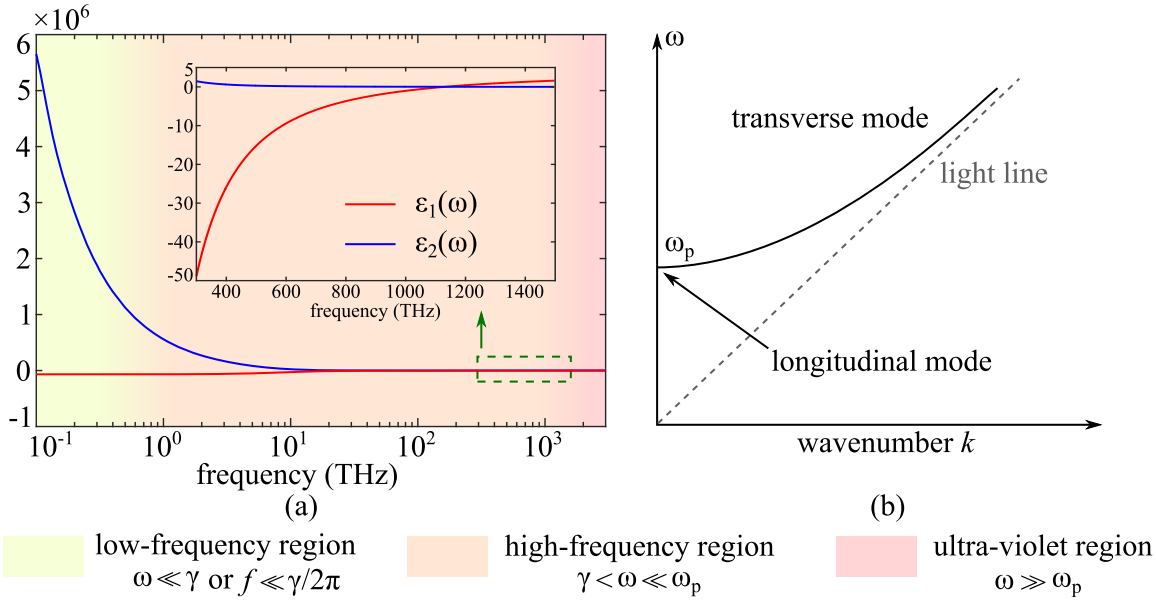

Figure 2.5. Drude model and dispersion curve of silver. (a) The Drude model based complex permittivity of silver. The plasma frequency $f_p = \omega_p/2\pi = 2178$ THz and the collision frequency $\gamma = 5.078$ THz (Thoreson *et al.* 2010). (b) Representation of transverse and longitudinal modes of bulk metal, which is seen as free electron gas.

temperature, and thus γ is around 100 THz. To take the residual polarisation of metals into consideration when ω approaches ω_p, "1" in Eq. 2.1 is usually replaced with ϵ_∞. Therefore, Eq. 2.1 becomes:

$$\epsilon(\omega) = \epsilon_\infty - \frac{\omega_p^2}{\omega^2 + i\gamma\omega}. \tag{2.2}$$

To discuss the optical properties of metals, the Drude-based complex permittivity of noble metal silver is taken as an example, as shown in Fig. 2.5. The model does not consider electron inter-band transitions in silver. According to Eq. 2.2, the real and imaginary parts of $\epsilon(\omega)$ of silver can be expressed as:

$$\epsilon_1(\omega) = \epsilon_\infty - \frac{\omega_p^2\tau^2}{1+\omega^2\tau^2}; \qquad \epsilon_2(\omega) = \frac{\omega_p^2\tau}{\omega(1+\omega^2\tau^2)}. \tag{2.3}$$

In the low frequency region where $\omega\tau \ll 1$ ($\omega \ll \gamma$), Eq. 2.3 approximates as:

$$\epsilon_1(\omega) \approx \epsilon_\infty - \omega_p^2\tau^2; \qquad \epsilon_2(\omega) \approx \frac{\omega_p^2\tau}{\omega}. \tag{2.4}$$

It is seen that the real part $\epsilon_1(\omega)$ is a large negative constant, while $\epsilon_2(\omega)$ approaches infinity when ω approaches zero. The relations of complex refractive index $\tilde{n}$, permittivity $\epsilon(\omega)$, conductivity $\sigma(\omega)$, and wave impedance Z are discussed in Appendix A. In

this low-frequency region, the wave impedance (calculated according to Appendix A) is so small that total reflection with 180° phase difference of electromagnetic waves from silver is expected. The silver conductivity is real and also extremely high so that silver (and more generally noble metals) can be considered as PEC.

In the high frequency region where $1 < \omega\tau \ll \omega_p\tau$ ($\gamma < \omega \ll \omega_p$), Eq. 2.3 becomes:

$$\epsilon_1(\omega) \approx \epsilon_\infty - \frac{\omega_p^2}{\omega^2}; \qquad \epsilon_2(\omega) \approx \frac{\omega_p^2}{\omega^3\tau}. \tag{2.5}$$

It can be inferred that $\epsilon_1(\omega)$ is still negative and large while $\epsilon_2(\omega)$ is reduced significantly. The wave impedance is still small, indicating high reflectivity of metals in this frequency region. Expressing those material characteristics in terms of conductivity now, the real conductivity is strongly reduced, which indicates increased loss in metals. However, the imaginary part of $\sigma(\omega)$ increases significantly, indicating increased phase difference between the oscillating electrons and the electric field, and confirming that metals can no longer be seen as ideal conductors in this region.

As frequency approaches the ultraviolet region where $\omega \geq \omega_p$, Eq. 2.3 becomes:

$$\epsilon_1(\omega) \approx \epsilon_\infty - \frac{\omega_p^2}{\omega^2}; \qquad \epsilon_2(\omega) \approx \frac{\omega_p^2}{\omega^3\tau} \approx 0. \tag{2.6}$$

In this region, $\epsilon_1(\omega)$ and $\epsilon_2(\omega)$ are significantly reduced. It is noted that when $\omega = \omega_p$, a longitudinal electromagnetic mode, as denoted in Fig. 2.5(b), is supported by metals. In this case, a bulk plasmon resonance occurs and the electric field is depolarised. For frequencies much larger than the ω_p, $\epsilon_1(\omega)$ approaches ϵ_∞ and $\epsilon_2(\omega)$ approaches 0, therefore, silver (metals) becomes transparent and lossless (inter-band transitions are not considered). Electromagnetic waves in this case are in transverse mode and their dispersion relation is governed by:

$$\omega^2 = \omega_p^2 + k^2c^2. \tag{2.7}$$

where k denotes the free-space wavenumber. This relation is plotted in Fig. 2.5(b) as a curve asymptotically approaching the light line.

2.2.2 Propagating and localised surface plasmons

In 1902, R. D. Wood observed diffuse "diffraction" peaks from metallic gratings under a transverse magnetic (TM) polarised excitation with magnetic field parallel to the

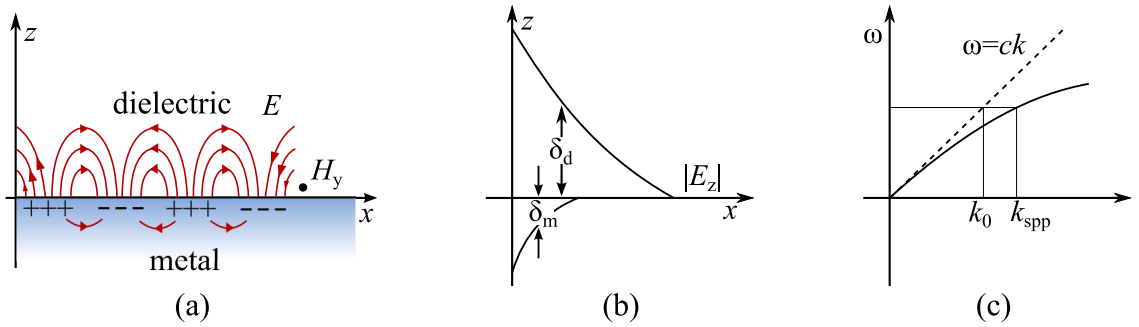

Figure 2.6. Concept of SPPs. (a) Illustration of SPPs at a metal-dielectric interface. (b) Along the perpendicular direction of the metal-dielectric interface, SPPs are evanescent waves that exponentially decay into the two sides of the interface. (c) A typical dispersion curve of SPPs. Figures are re-plotted based on (Benson 2011).

grating surface, where the intensity dropped from maximum to minimum within a very small wavelength range (Wood 1902). The Wood's Anomalies soon raised interests among many specialists and researchers in optics. Later, with the development of laser sources and microfabrication of holographic gratings, it was finally experimentally confirmed that a surface plasmon resonance was supported by metallic gratings and the corresponding resonance peaks (*i.e.* diffuse peaks) were broader than sharp diffraction peaks (Enoch and Bonod 2012). Thereby, Wood's Anomalies are viewed as the initiation of plasmonics. SPPs and LSPRs are the two fundamental types of plasmonic excitations. As conceptually illustrated in Fig. 2.6(a), SPPs are electromagnetic waves coupling with the collective oscillations of free electrons and are confined along a metal-dielectric interface at optical frequencies (Maier 2007). They are TM waves in characters (the magnetic field in the y-direction) and can only be excited by a TM-polarised excitation. As presented in Fig. 2.6(b), SPPs are evanescent waves in the direction perpendicular to the interface, as such are bounded and therefore non-radiative surface electromagnetic modes. These characteristics can be explained by considering the SPP wavenumber k_{spp} at a semi-infinite metal-dielectric interface (Maier 2007):

$$k_{spp} = k_0 \sqrt{\frac{\epsilon_d \epsilon_m}{\epsilon_d + \epsilon_m}}, \tag{2.8}$$

where $k_0 = 2\pi/\lambda_0$ is the free-space wavenumber and ϵ_d and ϵ_m are the complex relative permittivity of the dielectric and metal on the two sides of the interface. The SPP dispersion relation of Eq. 2.8 is conceptually plotted in Fig. 2.6(c). From Eq. 2.8 and Fig. 2.6(c), it is seen that at the same frequency, k_{spp} is larger than the free-space wavenumber k_0. This momentum mismatch implies that energy and momentum cannot be simultaneously conserved at a flat metal-dielectric interface, and therefore, SPPs cannot be

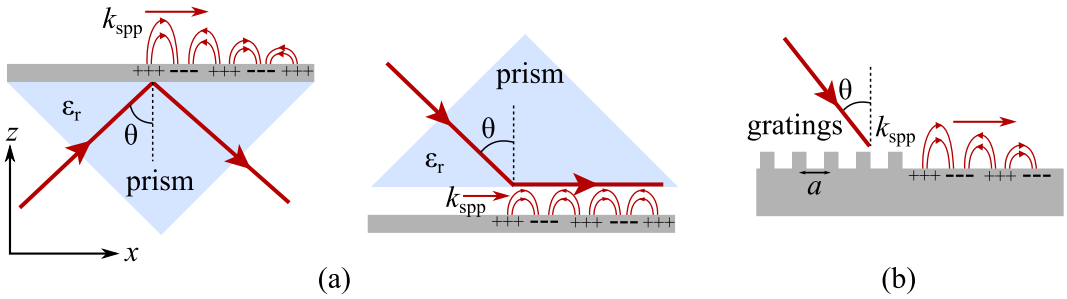

Figure 2.7. Conventional SPP coupling methods. (a) Prism coupling. Left: Kretschmann configuration. Right: Otto configuration. (b) Grating coupling.

directly excited by free-space incident electromagnetic waves. Conventionally, two proven techniques are used for providing extra momentum as depicted in Fig. 2.7(a,b). A prism with a relative permittivity ϵ_r can increase the momentum of an incident wave to match with that of SPPs, and the matching condition is: $k_{spp} = k_0\sqrt{\epsilon_r}\sin\theta$. Usually, an incidence at the critical angle is preferred to ensure maximum energy transfer. Grating coupling is the other commonly used SPP coupling method. Momentum matching can take place whenever the condition

$$k_{spp} = k_0 \sin\theta \pm n\frac{2\pi}{a}; \quad n = 1, 2, 3... \tag{2.9}$$

is fulfilled. Here a is the grating period and n is the diffraction order.

The confinement of SPPs to an interface can overcome the diffraction limit, which makes SPPs a potential candidate as optical signal carrier. Plasmonic couplers and waveguides are the basic components to control the propagation of SPP signals. Plasmonic couplers are usually based on grating structures as well as subwavelength holes (Devaux *et al.* 2003), grooves (Baron *et al.* 2011) or slits (Chen *et al.* 2010). Different functions such as SPP reflection, focusing, interference (Ditlbacher *et al.* 2002) and unidirectional launching (López-Tejeira *et al.* 2007, Liu *et al.* 2012) have been demonstrated. Chapter 4 is devoted to a discussion of SPP coupling and unidirectional launching, and proposes to use non-uniform arrays of DRs for SPP launching. For plasmonic waveguides, various types of guiding structures have been reported. Figure 2.8 summarises four different SPP waveguide structures including (a) bandgap structures (Marquart *et al.* 2005), (b) nanowires (Ditlbacher *et al.* 2005), (c) nanoparticle chains (Maier *et al.* 2003) and (d) metal slabs (Weeber *et al.* 2003). Bandgap structures are made of periodic arrangement of simple nano-geometries and their operation is similar to photonic crystals in the sense that they demonstrate stop band for SPPs in certain frequency ranges. Therefore, SPP can only propagate along the pre-designed direction on a metal surface. Nanowires

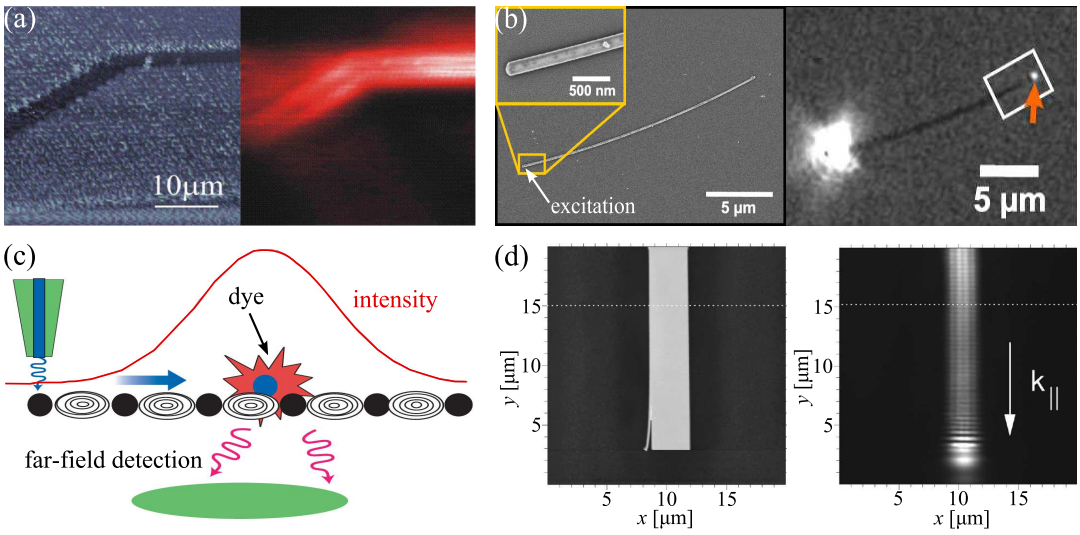

Figure 2.8. Plasmonic waveguide structures. Plasmonic waveguide structures based on (a) bandgap structures; (b) nanowires; (c) nanoparticle chain for sensing applications; (d) metallic strip/slab. (a) to (d) are reproduced from: Marquart *et al.* (2005), Ditlbacher *et al.* (2005), Maier *et al.* (2003) and Weeber *et al.* (2003), respectively.

are also extensively studied as waveguide structures. They can demonstrate transverse electromagnetic mode, which is similar to the dominant mode in microwave coaxial cables. A difference is that the transverse mode supported by nanowires are SPP evanescent waves confined to the nanowire surface. Figure 2.8(b) demonstrates energy transfer from one end of a nanowire to the other end. Figure 2.8(c) presents a SPP waveguide based on nanoparticle chains for sensing application. Nanoparticle chains can guide SPP propagations based on the coupling between adjacent metallic particles. Figure 2.8(d) shows that metal slabs embedded inside a dielectric material can support SPP propagation. A symmetrical mode (even) (Berini 2000) and an asymmetrical (odd) (Berini 2001) mode can be excited on a metal slab. The symmetrical mode demonstrates increased confinement and attenuation when reducing the slab thickness while the asymmetrical mode shows the opposite.

LSPRs are the other fundamental plasmonic excitation besides SPPs. Different from SPPs, LSPRs are electromagnetic waves coupling to collective electron oscillations bounded by metallic nanoparticles at optical frequencies (Maier 2007). Nanoparticles that support LSPRs are normally comparable or much smaller than the excitation wavelength. These small particles can provide extra momentum for matching free-space waves and LSPRs. Therefore, LSPRs supported within nanoparticles can be

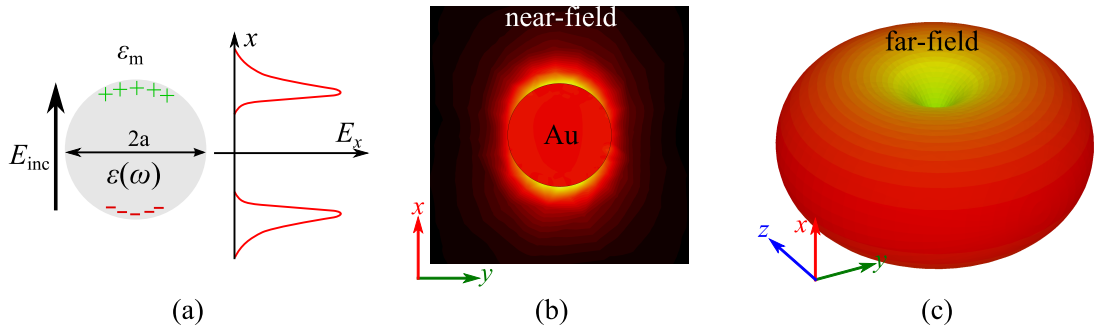

Figure 2.9. Illustration of localised surface plasmons resonance. (a) Illustration of a LSPR on a metallic nano-sphere when $Re[\epsilon(\omega)] = -2\epsilon_m$. (b-c) Simulation of a LSPR supported by a 40 nm (radius $a = 20$ nm) gold sphere in air at 716.5 THz. The x-polarised plane-wave excitation is incident from z-direction. The (b) near-field E-field and (c) far-field radiation E-field pattern are presented. Gold is described with the Drude model in Eq. 2.2 based on the data from Thoreson *et al.* (2010).

understood as a simultaneous conservation of energy and momentum (Enoch and Bonod 2012).

The brief discussion on LSPRs as presented here is based on the dipolar resonance and light extinction of a subwavelength metallic sphere. As delineated in Fig. 2.9(a), a subwavelength metallic sphere with radius a ($a \ll \lambda_{\text{inc}}$) demonstrates electric dipolar moment in response to an external excitation. By applying the Laplace's Equation for electric potential in the quasi-electrostatic assumption ($\nabla^2\Phi = 0$), the dipole moment of such a subwavelength sphere can be expressed as:

$$\mathbf{p} = 4\pi\epsilon_0\epsilon_m a^3 \frac{\epsilon(\omega) - \epsilon_m}{\epsilon(\omega) + 2\epsilon_m} E_{\text{inc}}, \tag{2.10}$$

where $\epsilon(\omega)$ is the dielectric function of the metallic particle described by a Drude model and ϵ_m is the relative permittivity of the surrounding dielectric medium. The term:

$$\alpha = 4\pi a^3 \frac{\epsilon(\omega) - \epsilon_m}{\epsilon(\omega) + 2\epsilon_m}, \tag{2.11}$$

is defined as the polarisability of this sphere. It is seen that $\mathbf{p}$ experiences a resonance if α reaches its pole when:

$$Re[\epsilon(\omega)] = -2\epsilon_m. \tag{2.12}$$

Equation 2.12 is the condition for metallic subwavelength spheres to be on LSP dipolar resonance. The magnitude of the resonant dipole moment largely depends on the imaginary part of the term $\epsilon(\omega) + 2\epsilon_m$. From Eq. 2.12, it is seen that LSPRs are very sensitive to the ambient environment. Therefore, LSPRs can be applied for sensing

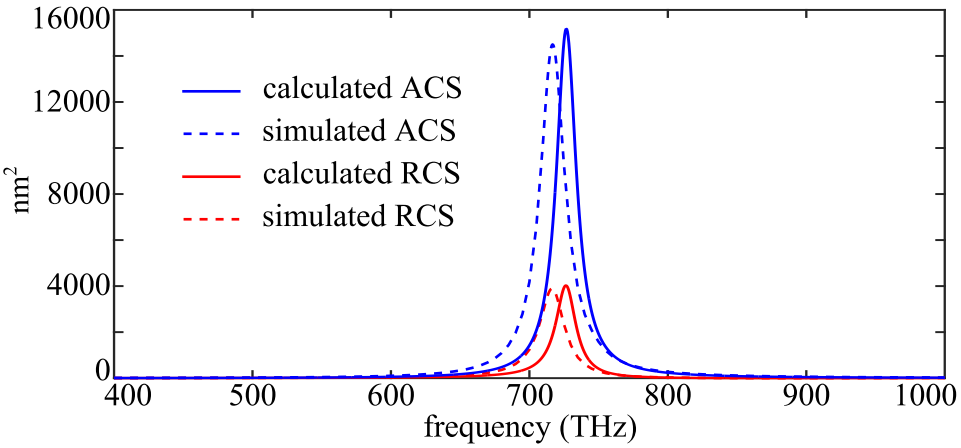

Figure 2.10. Calculated and simulated radar cross section and absorption cross section. Calculated and simulated radar (scattering) cross section (RCS) and absorption cross section (ACS) of a 40 nm ($a = 20$ nm) gold particle excited by a plane-wave excitation. Calculated results are based on Eq. 2.15 and 2.16 while simulations are performed with CST Microwave Studio. The discrepancies between the simulated and calculated results are mainly caused by the fact that the simulation based on finite-element method (FEM) is most likely more accurate than the quasi-electrostatic assumption adopted in Eq. 2.15 and 2.16.

applications, for instance, detecting the variation of refractive index (Liu *et al.* 2010). Figure 2.9(b,c) present the simulated near-field E-field distribution and far-field E-field pattern, respectively, of a 40 nm gold sphere under a plane-wave excitation. The results correspond to an infinitesimal dipolar resonance. This nano-scale dipolar resonance suggests that LSPRs can play an important role in optical nano-antennas for light manipulations and nano-scale light-object interactions (Novotny and Van Hulst 2011). The field enhancement around LSPR nanoparticles can also be applied for Surface Enhanced Raman Spectroscopy (SERS) (Kneipp *et al.* 1997, Willets and Van Duyne 2007). The near-field and far-field electric fields of a dipolar LSPR can be mathematically expressed as:

$$E(r,t) = \frac{1}{4\pi\epsilon_0\epsilon_m}\frac{3\mathbf{n}(\mathbf{n}\cdot\mathbf{p})-\mathbf{p}}{r^3}e^{-j\omega t}, \quad \text{(near-field)} \tag{2.13}$$

$$E(r,t) = \frac{k^2}{4\pi\epsilon_0\epsilon_m}\frac{(\mathbf{n}\times\mathbf{p})\times\mathbf{n}}{r}e^{j(kr-\omega t)} \quad \text{(far-field)}, \tag{2.14}$$

with $\mathbf{n}$ being the unit vector in the radial direction at the point of interest and $k = 2\pi/\lambda$. It is also important to consider power scattering and absorption by a nanoparticle under a plane-wave excitation. They are described by the scattering and absorption cross-sections defined as C_{scat}=I_{scat}/I_{inc} and C_{abs}=I_{abs}/I_{inc} (Bohren and Huffman 2008), in which I_{inc} is the incident intensity. C_{scat} and C_{abs} are calculated as (Bohren and

Huffman 2008):

$$C_{\text{scat}} = \frac{8\pi}{3}k^4a^6\left|\frac{\epsilon(\omega)-\epsilon_m}{\epsilon(\omega)+2\epsilon_m}\right|^2 = \frac{k^4}{6\pi}|\alpha|^2 \Rightarrow C_{\text{scat}} \propto \frac{a^6}{\lambda^4}, \tag{2.15}$$

$$C_{\text{abs}} = 4\pi k a^3 \text{Im}\left[\frac{\epsilon(\omega)-\epsilon_m}{\epsilon(\omega)+2\epsilon_m}\right] = k\text{Im}(\alpha) \Rightarrow C_{\text{abs}} \propto \frac{a^3}{\lambda}; \tag{2.16}$$

As a is much smaller than the incident wavelength λ, it is expected from Eq. 2.15 and Eq. 2.16 that C_{abs} would be much greater than C_{scat}. Figure 2.10 presented the simulated and calculated C_{abs} and C_{scat} of the 40 nm gold sphere presented in Fig. 2.9. The simulated and calculated results are close to each other, and C_{abs} is seen to be more than three folds of C_{scat}. As a significant amount of energy is absorbed in metallic nanoparticles that support LSPR, it can be seen that nano-scale DRs should have a higher radiation efficiency than their metallic counterparts.

2.3 Optical metasurfaces

This section presents a short review of optical metasurface research. Due to the diverse and fast-ongoing research activities on optical metasurfaces, the review does not attempt to present a comprehensive summary. Instead, this review covers the fundamentals and research of optical metasurface most relevant to the study in this thesis. The first part introduces wavefront engineering metasurfaces, which are seen as the beginning of optical metasurface research. The second part discusses the resonance modes in optical metasurfaces. Various resonance modes can be supported and tailored in optical resonators, and are important for metasurfaces to achieve their intended functionalities. Finally, the last part focuses on current research on DR metasurfaces, which are in close relation to the study in this thesis.

2.3.1 Optical metasurfaces for wavefront engineering

Wavefront engineering metasurfaces aim at manipulating the propagation of optical waves into an arbitrary pre-designed pattern based on controlling local phase distributions on metasurfaces. To realise that, a control of 2π phase range is required as can be obtained from subwavelength resonators near resonance. By properly arranging the local phase gradients, various wavefront engineering functions can be realised, including anomalous reflection (Zou *et al.* 2013, Sun *et al.* 2012b) and

transmission (Yu *et al.* 2011, Aieta *et al.* 2012b, Monticone *et al.* 2013), beam focusing (Aieta *et al.* 2012a, Pors *et al.* 2013, Asadchy *et al.* 2016, Kamali *et al.* 2016a, Kamali *et al.* 2016b), or vortex generation (Yu *et al.* 2011, Yang *et al.* 2014b). Although similar concepts have long existed at microwave frequencies in the form of reflectarrays (Mailloux 2005) and frequency-selective surfaces (Munk 2000), the extension to optical metasurfaces has brought new applications for optical components that can be realised on a flat thin film.

Figure 2.11(a) outlines the formalism of the generalised laws of reflection and refraction at an interface with local engineered phase gradients in the three-dimensional (3D) space, which can be mathematically expressed as:

$$\left.\begin{aligned} \sin(\theta_r) - \sin(\theta_i) &= \frac{1}{n_i k_0}\frac{d\Phi}{dx} \\ \cos(\theta_r)\sin(\varphi_r) &= \frac{1}{n_i k_0}\frac{d\Phi}{dy} \end{aligned}\right\} \quad \text{Generalised law of reflection} \tag{2.17}$$

$$\left.\begin{aligned} n_t \sin(\theta_t) - n_i \sin(\theta_i) &= \frac{1}{k_0}\frac{d\Phi}{dx} \\ \cos(\theta_t)\sin(\varphi_t) &= \frac{1}{n_t k_0}\frac{d\Phi}{dy} \end{aligned}\right\} \quad \text{Generalised law of refraction} \tag{2.18}$$

where k_0 is the free-space wavenumber and $d\Phi/dx$ and $d\Phi/dy$ are the phase gradients along x- and y-directions. Equations 2.17 and 2.18 indicate that metasurfaces are able to bend light to a pre-designed propagation direction. This concept has been experimentally demonstrated across a wide range of frequencies at microwave (Sun *et al.* 2012a), terahertz (Niu *et al.* 2013) and optical frequencies (Yu *et al.* 2011, Zou *et al.* 2013, Sun *et al.* 2012b, Yu and Capasso 2014, Li *et al.* 2015).

Figure 1.2 and Fig 2.11(b) present several reported optical metasurfaces for anomalous reflection/refraction. Among them, Fig. 1.2(a) is based on gold V-shape resonators. Depending on the length and the bending angle of a resonator, it can produce different reflection phase responses to the incident electromagnetic waves. Proper arrangement of different V-shape resonators can create phase gradients along the silicon substrate surface. Figure 1.2(b) shows a visible light reflectarray based on nano-scale TiO_2 cylinder resonators. Compared to the V-shape gold resonators, the DRs carry significantly lower Ohmic loss. Therefore, the radiation efficiency is higher. Figure 2.11(b) presents an anomalous reflection and beam splitting design based on metal-insulator-metal multilayer structures. Due to the trapezoid shape of the resonator, the phase gradient continuously covers the whole 2π phase range, which shows dispersion properties and is engineered for beam splitting.

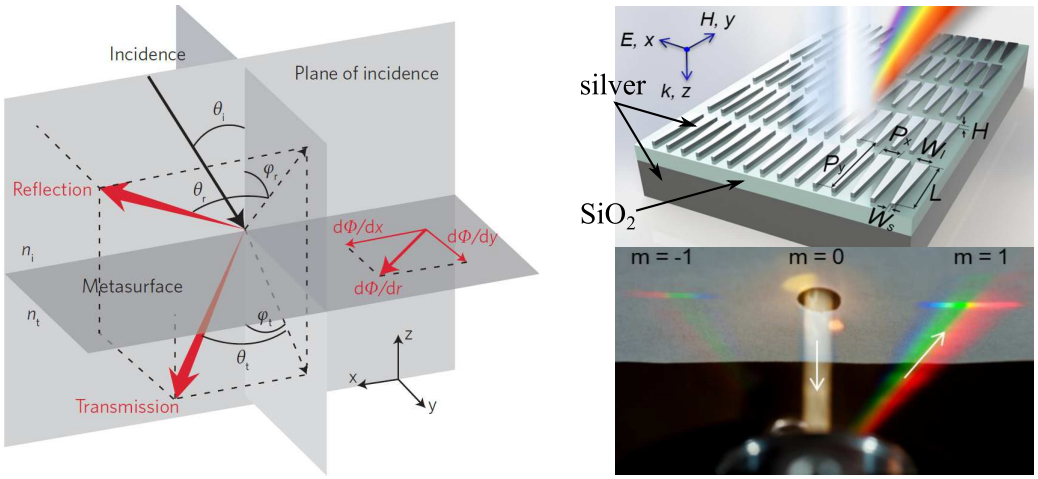

Figure 2.11. Optical metasurfaces demonstrating generalised law of reflection and refraction. (a) Illustration of generalised law of reflection and refraction in three-dimension space. n_i and n_t denote the refractive indices of media on both sides of a metasurface. The incidence is given from the x-z plane at an angle of θ_i. The reflected and refracted beams have angles of θ_r and θ_t to the y-z plane, respectively. Their projections on y-z plane have angles of φ_r and φ_t to the z-axis, respectively. (b) Anomalous reflection and spectrum splitting based on trapezoid silver antenna array and substrate with a SiO_2 spacer. (a) and (b) are reproduced from (Yu and Capasso 2014) and (Li *et al.* 2015) respectively.

Other wavefront shaping functions such as beam focusing (flat lens) (Aieta *et al.* 2012a, Pors *et al.* 2013) and vortex generation (Yu *et al.* 2011, Yang *et al.* 2014b) have also been demonstrated. Figure 2.12(a-c) presents a flat lens example, which is also based on V-shape nano-antenna array. To realise beam focusing, the phase discontinuities on a flat surface must fulfill the condition that:

$$\varphi(x,y) = \frac{2\pi}{\lambda}(\sqrt{x^2+y^2+f^2} - f). \tag{2.19}$$

In Eq. 2.19, $\varphi(x,y)$ describes the phase distribution on the flat lens surface described by a 2D coordinates, and f is the focus length of the designed lens. Beam focusing realised by an ultra-thin flat metasurface presents the advantage of achieving high numerical aperture (NA) with no aberration. Figure 2.12(d) presents a vortex generation by using V-shape gold resonator. The vortex beam can be applied in optical communication systems. Similar vortex beam nanostructures are also demonstrated based on DRs (Yang *et al.* 2014b). Due to the thin profiles of all these devices, it is much easier to integrate them as thin-film flat optical components into complex photonic systems and circuits.

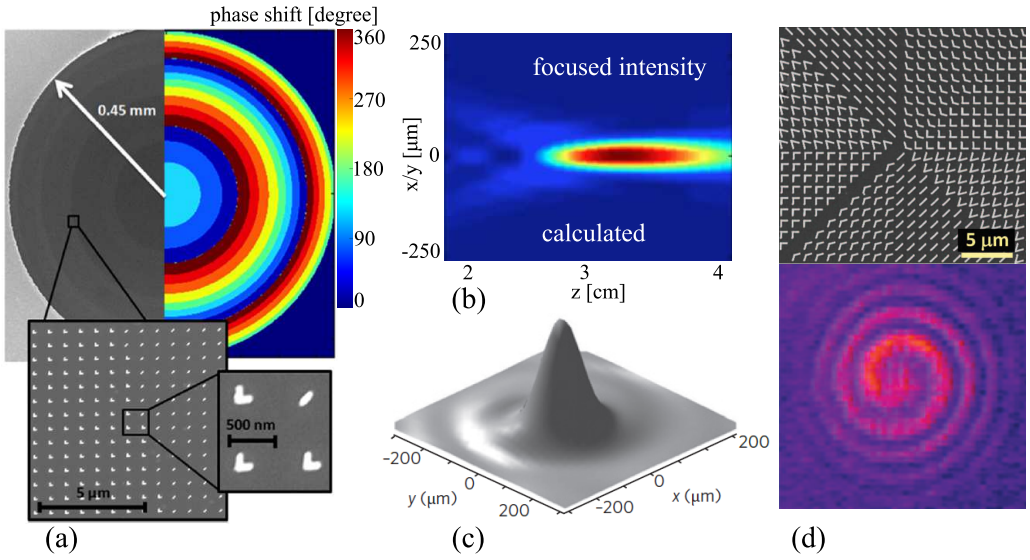

Figure 2.12. Flat lens focusing and vortex generation based on metasurfaces. (a-c) Flat lens focusing based on V-shape nano-antenna array (Aieta *et al.* 2012a). (a) The left and the bottom insets show the fabricated V-shape nano-antenna array while the right part shows the phase response distribution. (b) The calculated focused intensity in the focused region. (c) The measured 3D intensity distribution. (d) A beam vortex generated by a metallic resonator metasurface (Yu *et al.* 2011).

2.3.2 Resonance modes in optical metasurfaces

Controlling the resonance modes can lead to various functionalities of metasurfaces, such as light absorption (Zhang *et al.* 2012, Yao *et al.* 2014), directional scattering (Staude *et al.* 2013), field enhancement (Radko *et al.* 2009, Yang *et al.* 2014a), and polarisation conversions (Yang *et al.* 2014b). The electric dipolar resonance is the most commonly used resonance mode and can be easily obtained with a metallic nano-bar structure (Vecchi *et al.* 2009), as shown in Fig. 2.13(a). By changing the bar length, the resonance frequency and the resonance phase and magnitude can be changed. As shown in Fig. 2.13(b), by breaking a metallic bar to a V-shape, symmetric and anti-symmetric resonance modes can be excited depending on the incident polarisations (Yu *et al.* 2011). The anti-symmetric resonance can induce a magnetic dipole in the orthogonal direction. However, this is not a direct coupling with the magnetic component of the incident light and the efficiency is low (Cai and Shalaev 2010). To achieve a direct magnetic coupling, the metal-insulator-metal (MIM) multilayer structure (Cai *et al.* 2007b) is often adopted. One example is given in Fig. 2.13(c-d), and similar MIM nanoantennas have been demonstrated for SPP coupling (Liu *et al.* 2012). On the other hand, as discussed in Section 2.1.2, electric and magnetic resonances can be easily supported

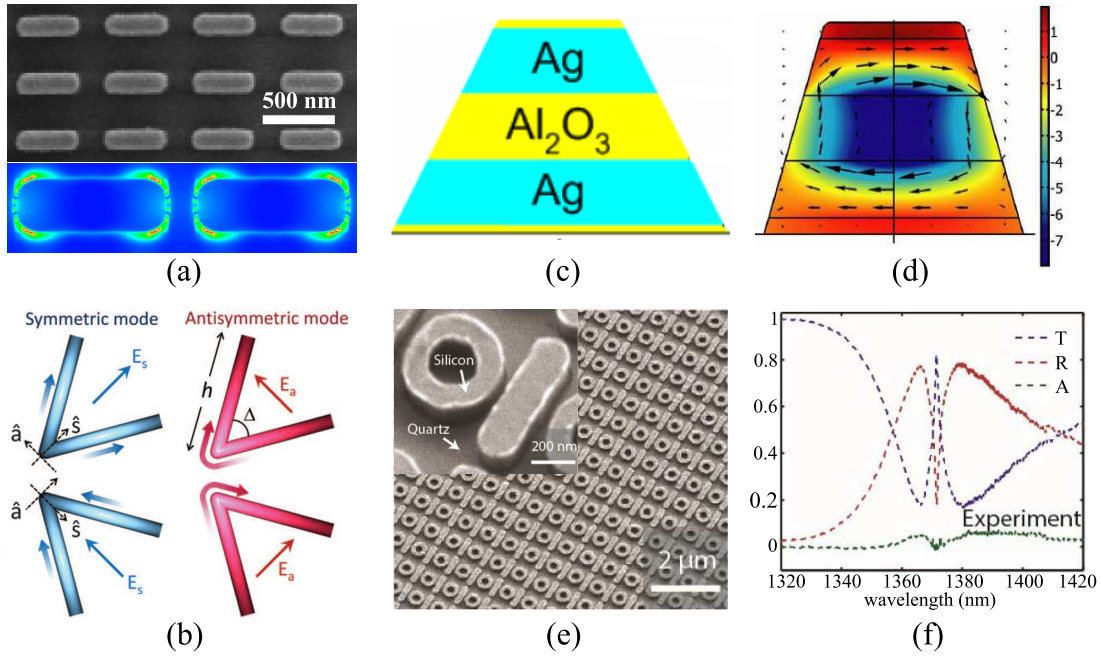

Figure 2.13. Examples of metasurface resonance modes. (a) Electric dipolar resonance mode supported by gold bar resonators (Vecchi *et al.* 2009). (b) Symmetric and asymmetric resonance modes supported by V-shape gold nano-antenna array (Yu *et al.* 2011). (c-d) Optical magnetic resonance supported by a Ag-Al_2O_3-Ag multilayer structure (Cai *et al.* 2007b). (e-f) Fano resonance supported by silicon bar and silicon ring resonators (Yang *et al.* 2014a). (e) shows the scanning electron microscope image of the fabricated metasurface and (f) corresponding measurement results.

by nano-scale DRs. By calculating the light scattering from a nanoscale DR, it is revealed that the magnetic dipole resonance occurs at lower frequencies, while electric dipole resonance, magnetic quadruple and electric quadruple resonances appear at higher frequencies (Kuznetsov *et al.* 2012). The resonances discussed above can all be directly excited by incident electromagnetic waves. Because of that, they are referred as bright resonance modes. On the contrary, dark resonance modes are the resonances that are indirectly excited by incident electromagnetic waves. Considering an example (Yang *et al.* 2014a) in Fig. 2.13(e,f), the incident electromagnetic waves excites the electric dipole resonance along silicon bars. Then, resonant silicon bars induce magnetic resonances in the adjacent silicon rings, whose magnetic fields are pointing normally to the surface. To excite this magnetic resonance in silicon rings, a break of symmetry (Singh *et al.* 2014) is necessary. The silicon bars in Fig. 2.13(c) have slightly different distances to their left and right silicon rings, so that a silicon ring is asymmetrically excited by two adjacent silicon bars. Such a magnetic resonance is indirectly excited by the incident electromagnetic waves and thus is referred as a dark resonance mode.

The interaction between bright and dark resonance modes can lead to Fano resonance (Luk'yanchuk *et al.* 2010) if they are both spatially and spectrally close to each other. Fano resonance can usually demonstrate a sharp resonance lineshape, which can be applied to sensing (Hao *et al.* 2008) and electromagnetic induced transparency (EIT) (Yang *et al.* 2014a, Marangos 1998, Zhang *et al.* 2008).

2.3.3 Dielectric resonator metasurfaces at optical frequencies

Recent years have seen significantly increased demonstrations of nano-scale DR metasurfaces at optical frequencies. As briefly mentioned in Chapter 1 and Section 2.1.2, nano-scale DRs made of low-loss dielectric materials have the advantage of high efficiency and supporting multiple resonance modes. These merits make them very attractive for constructing efficient optical functional nanostructures. A number of

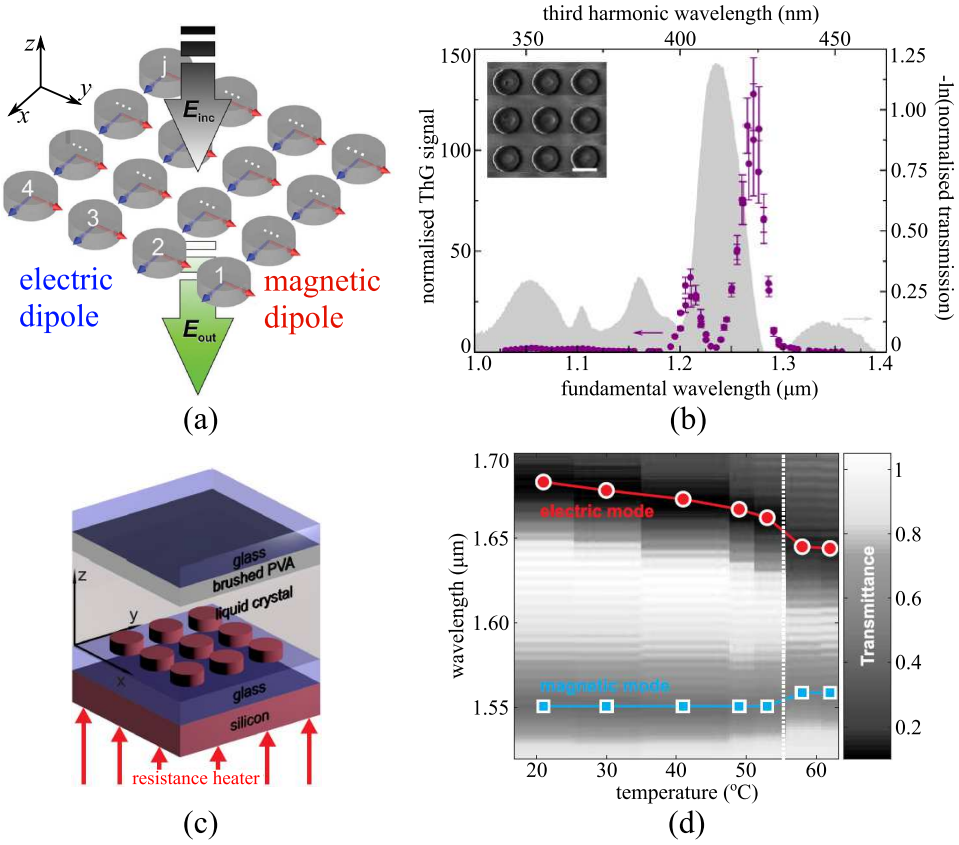

Figure 2.14. Optical DR metasurfaces. (a) Huygens' surface made of a uniform silicon DR array (Decker *et al.* 2015). (b) Silicon DR array for enhancing third harmonic generations (Shcherbakov *et al.* 2014). (c-d) Active tunable DR metasurface (Sautter *et al.* 2015).

DR-based optical metasurfaces have been demonstrated. Among them, many DR metasurfaces were made for wavefront engineering (Zou *et al.* 2013, Yang *et al.* 2014b, Asadchy *et al.* 2016, Kamali *et al.* 2016a, Kamali *et al.* 2016b). In these designs, efficient electric and magnetic resonances are utilised to provide local phase gradients, and they show higher efficiencies compared to their counterparts based on metallic resonators (Yu *et al.* 2011, Sun *et al.* 2012b). In the past a few years, many reported DR metasurfaces were based on silicon DRs. Due to the relatively higher refractive index, it is possible to excite several orders of resonance modes in the near-infrared and visible frequency ranges. For instance, by combining both electric dipole and magnetic dipole resonances in one DR at the same frequency, a highly directional radiating Huygens' sources (Decker *et al.* 2015) can be achieved, as shown in Fig. 2.14(a). In addition, resonant nano-scale silicon DRs are adopted for enhancing third-order harmonic generation (Shcherbakov *et al.* 2014). Figure 2.14(b) shows that the magnetic resonance of the silicon DR array enhances the third harmonic signals. Mie resonances supported by DRs can also be engineered into electric and magnetic reflectors at optical frequencies (Moitra *et al.* 2014). High reflectivity can be realised when a strong impedance mismatch is created by strong electric or magnetic resonances of DRs. Recently, DRs have also been demonstrated for active and reconfigurable metasurfaces (Sautter *et al.* 2015). One of the reconfigurable DR metasurfaces was achieved by embedding silicon DR arrays inside phase-changing liquid crystal. By changing the structure temperature, the material phase of the liquid crystal can be changed, and thus both magnetic and electric resonances can be tuned. Similar phase-change all-dielectric metasurfaces have also been reported by Karvounis *et al.* (2016). A mechanically tunable DR metasurface was also demonstrated in 2015 as part of the present research work and is further discussed in Chapter 6.

2.4 Summary

This chapter has summarised the most relevant background to the research presented in this thesis. A general introduction to microwave DRAs has been given in the first section. DRAs have the advantages of compact size, high efficiency, convenient coupling schemes, tunable bandwidth and multiple resonance modes. Features such as high efficiency and multiple resonances can be extended to the optical frequencies. As such, the use of DRAs promises highly efficient optical functional nanostructures. An introduction to the fundamentals of SPPs and LSPRs has been presented in the second

section. The section has first discussed the optical properties of metals based on the Drude model. Then, the basics of SPPs and LSPRs have been discussed, with a focus on SPP waveguides and LSPR dipolar resonance of metallic nanospheres. The last section has given a brief review of optical metasurfaces. Optical metasurfaces for wavefront engineering have been discussed in the first part. The second part has discussed different resonance modes, which are important for the designed functionalities in optical metasurfaces. The last part has reviewed current research on optical metasurfaces based on nano-scale DRs, which have attracted significant research attention in recent years.

Chapter 3

Resonance Breakdown of Nano-scale Dielectric Resonators

A major type of nanostructures studied in this thesis is based on patterning cylindrical subwavelength DRs on metallic substrates. DRs in such a configuration can be excited to resonate as horizontal magnetic dipoles. In this Chapter, the resonance characteristics of cylindrical DRs on metallic substrates are analysed in detail. It is found that two types of resonance breakdown can occur for DRs on metallic substrates at optical frequencies. The first type of resonance breakdown occurs in DRs made of materials with very low permittivities, where no resonance can be supported, because of the low contrast to the surrounding medium. Of particular interest is the second type of resonance breakdown, namely the negatively-matched resonance breakdown. This occurs when the real parts of permittivities of DRs and their metallic substrates are negatively matched. The negatively-matched resonance breakdown can be avoided by adding a thin low-permittivity layer between DRs and their substrates. This chapter provides a theoretical basis for the studies in Chapter 4 and 5.

3.1 Introduction

In recent years, dielectric resonators (DRs) have been increasingly proposed and used for achieving high-efficiency optical nanostructures. Among resonant dielectric structures, one type of them is made by patterning nano-scale DRs on metallic substrates (Zou *et al.* 2013, Zou *et al.* 2015a, Yang *et al.* 2014b). Such a metallodielectric combination is inspired by microwave DRAs, for which a metal ground plane is typically included as an electric symmetry plane. As depicted in Fig. 3.1(a-c), when excited by a normally incident plane-wave, a DR can resonate in its fundamental magnetic dipolar mode ($HEM_{11\delta}$), with equivalent dipole along the horizontal direction. This resonance mode is excited due to the symmetric nature of the normally incident *E*-field and is shaped by the boundary conditions at DR-air and DR-metal interfaces. At microwave frequencies, as an example given in Fig. 3.1(b), because metals are seen as perfect electric conductors (PECs), the *E*-field inside the DR is forced to be perpendicular to the metallic ground plane. In this case, the *E*-field has the highest intensity at the boundary of the DR but it becomes very weak at its centre. The dissipation in both the metal and the dielectric parts is low while most of the energy is radiated. The same structure can be down-scaled for terahertz and optical applications. At terahertz frequencies, metals still function as good conductors. Therefore, such metallodielectric structures supporting magnetic resonances can be made efficient, as demonstrated for magnetic mirrors (Headland *et al.* 2015) and focusing mirrors (Headland *et al.* 2016). As frequency approaches the optical range, metals become poor conductors and the plasmonic loss become obvious. As a result, the *E*-field at the DR-metal interface is not perpendicular to the metal surface and the highest *E*-field intensity is close to the centre of the DR, as shown in Fig. 3.1(c). The horizontal

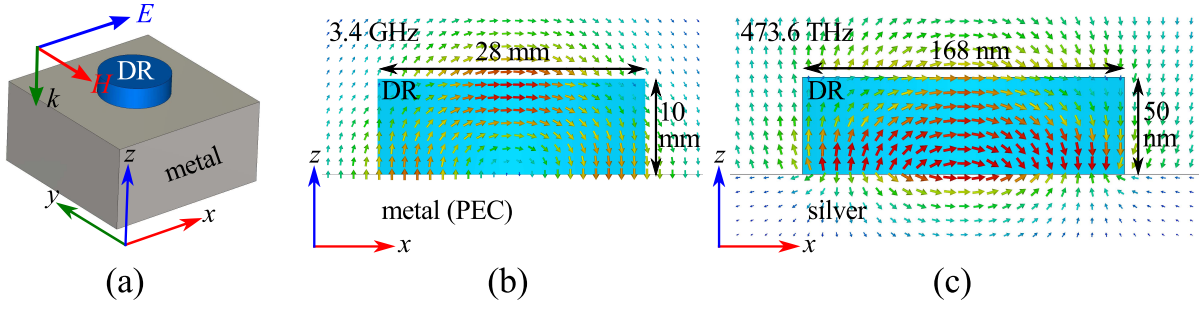

Figure 3.1. DRs resonating in their $HEM_{11\delta}$ mode. (a) Schematic of the simulated unit-cell structure. The simulation is performed with CST Microwave Studio. *E*-fields of $HEM_{11\delta}$ mode at (b) microwave frequencies and (c) visible light frequencies.

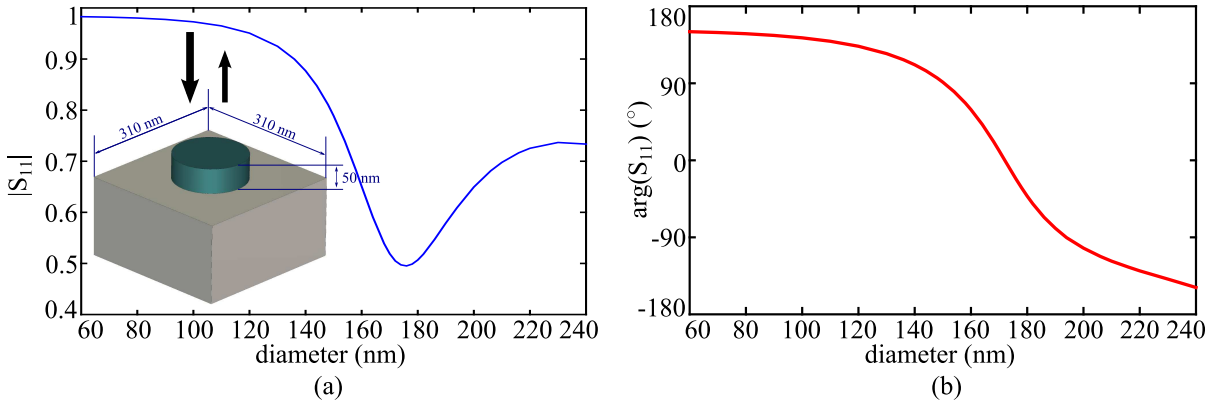

Figure 3.2. Reflection amplitude and phase of a uniform array of nano-scale DRs on a silver substrate. The simulated unit-cell structure is shown as the inset. TiO_2 and silver are selected to be the DR and the substrate respectively. The simulation is done at 633 nm with CST Microwave Studio.

magnetic dipole resonance in nano-scale DRs normally occurs when the DR diameter is around the half of the SPP wavelength λ_{spp} at the DR-metal interface.

The horizontal magnetic dipole resonance in nano-scale DRs on metallic substrates promises several prominent applications. As shown in Fig. 3.2, by varying the diameter of a cylindrical TiO_2 DR, a uniform array of the DR can demonstrate different reflection amplitude and phase responses. This property can be used to create phase gradients along a metallic surface and can be adopted for constructing optical reflectarrays (Zou *et al.* 2013) and other wavefront shaping metasurfaces (Yu and Capasso 2014). Another promising application of this type of nanostructure is for efficient SPP coupling (Zou *et al.* 2015a). Figure 3.3 demonstrates the concept of using DRs on a metallic substrate for efficient SPP coupling. A high coupling efficiency is suggested by the high similarity between the *E*-field distributions of a horizontal magnetic dipole and SPPs. Chapter 4 further elaborates on nano-scale DRs for SPP coupling and unidirectional launching.

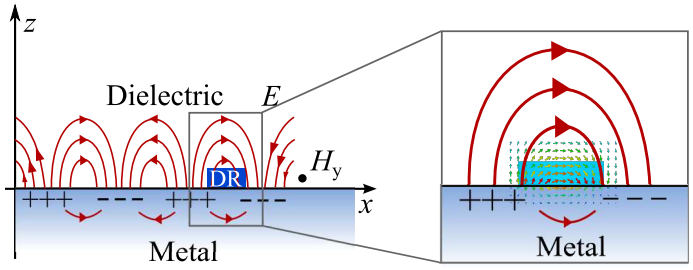

Figure 3.3. Illustration of DR as horizontal magnetic dipole for SPP coupling.

At optical frequencies, the magnetic dipole resonance of nano-scale DRs on metallic substrates are highly affected by the plasmonic effects. High plasmonic loss may lead to resonance breakdown and disfunction of a DR-based metasurface. Therefore, in this Chapter, the resonance properties of nano-scale DRs on metallic substrates are analysed in detail. It is found that two types of resonance breakdown can occur in subwavelength DRs on metallic substrates, and they are discussed in Section 3.2. Section 3.3 propose a mitigation method for the negatively-matched resonance breakdown. The study in this Chapter suggests important considerations for applying nano-scale DRs in the optical frequency range.

3.2 Resonance breakdown

At optical frequencies, nano-scale DRs on metallic substrates experience strong plasmonic effects at the metal-dielectric interface. To analyse the plasmonic effect on the resonance of DRs, firstly, a well-known situation of SPPs at the metal-dielectric interface is reviewed. Figure 3.4(a) outlines the scenario of SPP at a semi-infinite metal-dielectric interface. The relative permittivity of the metal is $\epsilon_m = \epsilon_m^{'} + i\epsilon_m^{''}$ and the relative permittivity of the dielectric is $\epsilon_d = \epsilon_d^{'} + i\epsilon_d^{''}$. At such an interface, the complex SPP wavenumber k_{spp} according to Eq. 2.8 is:

$$k_{spp} = k_0 \sqrt{\frac{(\epsilon_m^{'}\epsilon_d^{'} - \epsilon_m^{''}\epsilon_d^{''}) + i(\epsilon_m^{'}\epsilon_d^{''} + \epsilon_m^{''}\epsilon_d^{'})}{(\epsilon_m^{'} + \epsilon_d^{'}) + i(\epsilon_m^{''} + \epsilon_d^{''})}}, \tag{3.1}$$

where k_0 is the free-space wavenumber. Equation 3.1 tells that SPPs are confined electromagnetic waves with their propagation characteristics depending on the properties of materials at both sides of the interface. Considering a special case of matching condition that $\epsilon_d^{'} = -\epsilon_m^{'}$ and assuming that the dielectric material is lossless (i.e., $\epsilon_d^{''} = 0$), Eq. 3.1 becomes:

$$k_{spp} = k_0 \sqrt{\epsilon_d^{'} + i\frac{\epsilon_d^{'2}}{\epsilon_m^{''}}} \approx k_0 \frac{\epsilon_d^{'}}{\sqrt{2\epsilon_m^{''}}} [(1 + \frac{\epsilon_m^{''}}{2\epsilon_d^{'}}) + i(1 - \frac{\epsilon_m^{''}}{2\epsilon_d^{'}})]. \tag{3.2}$$

The first-order approximation is taken in Eq. 3.2. For noble metals, the real part of their permittivity $\epsilon_m^{'}$ (which is assumed to be equal to $-\epsilon_d^{'}$) is much greater than the imaginary part $\epsilon_m^{''}$. Therefore, from Eq. 3.2, it is seen that the real part of k_{spp} at the matched interface is roughly $\epsilon_d^{'}/\sqrt{2\epsilon_m^{''}}$ times of k_0 and that the real and imaginary parts of k_{spp} are large and nearly equal. This result implies an extremely small SPP wavelength as well as a large propagation loss. Therefore, SPPs in this case can hardly

propagate. Additionally, the matched permittivities result in a depolarised electric field at the metal-dielectic interface (Maier 2007). Figure 3.4(b,c) present the calculated dispersion diagrams at interfaces of silver (Palik 1998) and different dielectric materials. The green curves represent the SPP wavevector at the silver-air interface, where the matched-permittivity (depolarisation) point is at the silver surface plasmon wavelength λ_{sp} (Maier 2007). As the relative permittivity ϵ_r of the dielectric material increases, the depolarisation point is shifted from ultraviolet to the visible wavelength range. Following the increase in the permittivity of the dielectric material, the plasmonic loss increases dramatically while the SPP wavelength shrinks significantly.

Based on the discussion above, the plasmonic effects on the resonance of nano-scale DRs on metallic substrates are analysed as follows. The analysis is carried out by simulating a uniform nano-scale DR array on a silver substrate and gradually increasing the DR relative permittivity ϵ_r from low to high values at 622 nm. The selection of the simulation wavelength considers that the real part of the relative permittivity of silicon $\epsilon_{Si} = 15.2$ (Palik 1998) matches well with that of silver (Palik 1998) with ϵ_{Ag} of $-15.2 + i1.03$ at 622 nm. This selection indicates certain practical scenarios. However,

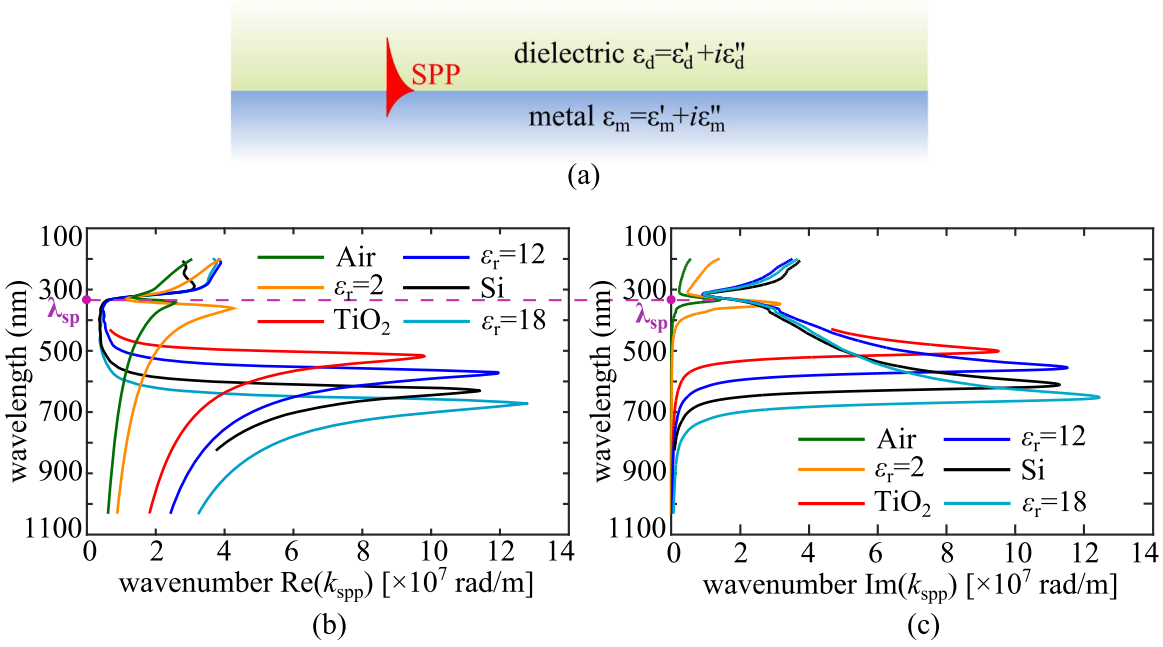

Figure 3.4. SPP at metal-dielectric interface and calculated SPP dispersions. (a) Illustration of SPP at semi-infinite metal-dielectric interface. Real (a) and imaginary (b) parts of SPP wavenumber at silver-dielectric interface calculated from Eq. 3.1. The properties of silver, TiO_2, and silicon are realistic and thus account for material dispersion and absorption (Palik 1998). Other dielectric materials considered here are lossless and nondispersive.

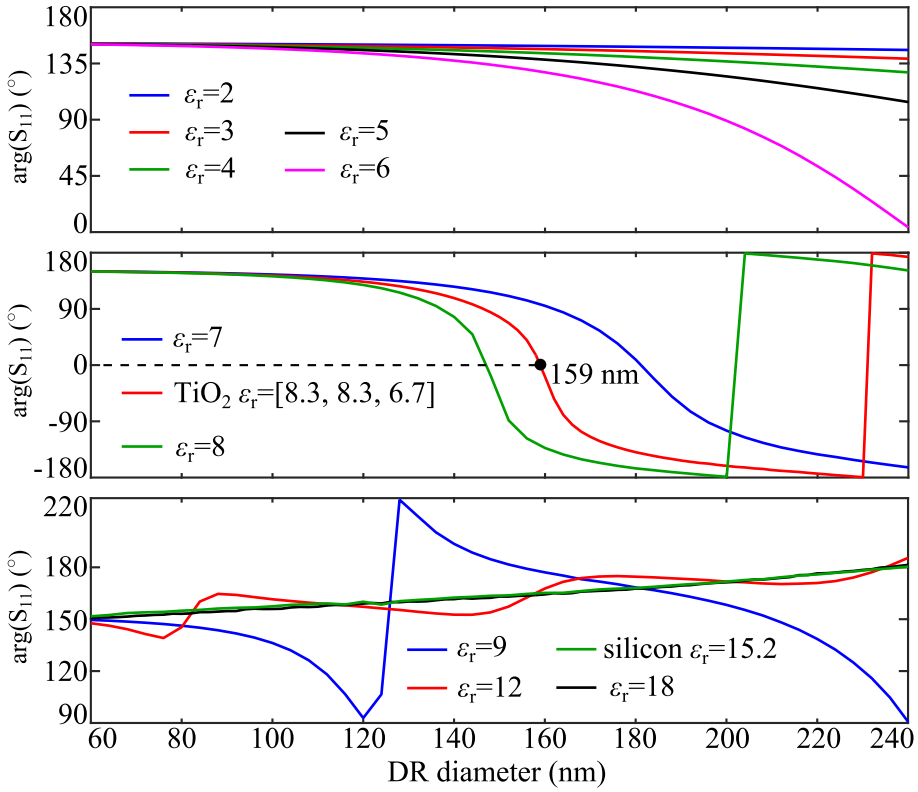

Figure 3.5. Reflection phase responses of uniform DRA arrays on metallic substrates. All simulations are carried out with the frequency-domain solver of CST Microwave Studio at 622 nm (482 THz). The simulated structure is a uniform cylindrical DRA array on a silver (Palik 1998) substrate, with a fixed unit cell size 350×350 nm^2 and a DRA height 50 nm. The DR diameter and its relative permittivity ϵ_r are varied. (a) Reflection phase responses of uniform DRA arrays with low permittivity on a silver substrate. Resonance breakdown is observed for very low permittivity values. DRAs of slightly higher permittivities are off-resonance. (b) Reflection phase responses of uniform DRA arrays of moderate permittivity on a silver substrate. The results show efficient DRA resonance. (c) Reflection phase responses of uniform DRA arrays of high permittivity on a silver substrate. The results suggest the matched-permittivity resonance breakdown.

it must be noted that $\langle 100 \rangle$ silicon cannot be directly grown on a silver surface due to their lattice mismatch. The selection of materials is thus for illustration purpose only. The simulated relative permittivities of DRs range from 2 to 18 and the selected unit cell size of the uniform array is 350×350 nm^2.

The simulation results of reflection phase responses and E-field distributions are summarised in Fig. 3.5 and Fig. 3.6 respectively, which depict different resonance and resonance breakdown scenarios. Figure 3.5(a) summarises the simulated reflection phase responses of uniform DR arrays with the DR permittivity ranging from 2 to 6. For the DR arrays of permittivity values of 2 and 3, the phase responses are nearly flat

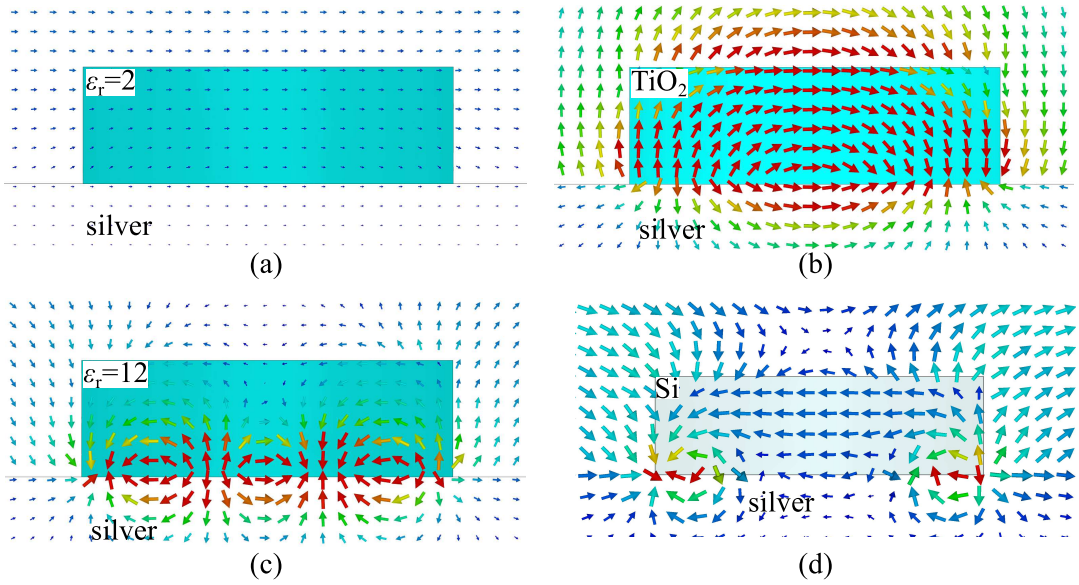

Figure 3.6. Illustrations of DR resonance breakdown. The simulated E-fields of same-size DRs of different materials on a silver substrates are presented. The DR diameter is marked as the black dot in Fig. 3.5(b). The simulation setup is identical to the setup described in Fig. 3.5. (a) Lossless DR with $\epsilon_r = 2$. (b) TiO_2 DR. (c) Lossless DR with $\epsilon_r = 12$. (d) Silicon DRA.

lines. This indicates that DRs with such low permittivity values are not able to confine incident energy sufficiently to sustain any resonances, and most of the incident light is scattered. As the permittivity increases above these values, the DRs start to show a weak resonance. While due to the limitation of the unit cell size, the DR size is too small for its resonance wavelength, and thus demonstrate limited phase ranges. Figure 3.6(a) plots the E-field of the DR with $\epsilon_r = 2$ on a silver substrate. It is seen that there are no resonance modes in the nano-scale DR. This corresponds to the low-permittivity resonance breakdown due to the low energy confinement and large radiation loss.

As the DR permittivity increases to moderate value, the DR array on a silver plane demonstrates a clear resonance feature. Figure 3.5(b) presents the reflection phase responses of DR arrays with moderate permittivity values. Taking the red curve of the TiO_2 DR array as an example, a phase range of nearly 2π can be achieved by varying the diameter of the DR. Figure 3.6(b) presents the E-field distribution of a resonant TiO_2 DR when excited by a normally incident plane wave at 622 nm. This resonance corresponds to a fundamental magnetic dipole resonance and its diameter is marked as the black dot in Fig. 3.5(b). Such a resonance feature can be tailored to support various dielectric optical metasurface designs (Zou *et al.* 2013, Zou *et al.* 2015a, Yang *et al.* 2014b).

With the permittivity rising to even higher value, the DR starts to experience the negatively matched-permittivity resonance breakdown. Figure 3.5(c) presents the reflection phase responses of DR arrays with high permittivity values. As the DR permittivity increases, the DR array demonstrates a diminishing phase range covering a nearly flat line when the positive permittivity of the dielectric (silicon) matches the absolute value of the negative permittivity of the metallic substrate (silver). Figure 3.6(c,d) present illustrative results. For the DR with $\epsilon_r = 12$, a higher-order mode resonance is observed due to the wavelength shortening effect, while for the silicon DR array on a silver substrate, no resonance can be sustained. This confirms the discussion in Section 3.2, which predicted that due to the negatively matched permittivities, the plasmonic loss increases dramatically while the SPP wavelength at the interface is significantly shortened. As such, SPPs can hardly propagate and consequently no resonances are supported. The reflection phase response of the DR array with $\epsilon_r = 18$ is also plotted in Fig. 3.5(c). In this case, the DR permittivity is away from the matching point and the SPP wavelength is significantly longer than that at the matched point. However, the plasmonic loss remains very large, and thus no resonance can be sustained. Therefore, a nearly flat line reflected phase curve is observed.

3.3 Resonance breakdown mitigation

The resonance breakdown of DRs on metallic substrates limits the efficient designs to only a narrow range of DR relative permittivities. To avoid the negatively-matched resonance breakdown, a thin low-permittivity dielectric layer can be deposited between the DR array and its metallic substrate to reduce the plasmonic losses and the wavelength shortening effect (Yang *et al.* 2014b). Figure 3.7 shows an example of such a structure in which a 10 nm SiO_2 layer is deposited between the DR array and its silver substrate. Simulated reflection phase responses of this structure are also presented in Fig. 3.7. We compare the phase responses with that in Fig. 3.5. The modified structure still demonstrates low-permittivity resonance breakdown at very low permittivity values and off-resonance features at slightly higher DR permittivities. However, the negatively matched-permittivity resonance breakdown occurring at high DR permittivities is clearly avoided. Instead, the DR array demonstrate 2π phase responses in a significantly larger DR permittivity range. Within such a larger range, DRs can keep their resonance characteristics and high efficiency. In this way, the selection of dielectric materials is relaxed for possible optical nanostructure designs.

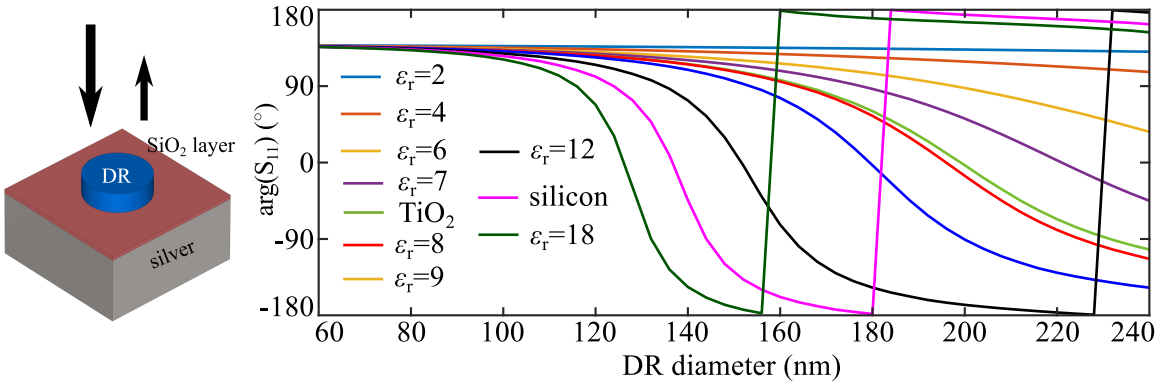

Figure 3.7. Reflection phase of modified DR arrays on metallic substrates. The structure unit-cell on the left shows the modified structure with a 10 nm SiO_2 layer deposited between the DR and its silver substrate. The simulation setup and structure are the same as described in Fig. 3.5 except for the SiO_2 layer.

3.4 Conclusion

In this chapter, nano-scale cylindrical DRs on metallic substrates for supporting horizontal magnetic dipolar resonance have been analysed. Such structures can create phase gradients along a metallic surface and can be applied for wavefront engineering. Likewise, the horizontal magnetic dipole resonance supported by DRs on metallic substrates can also be applied to design efficient SPP couplers. Based on the discussion of SPP at negatively-matched interface and verifications with full-wave simulations, two types of resonance breakdowns of nano-scale DRs on metallic substrates at visible frequencies have been analysed. As the permittivity of a DR on a metallic substrate increases from low to high values, the DR experiences low-permittivity and matched-permittivity resonance breakdowns at the two extremes. As a consequence, DRs only resonate efficiently within a limited range of permittivities. The two types of resonance breakdown occur due to the high radiation losses and plasmonic losses respectively. Of particular interests is the negatively matched-permittivity resonance breakdown, which occurs when the dielectric and metallic materials are negatively matched in their permittivities. The matched-permittivity resonance breakdown can be avoided by inserting a thin low-permittivity dielectric layer between the DRA array and its metallic substrate. As a result, the DRA permittivity range for efficient resonance can be significantly broadened. The study in this chapter suggests certain critical considerations when designing

metallodielectric nanostructures at the visible frequencies and lays the theoretical basis for the following chapters.

Chapter 4

Directional Excitation of Surface Plasmons by Dielectric Resonators

AN important aim of current research on plasmonics is to develop compact components to manipulate surface plasmon polaritons (SPPs). More specifically, one major aim is to develop efficient SPP couplers. The commonly used metallic resonators are inefficient to couple free-space waves to SPPs, while metallic gratings require oblique incidence for achieving unidirectional propagation. In this chapter, nano-scale non-uniform arrays of dielectric resonators (DRs) on metallic substrates are proposed for unidirectional launching of SPPs. The application of metallodielectric nanostructures can produce resonances mainly in the low-loss DRs and hence the power dissipated through oscillating current in metal can be reduced. DRs operating near resonance can provide phase control when coupling incident waves into SPPs. The theoretical analysis and simulations show that non-uniform DR arrays can efficiently launch SPPs into a pre-designed direction. Furthermore, with proper patterning, optimal launching can be achieved by avoiding power leakage via deflection into free space. The SPP launching condition and the influence of propagation loss are mathematically analysed from the viewpoint of antenna array theory. The SPPs launchers based on DRs have a potential for applications in highly efficient integrated optics and optical waveguides.

4.1 Introduction

Integrated optics and photonics have made remarkable contributions to the advancement of telecommunications, information processing and storage, sensing and spectroscopy. The miniaturisation of photonic devices may potentially enable low power consumption in ultra-fast processors, high-resolution imaging and sensors with unprecedented sensitivity and specificity. As an emerging branch in nanophotonics, plasmonics has gained significant interest in the past decade, thanks to the unique properties of subwavelength optical confinement and field enhancement in metallic nanostructures.

As a key element of plasmonic devices, unidirectional SPP launchers have attracted significant research attention in recent years. Conventionally, free-space propagation waves can be coupled into SPPs via prisms or metallic gratings (Maier 2007). However, prisms are too bulky for integrated optics, while metallic gratings require phase differences introduced by oblique incidence to realise unidirectional launching of SPPs (Hutley and Maystre 1976). So far, various nanostructures based on different principles have been demonstrated for unidirectional SPP launching, aiming at overcoming the limitation of the conventional coupling methods and providing discrete components for integrated optics. Figure 4.1 summarises several reported SPP launchers based on different nanostructures. A nanoslit on a metal surface can provide extra momentum and work as a SPP coupler that launches SPPs bidirectionally. Combined with metallic gratings (Gan *et al.* 2007) or Bragg reflectors (Fu *et al.* 2008, López-Tejeira *et al.* 2007), the SPPs coupled by a nanoslit can be guided or reflected into a desired direction. An example of a nanoslit with Bragg reflectors is presented in Fig. 4.1(a). Such a configuration can demonstrate high unidirectioal launching ratio by increasing the number of Bragg reflectors. With some modifications, an asymmetric nanoslit combined with a nanocavity (Chen *et al.* 2010) can realise unidirectional SPP launching based on wave interference from the Fabry-Pérot resonance. Grooves (Kuttge *et al.* 2009) and apertures (Yin *et al.* 2004) on metallic surfaces have also been demonstrated for SPP coupling. In general, when excited by incident electromagnetic waves, grooves and apertures can create horizontal magnetic currents whose field distributions are comparable to that of SPPs. Therefore, they can work as SPP couplers. As shown in Fig. 4.1(b), by changing the dimensions of grooves, a phase shift can be added to the excited SPPs. Thus a non-uniform array of grooves (Baron *et al.* 2011, Huang and Brongersma 2013) can achieve unidirectional SPP launching resulting from wave interference. Similar SPP launching principle has also been demonstrated based on apertures (He *et al.* 2012). Recently,

Liu *et al.* (2012) presented a compact magnetic antenna launcher consisting of two near resonant Au-MgF_2-Au sandwich structures, as shown in Fig 4.1(c). This arrangement is equivalent to two horizontal magnetic dipoles where a phase shift is obtained from different antenna dimensions. The SPP unidirectional launcher mentioned above are all based on SPP reflection and interference where phase shifts are necessary. On the other hand, an intriguing unidirectional SPP launcher based on a structure mimicking a single rotating dipole (Xi *et al.* 2014) has also been reported. More sophisticated SPP launcher designs have also been demonstrated. Lu *et al.* (2013) demonstrated an ultra-broadband SPP unidirectional launchers, which realised strong unidirectional SPP coupling from

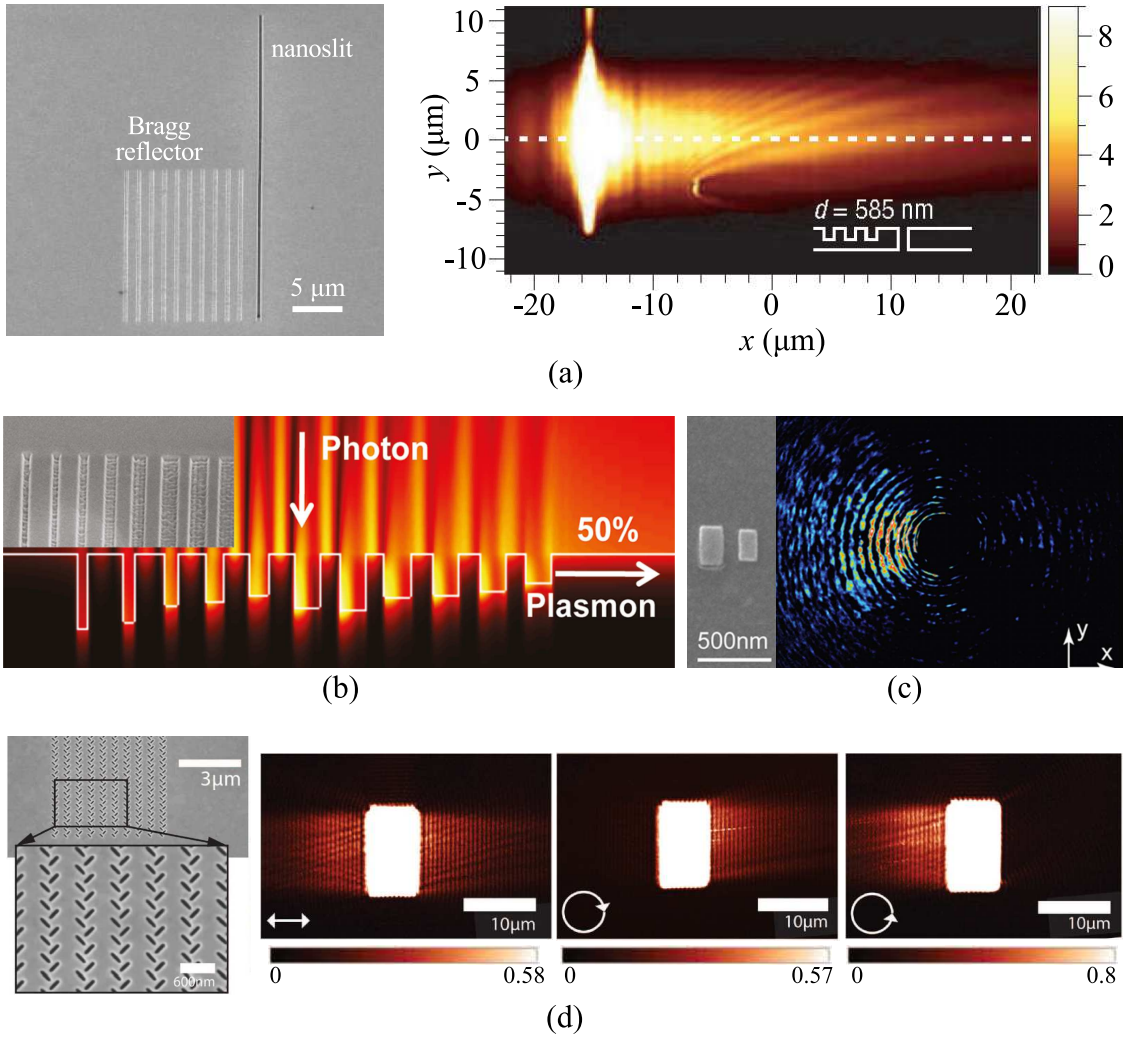

Figure 4.1. Experimentally demonstrated unidirectional SPP launchers. SPP launchers based on (a) nanoslit and bragg reflectors; (b) non-uniform grooves; (c) Au-MgF_2-Au magnetic antennas; (d) cross polarised aperture arrays. Figures and results of designs in (a-d) are adopted from López-Tejeira *et al.* (2007), Baron *et al.* (2011), Liu *et al.* (2012), and Lin *et al.* (2013), respectively.

690 nm to 900 nm. Lin *et al.* (2013) reported a polarisation-dependent SPP launcher, shown in Fig. 4.1(d). The aperture arrays with orthogonal orientations can launch SPP into left, right or bi-directions when excited by waves with different polarisations.

In this chapter, based on the SPP coupling mechanism by DRs discussed in Section 3.1 of Chapter 3, unidirectional SPP launchers made of non-uniform arrays of DRs on metallic substrates are proposed and studied. Section 4.2 analyses the optimal SPP launching condition. Section 4.3 further examines the SPP launching based on linear antenna array theory, with the consideration of SPP propagation loss and finite array sizes. Section 4.4 presents the verification of unidirectional SPP launching and the optimal launching condition based on numerical simulations.

4.2 Optimal SPP launching condition

A common principle for unidirectional launching of SPPs is based on wave interference. This interference process is illustrated in Fig. 4.2(a) for the proposed SPP launcher based on DRs. For simplicity, only two adjacent DRs from an infinite array are considered first. The DRs are located on a silver surface with a distance d between their centres and they have phase responses on reflection corresponding to φ_1 and φ_2. Illuminated by a TM-polarised light with an incidence angle of θ_i, the two resonators couple the incident waves into SPPs. The SPPs excited by those two elements have phase differences imposed by the elements' intrinsic phase responses, the incident angle, and the different

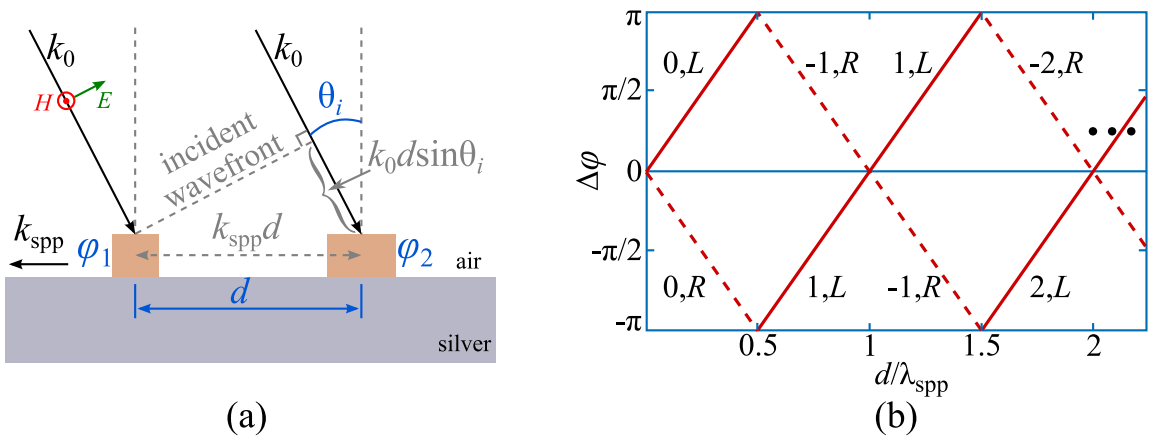

Figure 4.2. DR array for SPP excitation. (a) Schematic of DRs for SPP unidirectional launching. (b) SPP directional launching lines for an infinite ideal array of DRs and a normal incidence. Here numbers denote the diffraction order while L and R denote left (solid line) and right (dashed line) directions.

propagation distances. With proper phase matching, constructive interference can be achieved on one side along the metal surface, with destructive interference on the other side. This phase matching condition can be generally described as:

$$\text{Leftward launching:} \quad \varphi_1 = \varphi_2 + k_0 d \sin\theta_i - k_{\text{spp}} d + 2v\pi, \tag{4.1a}$$

$$\text{Rightward launching:} \quad \varphi_1 - k_{\text{spp}} d = \varphi_2 + k_0 d \sin\theta_i + 2v\pi, \tag{4.1b}$$

$$\text{In summary:} \quad \varphi_1 \pm k_{\text{spp}} d = \varphi_2 + k_0 d \sin\theta_i + 2v\pi; \tag{4.1c}$$

where k_0 is the wavenumber of the incident free-space wave and k_{spp} denotes the wavenumber of the propagating SPPs launched by the DRs. However, it should be noted that the wavevector $\boldsymbol{k}_{\text{spp}}$ in Eqs. 4.1(a) and (b) points to opposite directions. Therefore, when combined to a single equation in Eq. 4.1(c), it is necessary to define the positive direction of $\boldsymbol{k}_{\text{spp}}$. The amplitude of the wavevector $\boldsymbol{k}_{\text{spp}}$ is defined with positive sign to the left as shown in Fig. 4.2(a). In Eq. 4.1(c), the case of "$+$" represents the perfect constructive interference towards the left-hand side while the "$-$" describes the perfect constructive interference towards the right-hand side. The integer $v = 0, \pm 1, \pm 2...$ denotes the SPP launching order. Under normal incidence, where $\theta_i = 0°$, Eq. 4.1 is simplified to:

$$\pm k_{\text{spp}} = \frac{\Delta\varphi}{d} + v\frac{2\pi}{d}, \tag{4.2}$$

with $\Delta\varphi = \varphi_2 - \varphi_1$. The solutions of Eq. 4.2 is graphically presented in Fig. 4.2(b). The plotted lines indicate perfect constructive interference on one side but destructive interference on the other side. Practically, lower launching orders v, and small distances d are preferred to minimise propagation losses. This preference is also reflected in the analysis in Section 4.3.

Besides SPP launching, the progressive phase response of a non-uniform DR array can be configured for realisation of reflectarrays at optical frequencies (Zou *et al.* 2013, Yang *et al.* 2014b). The optical reflectarray in Zou *et al.* (2013) was demonstrated to deflect incident light into a pre-designed direction in free space. In the context of SPP launching, this deflection mechanism reduces the power available for surface wave coupling and must be suppressed. In the following, we analyse how to minimise power leakage from deflection and achieve optimal SPP launching.

As illustrated in Fig. 4.3(a), the beam deflected by two adjacent elements towards an angle θ_r can be described by the phase matching condition:

$$\varphi_1 + k_0 d \sin\theta_r = \varphi_2 + k_0 d \sin\theta_i + 2(m-1)\pi. \tag{4.3}$$

Here the index $m = 1, 2, 3...$ represents diffraction orders created by the two adjacent resonators. The numbering "$m-1$" is selected such that $m = 1$ matches the first diffraction order. For normal incidence ($\theta_i = 0°$), the m^{th}-order diffraction (deflection) angle can be calculated as:

$$\sin\theta_r = \frac{\Delta\varphi}{k_0 d} + (m-1)\frac{2\pi}{k_0 d}\,. \tag{4.4}$$

For the array configuration with progressive $\Delta\varphi$ and inter-element spacing d, the $m = 1$ order deflection is the most relevant and needs to be suppressed. From Eq. 4.4, a necessary condition can be found by considering that the $m = 1$ order deflection can be accessed only when $|\sin\theta_r| \leq 1$. i.e.

$$\frac{|\Delta\varphi|}{d} \leq k_0. \tag{4.5}$$

This condition is presented graphically in Fig. 4.3(b), showing, the well-defined areas as deflection zone (shaded; $|\sin\theta_r| \leq 1$) and non-deflection zones (unshaded; $|\sin\theta_r| > 1$). To facilitate the analysis of achieving optimal SPP launching and suppressing wave deflection, Fig. 4.2(b) and Fig. 4.3(b) are combined into Fig. 4.4(a), in which λ_0 is selected to be 633 nm (equivalent to 474 THz) and the corresponding λ_{spp} is calculated on a silver-air interface. It is seen in Fig. 4.4(a) that the zeroth-order directional SPP launching lines lie inside the non-deflection zone. Hence, the lines satisfy the condition for unidirectional SPP launching, while prohibiting power leakage from deflection. The ($\Delta\varphi$, d) pairs corresponding to these lines fulfill:

$$\frac{|\Delta\varphi|}{d} = k_{\text{spp}} > k_0. \tag{4.6}$$

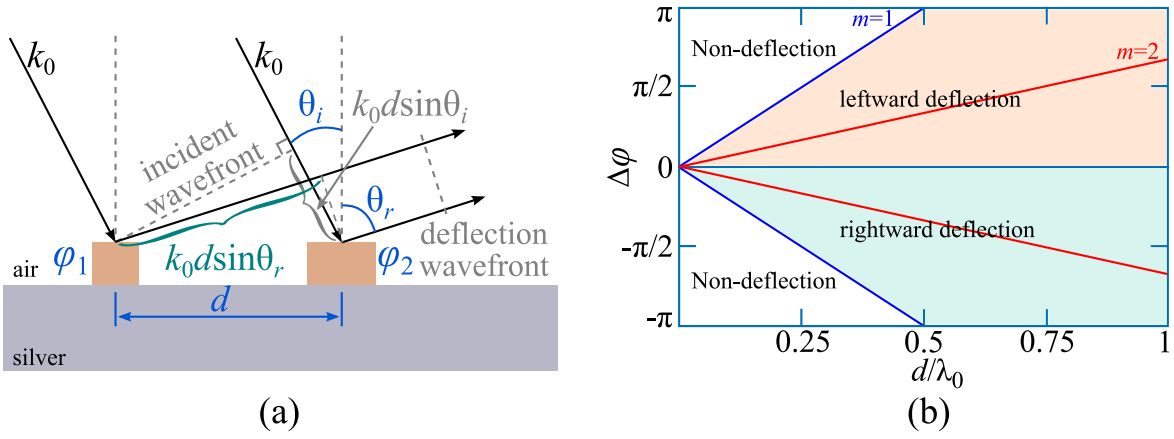

Figure 4.3. DR array in reflectarray configuration. (a) Schematic of DRs for reflectarray beam deflection. (b) Deflection zone and non-deflection zone. The blue lines and red lines denote the first and the second order deflections tangential to the surface ($\theta_r = \pm 90°$) respectively.

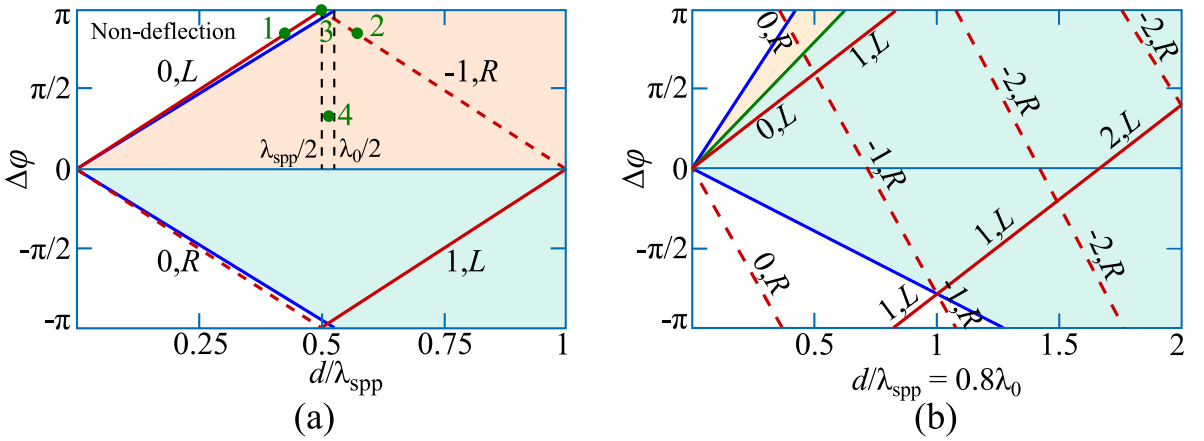

Figure 4.4. SPP launching condition. (a) Normal incidence with $k_{spp} = 1.033k_0$ (SPP wavenumber calculated on silver-air interface at 633 nm). The green dots 1, 2 and 3 correspond to design and simulation cases 1, 2 and 3 in Section 4.4. The reflectarray realised in (Zou *et al.* 2013) is also labelled as dot 4. (b) Oblique incidence at 30° with increased $k_{spp} = 1.25k_0$ for illustration purposes.

Therefore, any pair along the $v = 0$ order lines promises high SPP launching efficiencies while the crossing points between the L and the R lines such as $(\frac{\lambda_{spp}}{2},\pi)$ promises bidirectional launching, which, in the case of infinite arrays, will result in standing waves. The non-deflection condition introduced in this section defines a radiation pattern with a unique main lobe along the launching direction on the metal surface, and without grating lobes to match higher diffraction orders (Zou *et al.* 2013). In effect, optimal SPP launching can be achieved.

The considerations of optimal launching can be extended to the case of oblique incidence, where the cumulative phase shift is caused by both the resonators' phase responses and the incidence angle. For this general case, Eq. 4.1(c) can be used for describing the ideal SPPs momentum matching, while the deflection conditions can be retrieved from Eq. 4.3. In particular, for the $m = 1$ order, the deflection angle can be calculated as:

$$\sin\theta_r = \frac{\Delta\varphi}{k_0 d} + \sin\theta_i. \tag{4.7}$$

To illustrate the effect of the angle of incidence, a sample case with an incidence angle $\theta_i = 30°$ is presented in Fig. 4.4(b) where the k_{spp} is increased to $1.25k_0$ for better illustration. It is observed that an asymmetry is introduced by the incidence angle and both the deflection zone and directional propagation lines are rotated in the graph. Nevertheless, optimal launching condition can be identified on the SPP launching line in the non-deflection zone, where the deflection angle θ_r becomes imaginary. Thus, the

optimal condition can be described as:

$$\frac{|\Delta\varphi|}{d} + k_0 \sin\theta_i = k_{\text{spp}} > k_0. \tag{4.8}$$

The green solid line denotes the Littrow configuration where the incident beam is reflected back along the incident path (Palmer and Loewen 2005).

4.3 Linear array theory for SPP launching

The analysis in Section 4.2 offers general guidelines for designing optimal launchers in an ideal infinite array based on the inter-element distance d and the progressive phase shift $\Delta\varphi$. However, this analysis does not include the effects of SPP propagation loss and of the finite extent of the array. Here the analysis is extended with a simple one-dimensional interference model which assumes a finite N-element array repeated infinitely in the direction perpendicular to the SPP launching direction. Additionally, all DRs, excited by a normally incident TM-polarised light, are assumed to have the same radiation pattern and the uniform amplitude of unity. As shown in Fig. 4.5, the N-resonator array is located on a silver surface and the elements have a progressive phase shift of $\Delta\varphi$. According to the interference principle, the total amplitude is the superposition of SPPs launched by all the resonators to either sides of the array. The total amplitude of the SPPs at observation points located at a distance D from the edge resonator on the left and right can be calculated as (with the time dependence $e^{i\omega t}$ omitted):

$$\begin{aligned} A_L &= \sum_{n=1}^{N} e^{-ik_{\text{spp}}[D+(n-1)d]+i(n-1)\Delta\varphi} \\ &= e^{-ik_{\text{spp}}D} \cdot \frac{1-e^{iN(\Delta\varphi-k_{\text{spp}}d)}}{1-e^{i(\Delta\varphi-k_{\text{spp}}d)}}; \end{aligned} \tag{4.9a}$$

$$\begin{aligned} A_R &= \sum_{n=1}^{N} e^{-ik_{\text{spp}}[D+(n-1)d]-i(n-1)\Delta\varphi} \\ &= e^{-ik_{\text{spp}}D} \cdot \frac{1-e^{iN(\Delta\varphi+k_{\text{spp}}d)}}{1-e^{i(\Delta\varphi+k_{\text{spp}}d)}}. \end{aligned} \tag{4.9b}$$

In Eqs. (4.9), A_L and A_R are the total SPP amplitude summations for propagation towards the left and right sides respectively. The complex SPP wavenumber k_{spp} includes the phase constant β and the attenuation constant α. Provided that the array

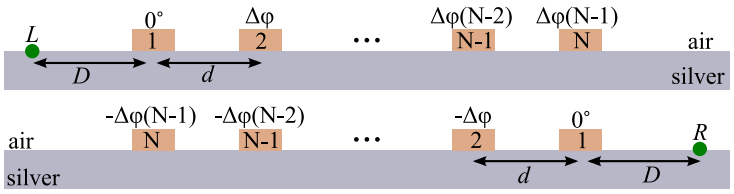

Figure 4.5. Concept of a N-DRA array with progressive phase. The observation green points L and R are set at left and right sides of the array.

operates at 633 nm on a silver-air interface, the complex SPP wavenumber is $k_{\text{spp}} = 1.025 \times 10^7 - i1.017 \times 10^4$ rad/m (Maier 2007, Zou *et al.* 2013). In the following, we will analyse SPP launching in this formalism starting from the infinite ideal array and later increasing complexity to observe the impact of the finite extent and propagation losses on the launching performance. First, the propagation loss is neglected or equivalently k_{spp} is assumed real. For an infinite array, i.e. the number of resonators $N = \infty$, the normalised left and right amplitudes can be analytically calculated as:

$$\begin{aligned} A_L/N &= \lim_{N\to\infty} \frac{1}{N} \frac{1 - e^{iN(\Delta\varphi - k_{\text{spp}}d)}}{1 - e^{i(\Delta\varphi - k_{\text{spp}}d)}} \\ &= \begin{cases} 1; & \Delta\varphi = k_{\text{spp}} \cdot d + 2m\pi \\ 0; & \text{otherwise} \end{cases} \end{aligned} \tag{4.10a}$$

$$\begin{aligned} A_R/N &= \lim_{N\to\infty} \frac{1}{N} \frac{1 - e^{iN(\Delta\varphi + k_{\text{spp}}d)}}{1 - e^{i(\Delta\varphi + k_{\text{spp}}d)}} \\ &= \begin{cases} 1; & \Delta\varphi = -k_{\text{spp}} \cdot d + 2m\pi \\ 0; & \text{otherwise} \end{cases} \end{aligned} \tag{4.10b}$$

where m is an arbitrary integer. This analysis confirms that for infinite lossless arrays, optimal directional launching is satisfied when $\Delta\varphi = \pm k_{\text{spp}}d + 2m\pi$, i.e. on directional launching lines shown in Fig. 4.2(b). On the other hand, if the condition is not strictly satisfied, the SPP vanishes.

For a finite array, optimal launching is still achieved by arrays on the directional launching lines in Fig. 4.2(b), but other array configurations that are not located on these lines can also lead to non-zero SPP amplitude. This is exemplified in Fig. 4.6(a) for propagation towards the left, in the case $N = 10$ (*i.e.* calculated based on Eq. 4.10a). The difference between normalised launched power to the left side and right side is presented in Fig. 4.6(b,c). The results from Fig. 4.6(a-c) confirms that the difference of launched power from finite arrays in the non-optimal launching region is not strictly

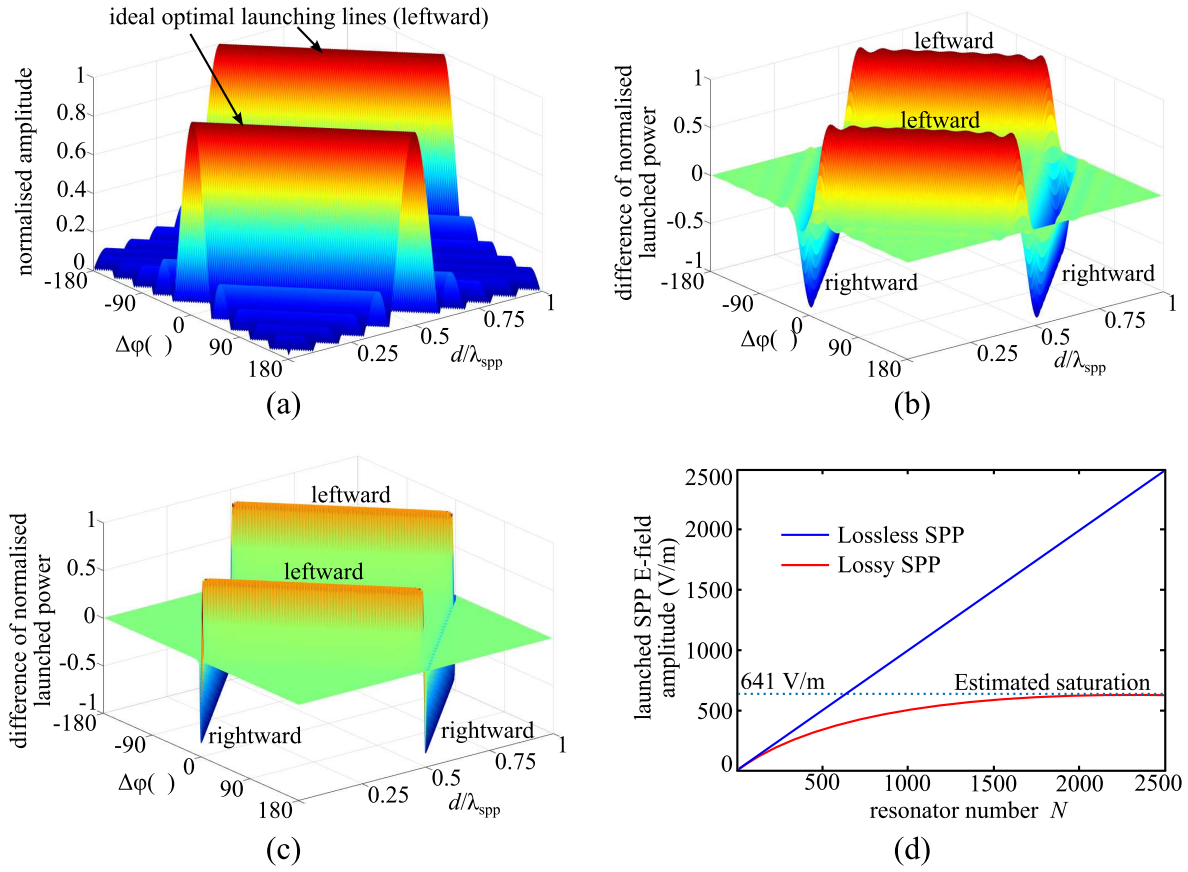

Figure 4.6. SPP launching calculation based on linear array theory. (a) Normalised SPP amplitude towards the left-hand side of finite arrays ($N = 10$) with different d and $\Delta\varphi$. (b-c) Difference of normalised power launched to the left (positive) and right (negative) for values (b) $N = 10$ and (c) $N = 100$. (d) Launched SPPs E-field amplitude for lossy (red) and lossless (blue) conditions, calculated at silver-air interface at 633 nm. Each DR is assumed to have SPP amplitude of 1 V/m.

zero and this effect is more obvious for smaller arrays than for larger arrays. With an increased number of resonators, the regions of unidirectional launching become increasingly narrower and, as can be expected, the results rapidly converge to the launching lines when N approaches infinity. It is also observed that on the launching lines, the SPP power for finite arrays is not constant, since a small amount of power can be launched towards the opposite direction too.

Now the analysis is extended to include the impact of the one-dimeonsional (1D) propagation loss by considering the complex SPP wavenumber k_{spp} given earlier. At 633 nm, the 1D propagation length (Zayats *et al.* 2005) of SPPs with infinite transversal extent on an ideally flat silver-air interface is approximately equal to 50 μm (Maier 2007, Zou *et al.* 2013), where the energy decays along the propagation direction of

SPPs wavefronts to $1/e$ or the amplitude decays to about 60.6%. Due to the amplitude attenuation, SPPs excited by a given resonator have negligible contribution to the total SPP beyond a certain distance. Mathematically, a re-examination of Eqs. 4.9(a) with k_{spp} replaced by $\beta - i\alpha$ yields:

$$A_{L,\alpha} = e^{-ik_{spp}D} \cdot \frac{1 - e^{iN(\Delta\varphi - \beta d)} e^{-Nd\alpha}}{1 - e^{i(\Delta\varphi - \beta d)} e^{-d\alpha}}; \tag{4.11}$$

where $A_{L,\alpha}$ is the launched SPP amplitude at a distance D away from a N-element array with given inter-element distance d and progressive phase $\Delta\varphi$. Due to the propagation loss, it can be indeed calculated that the value of $A_{L,\alpha}$ converges to $e^{-ik_{spp}D}/(1 - e^{i(\Delta\varphi - \beta d)} e^{-\alpha d})$ when N approaches infinity and $e^{-Nd\alpha}$ becomes zero. An example corresponding to the $(\Delta\varphi, d)$ pair $(\frac{\pi}{2}, \frac{\lambda_{spp}}{4})$ on $(0, L)$ line is presented in Fig. 4.6(d), where it is clearly visible that the launched SPP E-field amplitude saturates due to the propagation loss.

4.4 Verification

In this section, in order to apply and validate the optimal launching condition, various SPPs launching structures made of non-uniform arrays of DRs on a metal surface are designed and demonstrated through full-wave simulation. The designed structures are shown in Fig. 4.7. All DRs are cylindrical in shape with varying radii but a uniform height of 75 nm. The centre distance between neighbouring resonators is denoted as d. Resonators are located on a silver substrate, which has a thickness of 150 nm and width of 300 nm. TiO_2 is selected for the DRs because of its electrical properties and relative ease of patterning at nanometre scale. The material offers an anisotropic relative

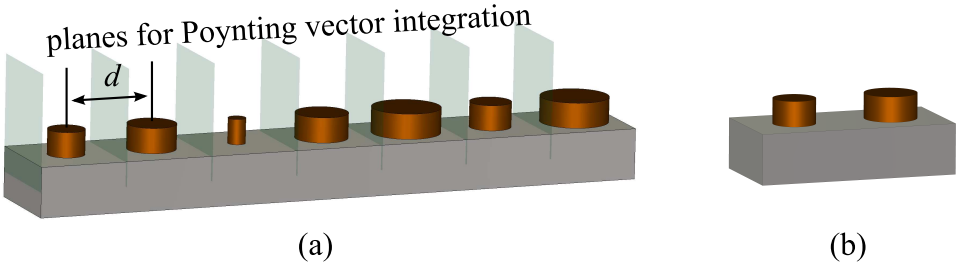

Figure 4.7. The designed SPP launcher. (a) Illustration for Cases 1 and 2 with a difference in the inter-element spacing d and resonator sizes. Poynting vector towards the left direction is integrated over transparent green planes illustrated in the figure for optimisation. (b) Illustration for Case 3 as a bidirectional coupler.

Table 4.1. Design parameters. The design cases are denoted as numbered green dots in Fig. 4.4(a).

Case	1	2	3	4 (Zou *et al.* 2013)
$\Delta\varphi$	$6\pi/7$	$6\pi/7$	π	$\pi/3$
d	$3\lambda_{spp}/7$ (265 nm)	$4\lambda_{spp}/7$ (350 nm)	$\lambda_{spp}/2$ (300 nm)	$\lambda_0/2$ (310 nm)
N	7	7	2	6
Subarray length	$3\lambda_{spp}$ (1855 nm)	$4\lambda_{spp}$ (2450 nm)	λ_{spp} (600 nm)	$3\lambda_0$ (1860 nm)
Function	Left launching	Right launching	Standing waves	Deflection

permittivity of 8.29 along the planar axes and 6.71 along the cylindrical axis with a loss tangent of less than 0.01 (Zou *et al.* 2013). Silver, as the metal substrate, offers a relative permittivity of $-16.05 + i0.48$ at 633 nm (Zou *et al.* 2013). At 633 nm, the SPP wavelength on the silver-air interface equals to $\lambda_{spp} = \lambda_0\sqrt{(\epsilon_{Ag} + \epsilon_{air})/\epsilon_{Ag}\epsilon_{air}} = 613$ nm.

Three illustrative cases are selected from the $v = 0, -1$ orders L and R lines, as indicated by the numbered green dots in Fig. 4.4(a). These practically realisable cases are selected with consideration of the sizes of resonators, which determine the smallest inter-element distance d, since neighbouring resonators cannot be patterned too close to each other. The corresponding element spacing d and required phase progressions are summarised in Table 4.1. Case 1 is selected on the ideal launching line with $v = 0$ in the non-deflection zone while Case 2 is on the line $v = -1$ in the deflection zone. According to Eq. 4.4, Case 2 promises a first order ($m = 1$) diffraction at an angle of $-48.6°$ from the normal direction. Case 3 is at the intersection of the lines $v = 0$ (L) and $v = -1$ (R), and hence Case 3 should couple incident light into SPPs propagating towards two

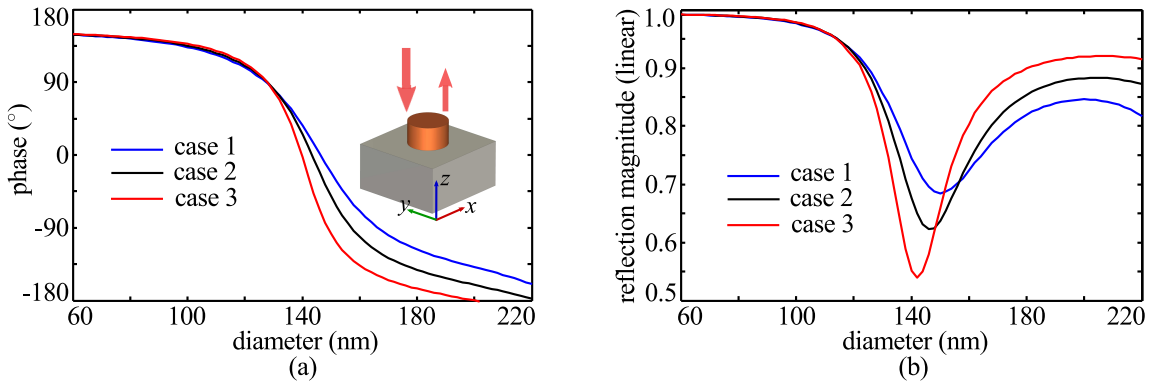

Figure 4.8. Numerically calculated phase responses and reflection magnitudes. The cases 1, 2, 3 are results of unit cells corresponding to simulations of marked dots 1, 2 and 3 in Fig. 4.4(a).

Table 4.2. Radii of DRs in the four featured simulation cases.

Case	Radius (nm)						
	R_1	R_2	R_3	R_4	R_5	R_6	R_7
1	106	63.5	105.5	61.5	113	84.5	51.5
2	84.5	69.5	99.5	58.5	35	82.5	57.5
3	64	79	#	#	#	#	#
4 (Zou *et al.* 2013)	33	77	85	90	96.5	121	#

opposite directions, resulting in standing waves. In addition to the three cases above, a previously published DR-based reflectarray (Zou *et al.* 2013), labelled as Case 4, is also marked in Fig. 4.4(a). In this last case, the goal of the reflectarray design was deflection and thus the geometry is located far from the SPP launching lines so that most of the incident power is deflected at a pre-designed offset angle from specular direction.

The required phase gradient for the three designs can be obtained by varying the size of the resonators. It can be shown that TiO_2 resonators with different radii around resonance exhibit different phase responses and reflection magnitudes when illuminated normally by plane waves (Zou *et al.* 2013). At 633 nm, the phase curves and reflection magnitudes can be computed via numerical simulations in infinite uniform array conditions. This has to be done separately for the different inter-element distance d corresponding to the three considered cases, as presented in Fig. 4.8. The obtained phase curves cover a range of about 330°, which is commonly deemed sufficient for practical designs. For the first three design cases marked by the green dots in Fig. 4.4(a), the radii of the individual DRs are selected from the phase curves to cover a cycle of 2π phase change and the obtained values are summarised in Table 4.2. These examples are specifically chosen to allow periodic repetition in subarrays formed by a small number of DRs covering one phase cycle. The simulations are carried out with the frequency-domain solver of CST Microwave Studio, using unit cell boundary conditions and TM (E-field parallel to the DR subarray) Floquet ports. Mutual coupling between the resonators with different sizes influences the local phase responses. Since the phases are calculated in a uniform array configuration, an optimisation of DRs' radii is necessary to compensate non-uniform coupling and achieve optimal launching. The optimisation is carried out for Cases 1 and 2 by maximising the Poynting vector integrated on a series of selected planes normal to the silver surface (as represented in Fig. 4.7(a)). In contrast, for simulation of Case 3, no optimisation is required as the effect of DR phase variation originating from non-uniform coupling is negligible.

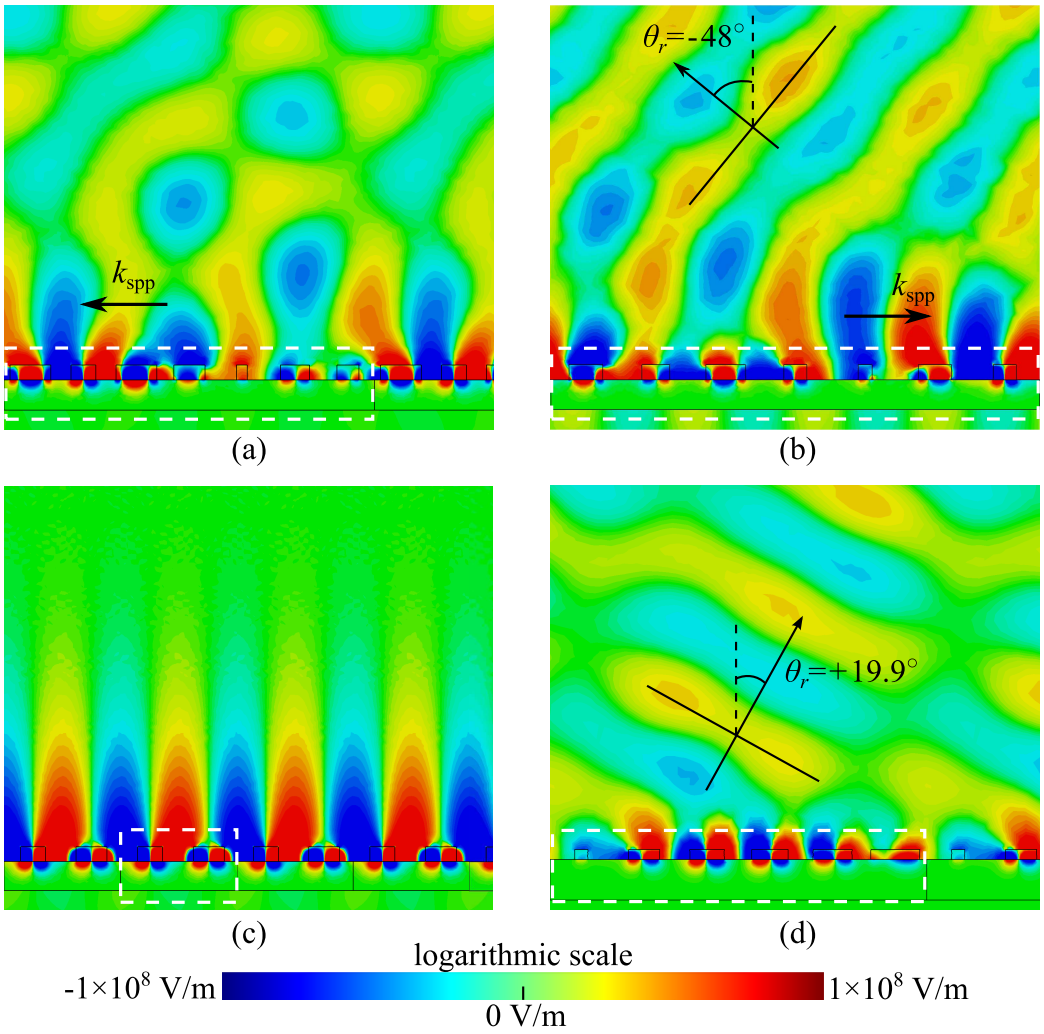

Figure 4.9. Simulated E-field component perpendicular to the silver surface for the four design cases. All cases are labelled in Fig. 4.4(a) and share the same amplitude and geometry scale. The white dashed boxes indicate a single subarray. (a) Case 1: Leftward SPP launcher in the non-deflection zone. 34% of the incident power is reflected while 66% is accepted including power coupled into SPPs and dissipated inside materials. (b) Case 2: Rightward SPP launcher in the deflection zone. 54% of the incident power is reflected while 46% is accepted. A deflection wavefront is visible at $-48°$ from the normal. (c) Case 3: A clear standing waves is observed on this structure with 67% of the incident power is reflected while 33% absorbed. (d) Case 4: The reflectarray in (Zou *et al.* 2013) is reproduced with without further optimisation. A clear deflection is observed at 19.9° off normal. 47% of the incident power is accepted mainly dissipated inside materials while 53% is reflected.

Figure 4.9 shows for Cases 1, 2, 3 and 4 the simulated E-field component normal to the interface. This particular field component contains most features of the launched plasmonic waves and includes some features from the scattered field. As shown in

Fig. 4.9(a) and (b), both of the TiO_2 based arrays for Cases 1 and 2 show clear directional SPP launching, with a distinctive difference in the scattered field. In addition to rightward directional launching, the result of Case 2 also shows a clear deflection wavefront at $-48°$, close to the theoretically calculated angle of $-48.6°$. In comparison, the result of Case 1 only shows leftward directional SPP launching and weak free-space scattering with no clearly defined direction. Furthermore, the simulations show that the accepted power, which includes power coupled into SPPs and power dissipated inside the materials, are 66% for Case 1 and 46% for Case 2. Simulation of Case 3 shows no directional SPP launching but only the expected standing waves. In this case, 67% of the incident light power is reflected while the rest is coupled into standing waves and dissipated as heat in the silver and TiO_2. This effect suggests (after optimisation) a possible application of DR arrays to perfect absorption. Case 4 is the simulation reproducing the reflectarray reported in (Zou *et al.* 2013) and the result shows clear deflection at 19.9° offset from normal direction.

The 3D simulation results also reveal some effects not accounted for in the analysis. The non-uniform arrays of DRs on the silver surface are not only excited by normal incident light, but also by the radiation from their neighbouring resonators. This parasitic excitation through mutual coupling introduces an asymmetry (Neugebauer *et al.* 2014) in the excited mode of each resonator. This effect can change the DRs' phases and radiation patterns and as a result, higher order modes are observed in some large DRs. Therefore, the optimisation procedure can yield DR sizes that are dramatically different from the radii found directly from the phase curves computed in a uniform array configuration (Fig. 4.8(a)). Furthermore, intrinsic differences in the elements' radiation magnitude also contribute to a difference observed between the analytical and numerical results. The resonant DRs have larger scattering cross-section than off-resonance DRs. This effect is more obvious when the progressive phase shift is large and can lead to stronger unwanted higher order diffractions and negative impact on SPP launching.

4.5 Conclusion

SPP couplers based on non-uniform DR arrays operating in their fundamental resonant magnetic dipole mode have been proposed. In a non-uniform array, a variation in the size of the DRs can introduce a phase gradient to control the propagation direction

of SPPs. By properly designing the SPP coupler array, optimal SPP launching can be achieved by avoiding energy leakage into deflection orders. The analysis presented in this Chapter provides guidelines for designing efficient and compact SPP couplers.

Chapter 5

Nano-scale TiO_2 Dielectric Resonator Absorbers

AS indicated in Chapter 4, surface plasmon polariton (SPP) forming standing waves can lead to high absorption. In this Chapter, a narrow-band plasmonic absorber based on uniform array of nano-scale cylindrical dielectric resonators (DRs) on a metallic substrate is experimentally demonstrated. Under a normally incident plane-wave excitation, the DRs resonate in their horizontal magnetic dipolar mode, which can be seen as localised plasmonic hot spots. Such a localised resonance also couples incident waves into SPPs bidirectionally, and perfect absorption is achieved by creating SPP standing waves. The simulation shows perfect absorption at 633 nm with a 90% power absorption relative bandwidth of 1.8%, while the measurement demonstrates maximum power absorption of 90% at 636 nm. Both simulation and measurement results are analysed with coupled mode theory. Additionally, further numerical studies elaborate on the dependence of absorption on the resonator size, period, and incidence angle. This design can be scaled to other wavelengths and can be used as components of integrated optical systems.

5.1 Review of metamaterial and plasmonic absorbers

Electromagnetic absorbers are devices that can convert incident electromagnetic energy into heat or other forms of energy efficiently. Ideally, no reflection or transmission of electromagnetic waves are allowed in the working wavelength range (Cui *et al.* 2014, Watts *et al.* 2012). This concept has attracted significant research interests, thanks to the wide range of applications such as energy harvesting (Sai *et al.* 2003, Sergeant *et al.* 2009), thermal emission (Molesky *et al.* 2013, Rephaeli and Fan 2009), light coupling (Hutley and Maystre 1976, Ye *et al.* 2014), and sensing (Bauch and Dostalek 2013, Liu *et al.* 2010).

So far, various approaches towards electromagnetic absorbers have been reported. In the last decade, metamaterial absorbers (Landy *et al.* 2008, Tao *et al.* 2008, Liu *et al.* 2010, Hao *et al.* 2010, Aydin *et al.* 2011) have been extensively studied, with demonstrations from microwave (Landy *et al.* 2008), to terahertz (Tao *et al.* 2008), and optical frequencies (Hao *et al.* 2010). In general, metamaterials are described by the effective medium theory (Smith and Pendry 2006). The existences of electric and magnetic resonances can tune the effective permittivity ϵ and permeability μ such that the effective impedance $Z = \sqrt{\epsilon/\mu}$ can match the free space impedance Z_0, and thereby maximise electromagnetic absorption. Metamaterial absorbers usually are designed by patterning metallic resonators on ground planes with dielectric spacers (Landy *et al.* 2008, Tao *et al.* 2008, Hao *et al.* 2010), where strong electric and magnetic resonances are supported.

At optical frequencies, plasmonic resonators play an important role in electromagnetic absorbers. Plasmonic metamaterials for high absorption usually exploit localised surface plasmon resonances (LSPRs) (Tan *et al.* 1999, Polyakov *et al.* 2012, Søndergaard *et al.* 2012, Zhang *et al.* 2012) and support resonances by multilayer structures (Hedayati *et al.* 2011, Aydin *et al.* 2011, Kats *et al.* 2013). This concept has also been extended to terahertz frequencies (Withayachumnankul *et al.* 2014). Apart from LSPRs, surface plasmon polaritons (SPPs) can also lead to perfect electromagnetic absorption. The first perfect optical absorption based on this principle was demonstrated with gold gratings (Hutley and Maystre 1976). Later, various similar SPP absorbers (Sharon *et al.* 1997, Fang *et al.* 2012) were reported and implemented for integrated optics (Holmgaar-d *et al.* 2009).

In this Chapter, a narrowband plasmonic absorber based on DRs is proposed and experimentally demonstrated. Such an absorber is developed by patterning an array of TiO_2 cylinders on a silver ground plane. TiO_2 is a low-loss dielectric with a loss tangent less than 0.01 in most of the visible frequency range (Zou *et al.* 2013, Palik 1998). The absorption mechanism of the design is different from purely LSPR absorbers or SPP

couplers made of metallic gratings. The DR array resonate locally in their fundamental magnetic dipolar mode, which couples the incident waves into SPP standing waves. This absorber can be co-fabricated with other high-efficiency DR components on the same integrated platform.

5.2 Design and fabrication

The perfect absorption is designed to be at 633 nm for demonstration purpose and can be scaled to other wavelengths. Figure 5.1(a) presents the unit-cell design of the proposed narrowband plasmonic absorber. The silver substrate thickness is 200 nm to prevent any light transmission. Excited by a normally incident plane wave, the DR is intended to resonate as a horizontal magnetic dipole, and can couple the free-space incident waves into SPPs efficiently (Zou *et al.* 2015a). The DR period should be close to one λ_{spp} to ensure SPP standing waves. However, the actual period is shorter due to the retardation effect caused by the presence of DRs. Due to the four-fold rotational symmetry of the unit cell, the absorption is polarisation independent.

The absorber is fabricated with electron beam lithography (EBL). The nanofabrication starts with the preparation of a silicon substrate, which is coated with a 200 nm silver layer via electron beam evaporation (Lesker PVD75). The silver-coated wafer is then spin-coated with an electron sensitive resist (950 PMMA A4) and soft-baked on a hotplate at 180 °C for 90 s. Subsequently, EBL is performed by using a field-emission electron microscope with a Nanometer Pattern Generation System (NPGS)

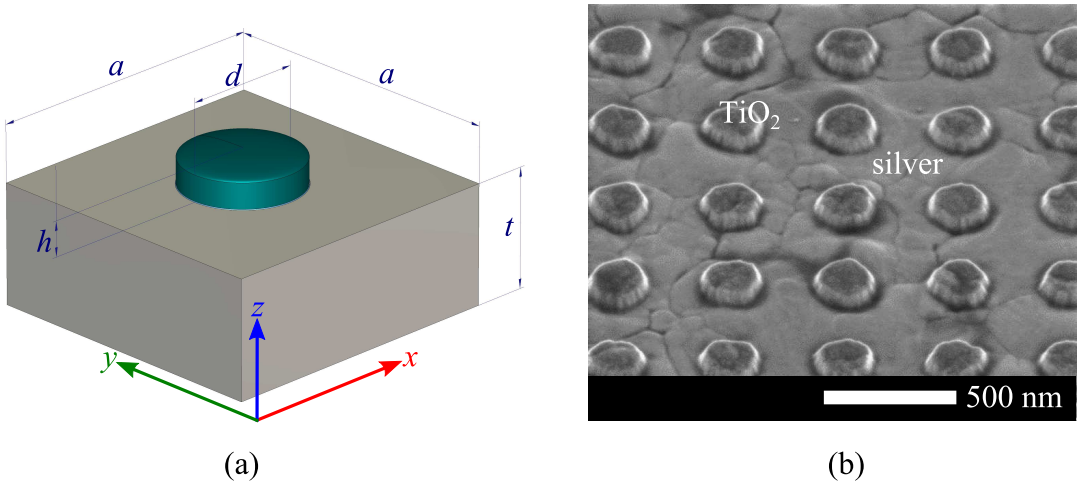

Figure 5.1. Absorber structure. (a) Schematic of the absorber unit cell. $a = 425$ nm, $d = 170$ nm, $h = 50$ nm, and $t = 200$ nm. (b) Scanning electron micrograph of the fabricated absorber sample.

(Nova NanoSEM, FEI Company using NPGS, JC Nabity Lithography Systems). After the electron exposure, the sample is first rinsed in isopropanol (IPA) and subsequently immersed in a methyl isobutyl ketone (MIBK) developer solution with isopropyl alcohol (1:3 MIBK:IPA) for 60 s. Then, to rinse off the MIBK developer, the sample is soaked in IPA and subsequently dried in nitrogen. Now the sample is ready for performing electron beam evaporation (Lesker PVD75) of TiO_2. After patterning TiO_2 resonators, lift-off is performed by soaking the sample in acetone for 1 h and then rinsed with IPA. Finally, the sample is dried using compressed nitrogen. In order to achieve the desired crystalline phase of the TiO_2 DRs, the sample is annealed at 600 °C in vacuum for 2 h. Figure 5.1(b) presents a scanning electron microscopy image of the fabricated sample.

5.3 Simulation and measurement results

First of all, numerical simulation of the absorber structure is performed with the frequency-domain solver in CST Microwave Studio. Floquet port excitation and unit cell boundary conditions are adopted. The normally-incident excitation is set to be linearly-polarised in the x-direction. The red line in Fig. 5.2(a) presents the simulated absorption spectrum, which demonstrates perfect absorption at the designed 633 nm. The 90% relative power absorption bandwidth is 1.8%. There is also a weak absorption peak resulting from a higher-order resonance of DRs at 535 nm. Figure 5.2(b, c) demonstrate the simulated E-field distributions of the absorber design at 633 nm. As shown, the DRs resonate strongly as horizontal magnetic dipoles, which couple the normally incident waves into SPPs in both the positive and negative x directions. The SPP standing waves resulting from interference can also be observed. The simulation also reveals that 74.2% of the incident power is dissipated in silver while 25.8% of the incident power is lost in the TiO_2 cylinders at 633 nm.

To examine the optical performance of the fabricated sample, the absorption spectrum of the absorber sample is measured and compared with simulation results. Figure 5.3 presents the photo of the measurement setup with the corresponding schematic shown as the inset. A tungsten halogen lamp is selected as the white light source, and the radiation passes through a polariser for x-polarised incidence. The light is then directly filtered by a 20 μm pinhole. The setup creates and ensures a near-Gaussian beam with a very small beam waist and a small divergence angle (Ye *et al.* 2014). After passing through a 50:50 beamsplitter, the white-light beam is focused by a 10× microscope

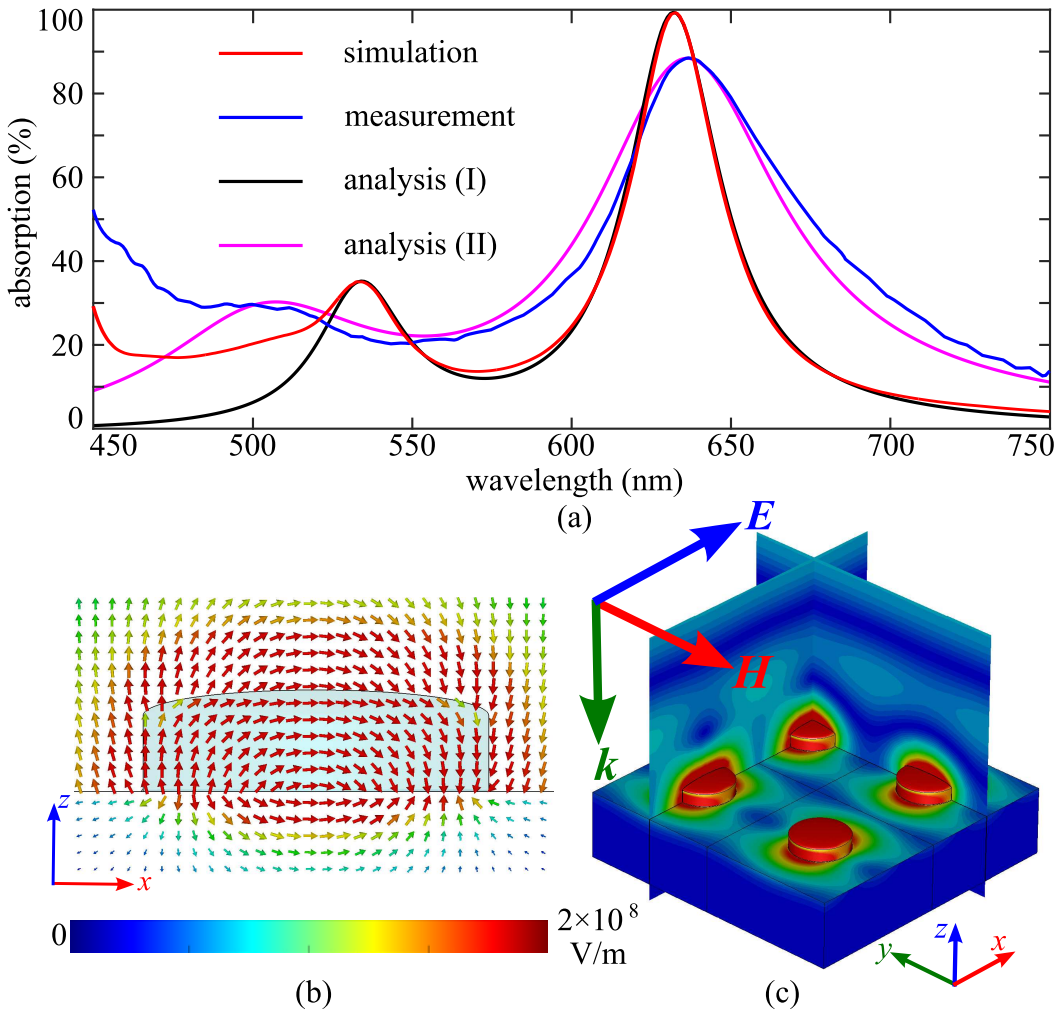

Figure 5.2. Simulation, measurement, and fitting analytical results. (a) The red line and the blue line are the simulated and measured absorption spectra of the plasmonic absorber. The black line (Q_{a1}=40, Q_{r1}=32, Q_{a2}=147, Q_{r2}=15) and the magenta line (Q_{a1}=29, Q_{r1}=13, Q_{a2}=85, Q_{r2}=6.7) are the analytical results fitted to the simulation and measurement results respectively. (b, c) Simulated E-field of the absorber design at 633 nm under x-polarised normal excitation. (b) and (c) show fields on the array and the DR cross-section, respectively.

objective (denoted as 10 × OB in Fig. 5.3) onto the absorber sample. The measured diameter of the focused beam is 85 μm, smaller than the fabricated DR footprint of 100 × 100 μm^2. The calculated Rayleigh length is around 9 mm at 633 nm (Saleh *et al.* 1991). Although aberration occurs, the Rayleigh length ensures approximate normal incidence in most of the visible wavelength range. The reflected light from the sample is collected by a fibre-coupled spectrometer and is normalised with the reflection from a reference silver mirror that replaces the sample. The measured spectrum is presented the as blue line in Fig. 5.2(a). The measured spectrum is in general agreement with the simulated

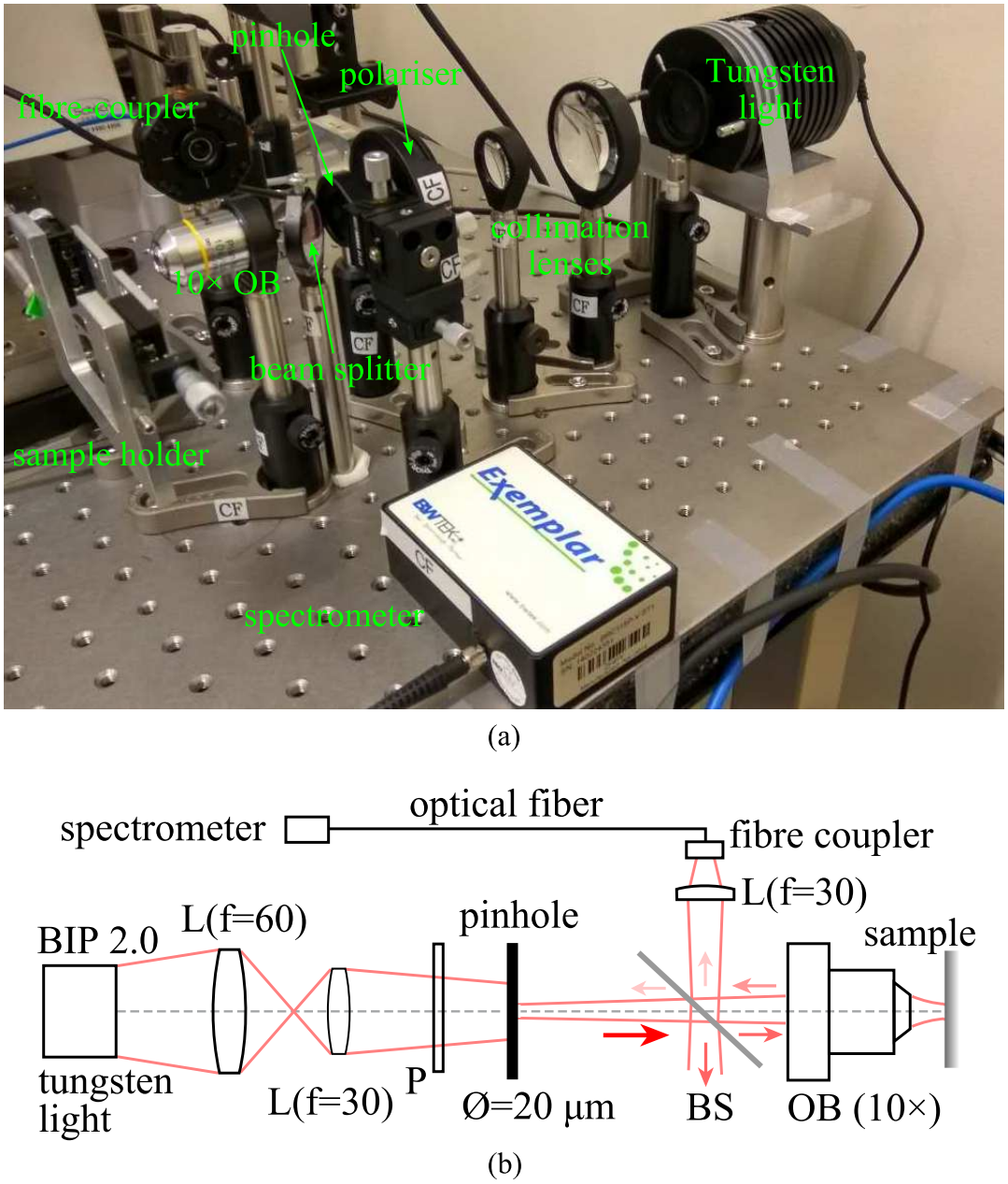

Figure 5.3. White light absorption measurement. Photo (a) of the customised white light absorption measurement setup with schematics illustrated in (b).

results. The maximum absorption is 90% and slightly redshifted to 636 nm due to limited fabrication accuracy. Several factors lead to a broader measured lineshape. The main likely cause is that the materials of the fabricated sample are lossier than materials modeled in the simulation. Additionally, incident light can leak from sample edges as the focused spot size is comparable to the sample size. The small divergent angle of the incident beam and the sample surface roughness also contribute to the lineshape broadening. The higher-order absorption peak is hardly observable in the measurement

and the measured increasing absorption at shorter wavelengths is actually resulted from the intrinsic absorption of TiO_2 (Kuznetsov and Serpone 2009).

5.4 Analysis and discussion

To explain the absorption mechanism in this DR array, the Q factors of the device are modelled based on the coupled mode theory (CMT) (Haus 1983, Qu *et al.* 2015). The plasmonic absorber can be viewed as an array of resonators coupled with free-space incident waves. Its operation can be described by quality factors Q_a and Q_r, where larger Q values correspond to smaller losses. Specifically, Q_a describes the energy trapped in the array and finally dissipated therein, while Q_r describes the radiation loss of the absorber. According to the CMT, the reflection coefficient Γ of the absorber can be expressed as (Haus 1983):

$$\Gamma(\lambda) = \frac{1}{N}\sum_{n=1}^{N}\frac{Q_{an} - Q_{rn} - 2jQ_{an}Q_{rn}\left(\frac{\lambda_n}{\lambda} - 1\right)}{Q_{an} + Q_{rn} + 2jQ_{an}Q_{rn}\left(\frac{\lambda_n}{\lambda} - 1\right)}, \tag{5.1}$$

where Q_{an} and Q_{rn} represent the Q_a and Q_r of the n-th order resonance mode of the DRs, while λ_n designates the n-th order resonance wavelength and λ is the considered wavelength. The weighting of contributions of each mode has already been incorporated into Q_{an} and Q_{rn}, and therefore, the Γ is only normalised to the number of resonance modes N. If only the fundamental resonance mode were considered, it can be expected from Eq. (5.1) that zero reflection at the resonance wavelength occurs at the condition of critical coupling (Bliokh *et al.* 2008) when $Q_a = Q_r$. On the other hand, when $Q_a \gg Q_r$ (over-damping case), magnetic reflection can be achieved (Headland *et al.* 2015). When $Q_a \ll Q_r$ (under-damping case), this corresponds to electric reflection. From Eq. (5.1), the absorbed power can be calculated as $1 - |\Gamma|^2$. We only consider the first two resonance modes (i.e., N=2) and fit the model to the simulation and the measurement results in Fig. 5.2(a). At 633 nm where the fundamental resonance (n=1) is dominant, although the perfect absorption is achieved in simulation, the corresponding Q_{a1} and Q_{r1} are not equal. The slight difference is caused by the contribution to absorption from the second resonance mode. For the measurement, Q_{r1} is smaller than Q_{a1} at 633 nm. Therefore, the radiation loss should be larger than the dissipation loss. It is also seen that Q_{a1} and Q_{r1} deduced from a best fit to the measurement are less than those from the simulation. It implies that the actual dissipation and radiation losses are larger than expected. An increase in the dissipation loss can be ascribed to the

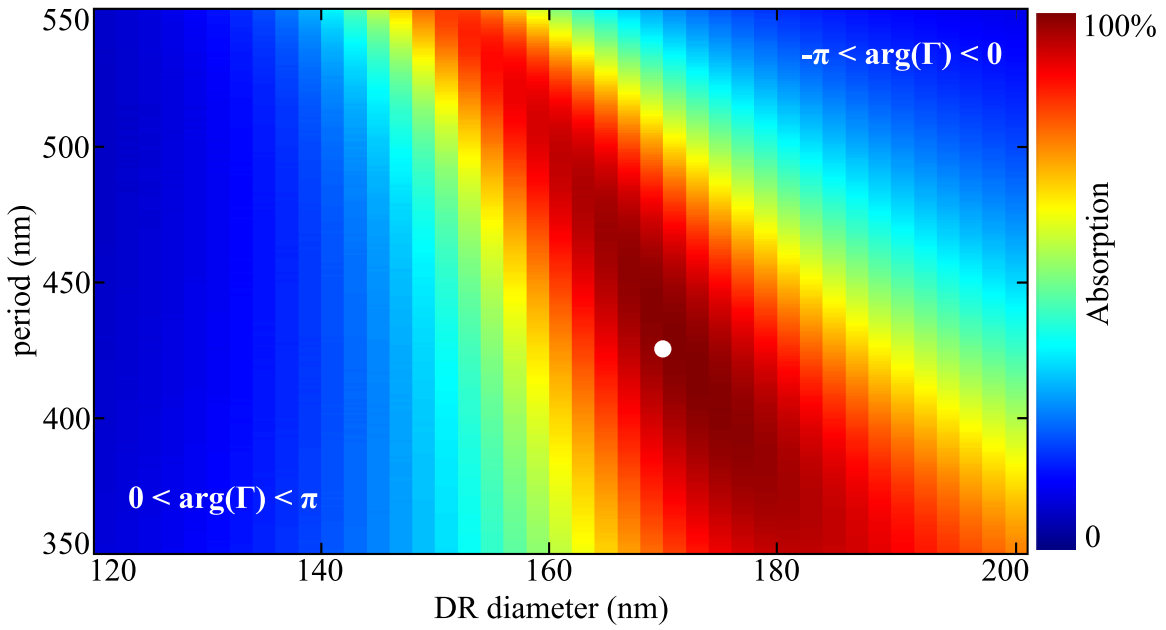

Figure 5.4. Absorption and reflection phase maps. Absorption (%) at 633 nm of a uniform TiO_2 DR array on a silver substrate when varying the DR diameter and period. The white dot marks the fabricated sample.

higher material loss of the fabricated sample than the modelled materials. Additionally, an increase in the radiation loss is mainly caused by the stronger scattering from the rough surfaces of the fabricated sample and light leakage from sample edges. As a result, the measured spectrum does not show perfect absorption at the main peak and the lineshape is broader than the simulated one. Similar analysis and interpretation can also be carried out at the second peak (n=2, ~535 nm) where it is seen that Q_{a2} is significantly larger than Q_{r2}. This indicates much greater radiation loss than the dissipation loss. Essentially, the greater radiation loss is because the DR period does not match the second order resonance wavelength, and it leads to a good coupling to radiation. The model shows reduced accuracy at the short wavelength end as only two resonance modes are considered. In addition, the model does not take the material frequency-dependent absorption into consideration.

In order to achieve high absorption, all DRs must be on resonance and the unit cell size must match the SPP wavelength. Therefore, in the following, the influence of the resonator radius and array periodicity on the absorption are studied. Figure 5.4 summarises the simulated absorption map with varying DR diameter and period at 633 nm. In Fig. 5.4, the red band in the graph demonstrates a region of high absorption, whereas the central area corresponds to both a strong DR resonance and perfect SPP

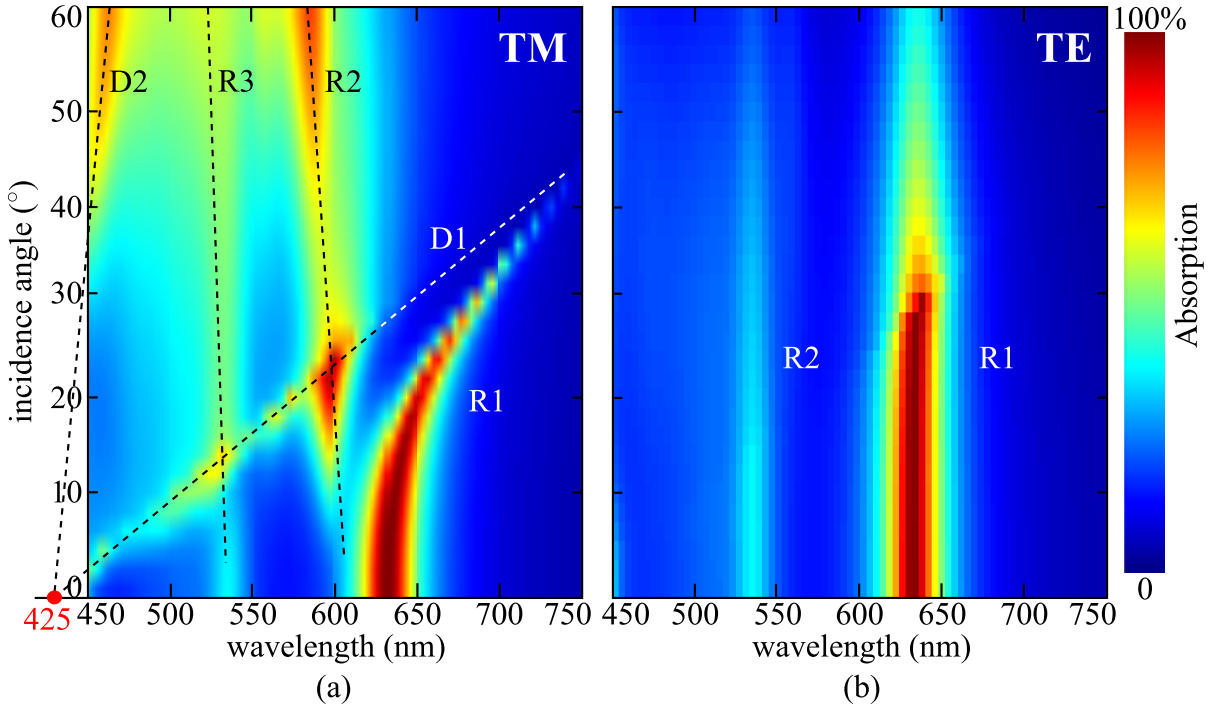

Figure 5.5. Simulated power absorption under oblique incidence. "R" and "D" label resonances and diffractions respectively. The wavelength of 425 nm corresponds to the unit cell size. Power absorption under (a) TM-polarised and (b) TE-polarised excitations are presented.

interference. In this region, the Q_a and Q_r are almost equal and the reflected phase is close to zero. Towards a larger period, the smaller DRs are away from their critical resonance, while towards the shorter period, higher order resonances can occur and complicate the SPP interferences. In both cases, the discrepancy between Q_a and Q_r increases and lead to reduced absorption. The DR arrays corresponding to the blue region are off-resonance, which translates into low dissipation loss and high radiation loss. At the left side of the red band, the phase of Γ is between 0 to π, while at the right side of the red band, the phase of Γ is between 0 to $-\pi$.

Figure 5.5 presents the visible light absorption spectra of the designed plasmonic absorber under oblique incidence angles for both TM and TE polarisations. In general, the figure shows that the absorption performance is more stable under the TE polarisation than under the TM polarisation. In the figure of TM polarisation, several orders of resonance (R) and diffraction (D) can be observed as the incidence angle varies. R1 labels the fundamental magnetic resonance of the DRs for the high absorption. R1 maintains stable absorption when the incidence angle varies within 10°, while it quickly redshifts and converges to the first order diffraction D1 as the incidence angle increases. R2 presents an asymmetrically excited magnetic dipole mode, only accessible at oblique incidence

and with asymmetrical reflections from adjacent resonators. R3 labels a higher-order magnetic resonance mode. Increased absorption is seen when D1 crosses R2 and R3 (Bitzer *et al.* 2009). Finally, D2 is the second order diffraction peak. Interestingly, in the wavelength region where D2 occurs, a negatively-matched resonance breakdown (Zou *et al.* 2015b) occurs, where the TiO_2 permittivity is negatively-matched with the real part of the permittivity of silver. In this case, the DRs can no longer resonate (as the case in Fig. 3.6(d)), and the array works only as grating. High absorption occurs when the DR period matches the momentum difference between SPPs at silver-air interface and free space waves. Under TE polarisation, as the incident *E*-field is parallel to the absorber surface, the absorption is more stable to angle variation than that under TM polarisation. It is seen that the absorber demonstrates over 90% absorption at around 633 nm up to 30°. Due to the transverse incident *E*-field, the coupling between free space waves and SPPs is strongly suppressed at large incident angles, and thus, less resonance and diffraction modes are observed.

5.5 Conclusion

In conclusion, a narrowband plasmonic absorber at 633 nm has been experimentally demonstrated. This absorber is based on a uniform array of TiO_2 DRs on a silver substrate. The design relies on resonant nano-scale DRs to couple incident waves into SPPs and achieves high absorption by SPP interferences. Coupled mode theory analysis on Q factors has been applied, which revealed the relation between the dissipation and radiation losses. The resonator size and array periodicity are important for achieving resonance and proper excitation of SPP standing waves. Under oblique incidence, the plasmonic absorber performance is more stable under TE polarisation than the TM polarisation. This study explored applications of nano-scale DRs in the visible frequencies and can be applied for sensing, filtering and integrated optics.

Chapter 6

Mechanically Tunable All-Dielectric Metasurfaces

DEVICES that manipulate light represent the future of information processing. Flat optics and structures with subwavelength periodic features (metasurfaces) provide compact solutions. The key bottleneck is efficiency, which has been demonstrated with significant improvement by replacing metallic resonators with dielectric resonators (DRs). To extend the functionalities of dielectric metasurfaces to real-world optical applications, the ability to tune their properties becomes important. In this chapter, a mechanically tunable all-dielectric metasurface is experimentally demonstrated. Such a metasurface is made by embedding an array of DRs in an elastomeric matrix. The optical response of the structure under a uniaxial strain is analysed by mechanical-electromagnetic co-simulations. It is experimentally observed that the metasurface exhibits remarkable resonance shifts. Analysis using a Lagrangian model reveals that strain influences the near-field mutual interaction between resonant dielectric elements. The ability to control and alter inter-resonator couplings will position dielectric metasurfaces as functional elements of reconfigurable optical devices.

6.1 Introduction

Next generation optical devices require components that are compact, efficient, and reconfigurable. At visible wavelengths, conventional optical components are usually based on geometrical optics, rendering them bulky. Optical metasurfaces seek to revolutionise realisation of optical components by utilising planar thin film layers of sub-wavelength resonant elements (Yu and Capasso 2014, Kildishev *et al.* 2013). Metasurfaces allow us to engineer phase discontinuities across the thin film interfaces (Yu *et al.* 2011). This concept breaks the dependence on phase retardation arising from optical path length in bulky optics and thus allows us to realise exotic functionality, including anomalous reflection and refraction (Sun *et al.* 2012b, Li *et al.* 2015), or broadband polarisation conversion (Yang *et al.* 2014b). As such, metasurfaces promise unparalleled applications in sensing (Kildishev *et al.* 2013), imaging (Huang *et al.* 2013), and communications (Wu *et al.* 2006).

To harness the functionality of metasurfaces for real-world applications, the ability to tune their response becomes important (Zheludev and Kivshar 2012). The inherent resonant nature of metasurfaces allows their electromagnetic responses to be tuned in many different ways. For instance, different resonance modes (Prodan *et al.* 2003) can be tuned by changing resonators relative orientations (Liu *et al.* 2009, Powell *et al.* 2011) or their geometries (Meinzer *et al.* 2014). The metasurface tunability can also be achieved by manipulating the near-field interactions via varying unit cell periods (Powell *et al.* 2010, Withayachumnankul *et al.* 2012, Sersic *et al.* 2009, Li *et al.* 2013). Other methods to achieve tunable metasurfaces or metamaterials include the use of phase-change materials (Driscoll *et al.* 2008, Seo *et al.* 2010), voltage-controlled coupling (Benz *et al.* 2013), and thermal stimulus (Ou *et al.* 2011). Incorporating resonant elements on stretchable substrates enables mechanical tuning of the optical responses of metasurfaces (Pryce *et al.* 2010, Aksu *et al.* 2011, Millyard *et al.* 2012). Additionally, in many metasurface designs, nonlinear materials have been introduced into resonant electromagnetic fields to enhance tunable higher-order harmonic generation (Boardman *et al.* 2011, Poutrina *et al.* 2010).

Apart from the tunability, efficiency is another factor to consider for metasurface in real-world applications. In the last few years, a number of metasurfaces made of DRs have been demonstrated for efficient light manipulations (Yang *et al.* 2014b, Zou *et al.* 2013, Zou *et al.* 2015a, Zou *et al.* 2014, Zou *et al.* 2016, Filonov *et al.* 2012, Staude *et al.* 2013, Decker *et al.* 2015), which have been reviewed in Chapter 2. Recently, Sautter *et al.* (2015)

have demonstrated an all-dielectric metasurface made of cylindrical silicon DRs covered by a nematic liquid crystal. By changing the operation temperature, the material phase of the liquid crystal and thus the near-field interactions of the resonators operating in magnetic and electric modes are altered, resulting in a demonstrated tunability of the all-dielectric metasurface.

In this Chapter, a mechanically tunable optical metasurface is proposed and experimentally demonstrated. The metasurface is made of an array of uniform TiO_2 (anatase) cylindrical DRs embedded in an elastomeric matrix. The elastomeric matrix, or more specifically polydimethylsiloxane (PDMS), is commonly used in stretchable technologies (Pryce *et al.* 2010, Seghir and Arscott 2015), as a flexible substrate due to its remarkable elasticity and low optical losses. With recent advances in stretchable electronics fabrication (Gutruf *et al.* 2013), brittle oxides can be integrated into elastomers through a unique transfer technique allowing for high process temperatures (Gutruf *et al.* 2015). Using this technique, a very high resolution of the embedded features can be achieved, limited only by the lithographic patterning techniques. The deformation of the soft PDMS allows for tuning the period of the array without altering the shape of the hard TiO_2 resonators, thus providing a convenient and viable metamaterial tuning method. Such a tuning strategy has been recently reported for tunable coloration based on high-index non-resonant diffraction grating with multi-mode interferences (Zhu *et al.* 2015). Here to analyse the resonant-metasurface design, mechanical and electromagnetic finite-element co-simulations have been adopted and the results have been verified at visible frequencies with measurements performed on a fabricated prototype metasurface. To shed light on the underlying tuning mechanisms, we have analysed the near-field interactions among DRs with a Lagrangian model (Powell *et al.* 2010, Withayachumnankul *et al.* 2012, Sersic *et al.* 2009) to interpret the observed resonance shifts. This work proposes an approach to achieve all-dielectric mechanically reconfigurable metasurfaces that enable the next generation optical devices and adaptive photonic systems.

6.2 Design and simulations

6.2.1 Optical response of unstrained metasurface

The tunable dielectric metasurface consists of a uniform array of cylindrical TiO_2 resonators embedded in an elastomeric PDMS matrix. In the considered frequency range from 450 THz to 600 THz (500 nm to 667 nm), the measured average relative permittivity

of TiO_2 is 5.8 (with measured dispersion data shown in Fig. B.1 of Appendix B), while PDMS has an isotropic relative permittivity of 2 (Mark 2009). As illustrated in insets of Fig. 6.1(a), the cylindrical TiO_2 DRs have a diameter of 190 nm and an overall height of 102 nm (of which the cap height is 32 nm, an inherent property of the lift-off method used in fabrication). The designed periodicity in the x- and y-directions is 408 nm. First of all, the optical response of the unstrained metasurface is analysed through electromagnetic simulation, which is carried out by CST Microwave Studio, using unit cell boundary conditions and Floquet excitation ports (Mias *et al.* 1999). When excited by normally incident plane-wave, the simulated transmission spectrum of the unstrained array exhibits a well-defined electric dipole resonance occurring at 591 nm, as shown in Fig. 6.1(a). It is noted that the sharp peak at 582 nm results from a grating effect associated with the infinite array periodicity. The instantaneous field distributions of

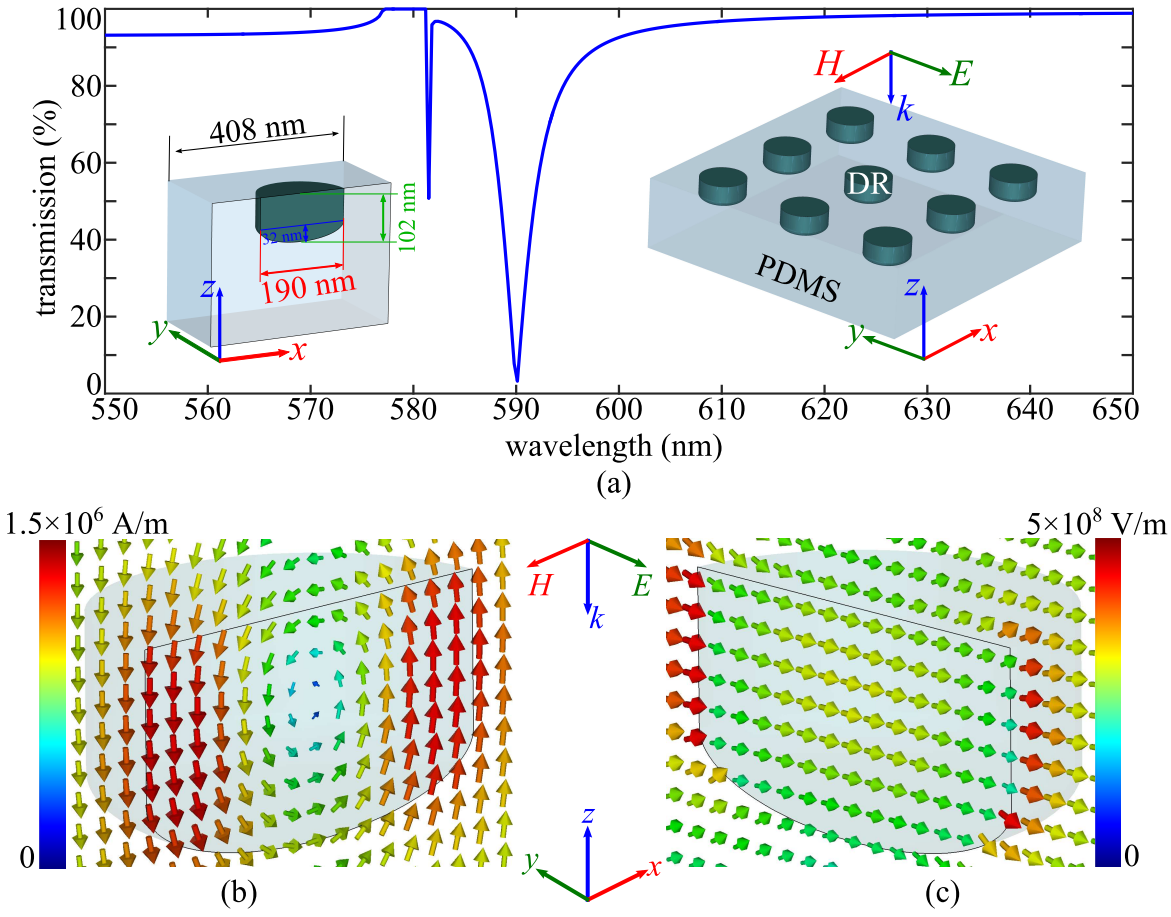

Figure 6.1. Resonant electric dipole response of a DR in unstrained PDMS matrix. (a) Simulated transmission of the unstrained array sample, for a normally incident wave with E-field along the y-direction. Simulated (b) H-field on the x-z plane and (c) E-field on the y-z plane of the resonators in an infinite unstrained array corresponding to the resonance peak in (a).

a cylindrical DR associated with this electric dipole mode, represented in Fig. 6.1(b,c), show the E-field on the y-z plane oscillating in the DR centre with the circulating H-field on the x-z plane.

6.2.2 Mechanically induced deformation and strain

In order to evaluate the effect of external strain, a three-dimensional (3D) mechanical model is created to conduct finite-element method (FEM) analysis of the metasurface. The FEM is carried out using the ANSYS 15 Mechanical tool. The model is built by considering an array of DRs centred on and embedded in the PDMS substrate. Under applied strain along the x-direction, the amount of DR unit cell displacement depends on the mechanical interplay of the hard high-modulus TiO_2 features embedded in the soft low-modulus elastomeric PDMS. To accurately analyse the mechanical deformations in the DR array with reasonable computational complexity, the simulated DR array includes 6×6 unit cells and the PDMS substrate is restricted to 10×5 μm^2 with a thickness of 2.5 μm. The PDMS substrate is then subjected to a simulated mechanical deformation with displacement of 0.6 μm in the x-direction, equivalent to 6% strain for

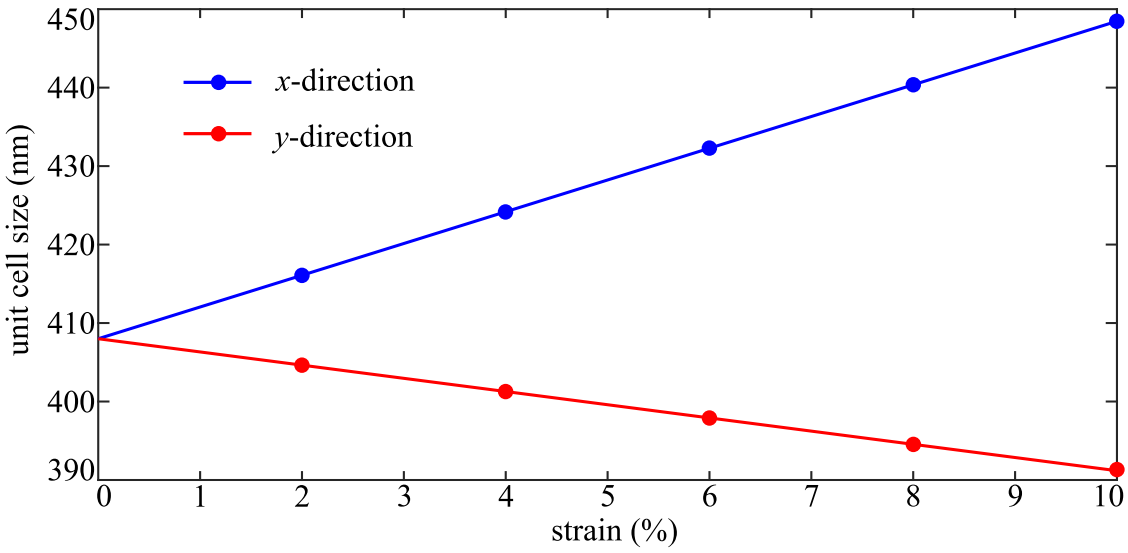

Figure 6.2. Simulation of change in unit cell period upon application of strain along the x-direction. The materials properties used for PDMS are: Young's modulus of 20 MPa (Bowden *et al.* 1998), density of 965 $kg \cdot m^{-3}$ (Nisar *et al.* 2008), and Poisson's ratio of 0.4 (Xia *et al.* 1996). The TiO_2 DRs embedded in the PDMS are 190 nm in diameter and 102 nm in height, with Young's modulus of 1.4×10^6 MPa (Ottermann *et al.* 1996), density of 4,260 $kg \cdot m^{-3}$ (Reddy *et al.* 2012), and Poissons ratio of 0.28 (Mayo *et al.* 1990).

the original length of 10 µm, with detailed simulation parameters included in the caption of Fig. 6.2. Figure 6.2 summarises the mechanical simulated unit cell deformations along the x- and y-directions upon application of uniaxial strain along the x-direction. In order to evaluate the influence of DRs embedded in PDMS, a blank substrate is compared to the DR-embedded structure. The results are displayed in Fig. 6.3, with direct comparison of the total deformation in Fig. 6.3(a) and Fig. 6.3(c) and normalised strain in Fig. 6.3(b) and Fig. 6.3(d). Despite the presence of the embedded TiO_2 features, the result suggests a uniform deformation with no observable distortion of the PDMS substrate in the direction perpendicular to the stretching direction. This response is identical to that of a control substrate without the embedded TiO_2 features. Figure 6.3(d) shows the normalised strain, which is the change in dimension in percentage, occurring in the device. It is observed in simulation that the TiO_2 DRs themselves do not deform under

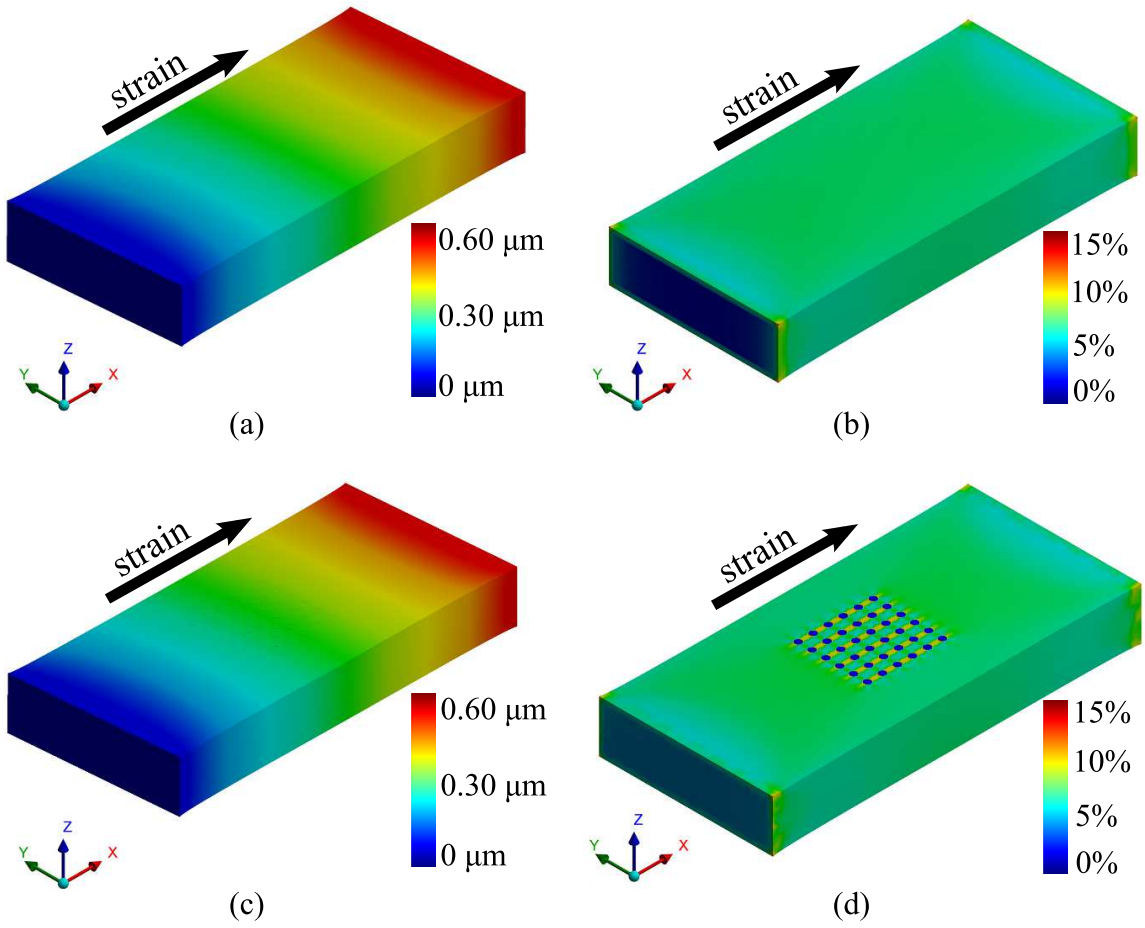

Figure 6.3. FEM mechanical modelling results. Results for 6% applied strain on (a,b) blank PDMS substrate and (c,d) PDMS substrate with embedded dielectric resonators. Three-dimensional maps of total deformation are shown in (a) and (c), with normalised strain shown in (b) and (d).

applied strain due to their high modulus, whilst the soft low-modulus PDMS deforms around them. This mechanical behavior results in a seamless movement of the TiO_2 DRs with the substrate. The resulting unit cell period in the direction parallel to the applied strain can therefore be varied consistently across the sample and proportionally to the amount of strain. The associated change in the unit cell period orthogonal to the applied strain can be attributed to the elastomers intrinsic Poisson's ratio of 0.4 (Xia *et al.* 1996) and is manifested in the simulation results as an induced compression of the unit cell size in the y-direction.

6.2.3 Tunability of optical response under strain

The observable effect of strain from the mechanical simulation, with specific reference to an alteration of the unit cell periodicity, guides the investigation towards the optical response of the dielectric metasurface. Full-wave electromagnetic simulations are carried out with CST Microwave Studio to predict tunability of optical response under strain. The fundamental transverse magnetic (TM) and transverse electric (TE) modes, corresponding respectively to x- and y-polarised waves, excite the structure in the normal direction. All propagating Floquet modes are observed. The background material is set to PDMS with the non-dispersive relative permittivity of 2 (Mark 2009). In the simulations, the unit cell dimensions are changed in accordance with the FEM mechanical simulation (Fig. 6.2) to imitate the effects of applied strain (stretching) along the x-direction together with induced strain (compression) along the y-direction.

As illustrated in Fig. 6.4(a), for the y-polarised excitation, the excited fundamental electric dipoles in the DRs have the E-field transversely coupled and the H-field longitudinally coupled along the applied strain direction. For the x-polarised incidence in Fig. 6.4(b), the converse applies, with the electric dipoles having the E-field longitudinally coupled and the H-field transversely coupled along the applied strain direction. Figure 6.4(c,d) summarise the simulated transmission spectra of the DR array under increasing strain from 0% to 6% for the y-polarised and the x-polarised incident waves, respectively. In general, the resonance peak undergoes redshift under the y-polarised excitation, while experiencing blueshift under the x-polarised excitation. In both figures, the sharp diffraction peak shifts oppositely to the resonance peak, because the incident E-field aligns along the unit cell shrinking direction for the y-polarisation but along the unit cell stretching direction for the x-polarisation. The redshift and blueshift of the dipole resonance imply different dominant effects for transverse and longitudinal

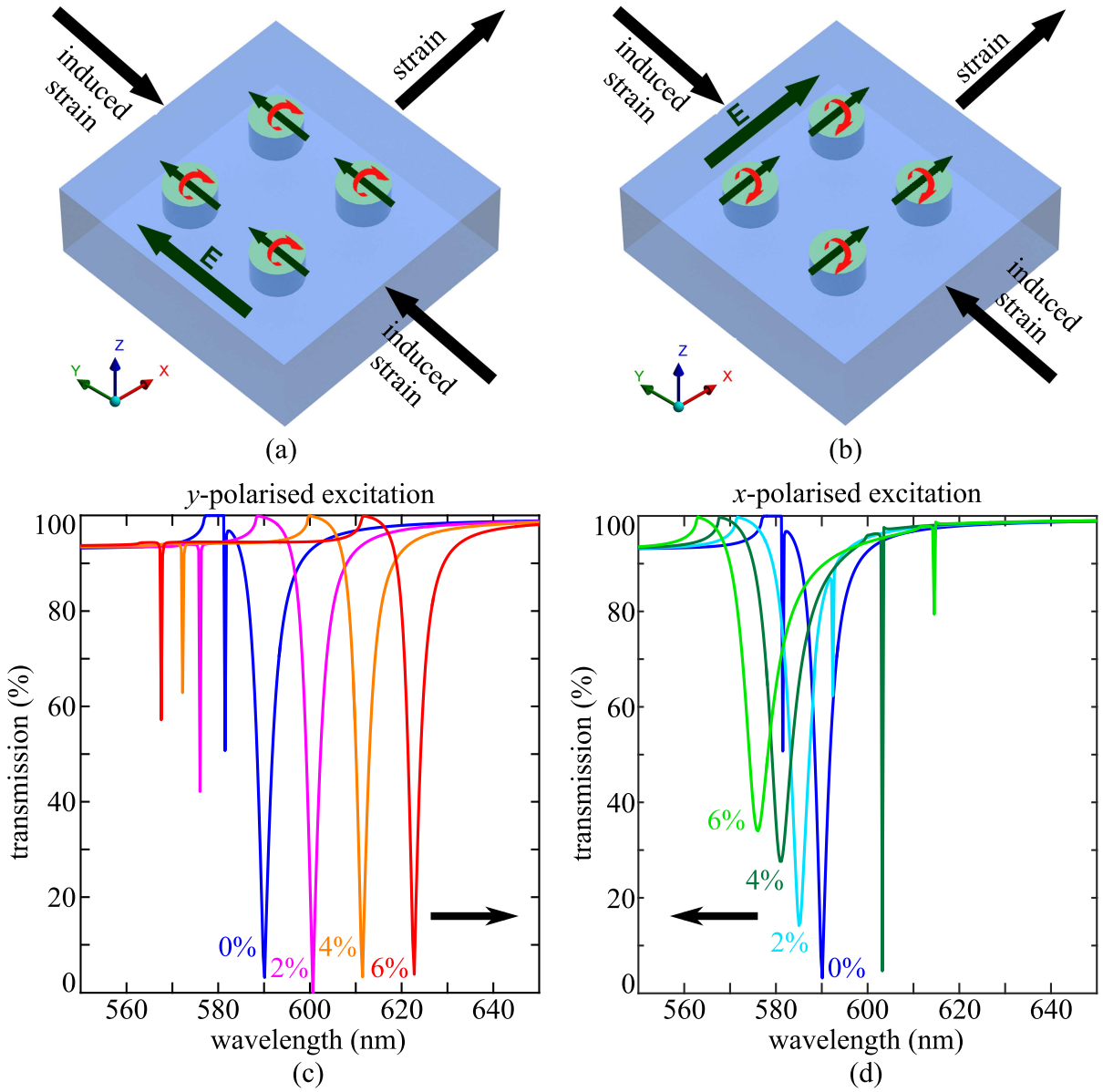

Figure 6.4. Optical simulations of the metasurface of TiO_2 DRs in PDMS. (a, b) Orientation of the y-polarised and x-polarised electric dipoles with respect to applied strain. The large dark green arrow denotes the incident E-field direction. The modal fields in the cylindrical DRs are labeled with the green arrows for the E-field component (parallel to the excited electric dipoles), while the red arrows indicate the circulating H-field component. Simulated resonances under (c) y-polarised and (d) x-polarised excitation for increasing applied strain, with the black arrow denoting direction of resulting resonance shift.

mutual coupling amongst the DRs. A detailed coupling analysis is presented later by using a Lagrangian model in Section 6.5. Here, it is emphasised that the resonance shifting is not from the array edge resonance effects (Tucker *et al.* 2015), since the array is considered to be 2D-infinite in the simulations.

6.3 Fabrication

Figure 6.5(a-f) show a step-wise schematic of the fabrication process used to create the tunable DR array sample. The fabrication process starts with a platinum (Pt) layer deposited by electron beam evaporation on a standard, cleaned silicon wafer shown in Fig. 6.5(a). A 250 nm thick polymethylmethacrylate (PMMA) layer is applied to the platinum-coated silicon wafer via spin coating followed by a hard bake at 180 °C. The electron-beam sensitive PMMA is subsequently exposed using an electron beam lithography system (Nabity EBL system on a FEI Nova SEM equipped with a field emission gun) by writing the negative mask of the DR array in a serial process. The written structures are 190 nm diameter holes with a separation of 420 nm in both the x- and y-directions. The DR array consists of 280×280 periods resulting in a total dimension of 118×118 μm^2. A subsequent immersion in a MIBK developer is used to wash away the regions exposed to the electron beam. The TiO_2 dielectric layer of 102 nm thickness is then deposited by electron beam evaporation shown in Fig. 6.5(b). Subsequently, lift-off is performed in an acetone bath to remove the excess TiO_2 (Fig. 6.5(c)). The lift-off is followed by an annealing step of 600 °C for 2 h in vacuum (Zou *et al.* 2013) to synthesise the anatase phase of TiO_2 for low optical loss. This is followed by the removal of the TiO_2–Pt sandwich from its rigid carrier by casting PDMS (2 mm thick) onto the TiO_2 layer, with a subsequent hotplate cure at 120 °C for 8 min and an immediate peel-off (Fig. 6.5(d)). It is significant to note that the step depicted in Fig. 6.5(d) results in a shrinkage of the PDMS substrate on release from the substrate, due to compressive strain introduced by the curing the PDMS at an elevated temperature (120 °C). This decrease in volume results in a multiaxial compression of around 2.9%. This phenomenon has been well characterised and accounted for in this work, by ensuring the nanofabrication pattern with unit cell dimensions that are larger (420 nm, in comparison to the 408 nm defined by the design). The wafer-sized TiO_2–PDMS device is flipped over onto a silicon carrier and the Pt layer removed by reactive ion etching (7.5 min, 100 W, Ar atmosphere, 70 mTorr working pressure) leaving the dielectric cylinders exposed, as illustrated in Fig. 6.5(e). The device is then carefully lifted off the carrier and diced into 50 mm×50 mm specimen for the ease of measurement (Fig. 6.5(f)). Figure 6.5(g) shows a false-colour scanning electron micrograph (FEI Verios 460L) of a partial view of the DR array.

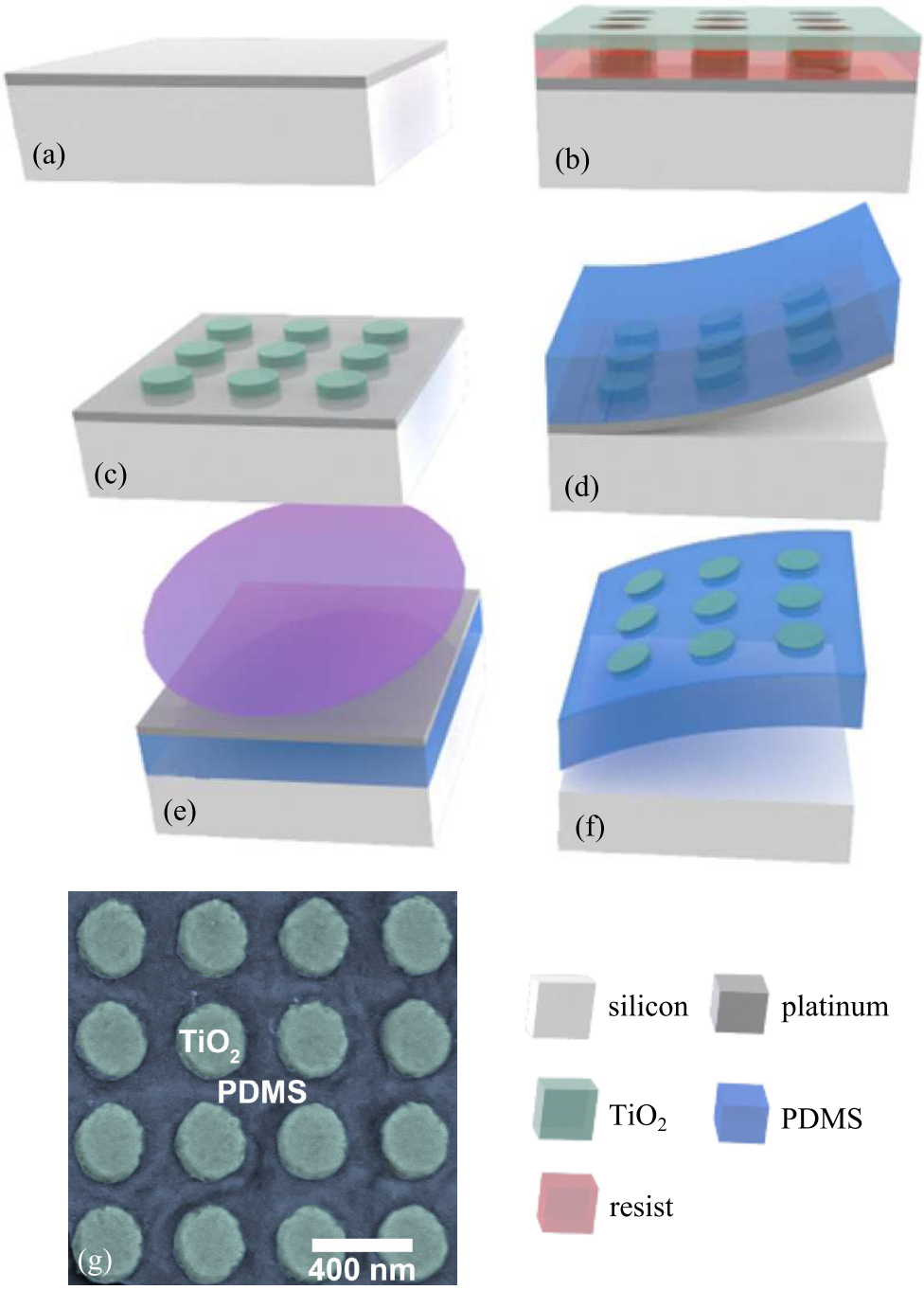

Figure 6.5. Nanofabrication process of dielectric resonator metasurface. (a) platinum deposition; (b) electron beam lithography for nanopatterning and TiO_2 deposition; (c) lift-off removal of TiO_2 and resist with subsequent annealing; (d) spin-coating and curing of PDMS with subsequent peel from carrier substrate; (e) schematic of purple plasma plume indicating platinum layer removal by dry etching; and (f) release to create a tunable metasurfaces. (g) TiO_2 DRs embedded in PDMS imaged with a scanning electron microscope and represented in false colour, where blue indicates PDMS and green for TiO_2.

6.4 Measurement and results

The resonance shifting spectral behaviour is verified via experimental characterisation, using nanofabricated samples and the test setup in Fig. 6.6. A 20 W BWTEK BIP 2.0 tungsten halogen lamp is selected as the white light source. To obtain sufficient incident power, the integration housing sphere is removed so that the lamp illuminates forward directly in a broad angle. A 2″ diameter, 60 mm focal length bi-convex lens (labelled as *collimation lens*) is used to collect and collimate the broadly divergent light into a 40× numerical aperture 0.65 objective. A Newport 5511 sheet polariser on a rotating mount is positioned right before the 40 objective for polarisation selection. Several black paper cards and an aluminum light housing box (not included in Fig. 6.6) are utilised to prevent randomly scattered light. The 40× objective focuses the light beam into a 50 μm pinhole. The measured power of the light from the pinhole is 82 μW, ensuring sufficient signal power over the noise level. An Olympus RMS20X 20× numerical aperture 0.4 achromatic objective is used to focus the light down to 140 μm to excite the DR array sample in its centre. The selection of the 20× objective takes both the beam divergence angle and focused beam size into consideration. The sample is mounted on a stretching stage with a minimum stretching step of 10 μm. The transmitted light is collected by a 1″ diameter, 30 mm focal length plano-convex lens into a SMA905 fibre coupler connected with a BWTEK FPC 600 μm core optical fibre. The fibre guides the transmitted light into

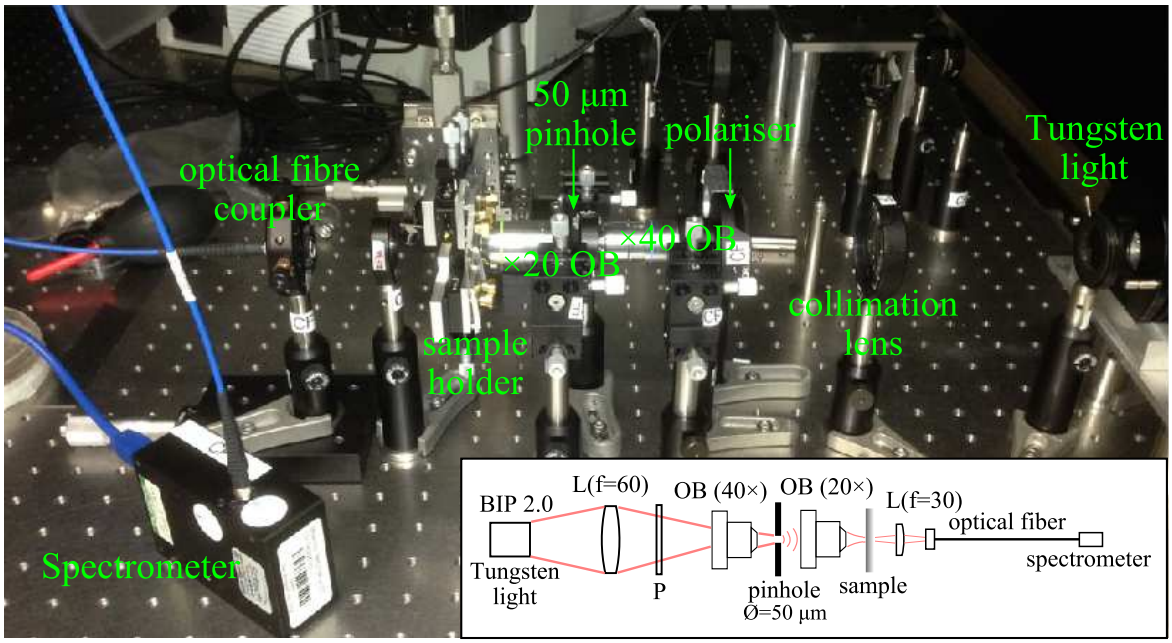

Figure 6.6. Optical characterisation setup of the DR metasurface.

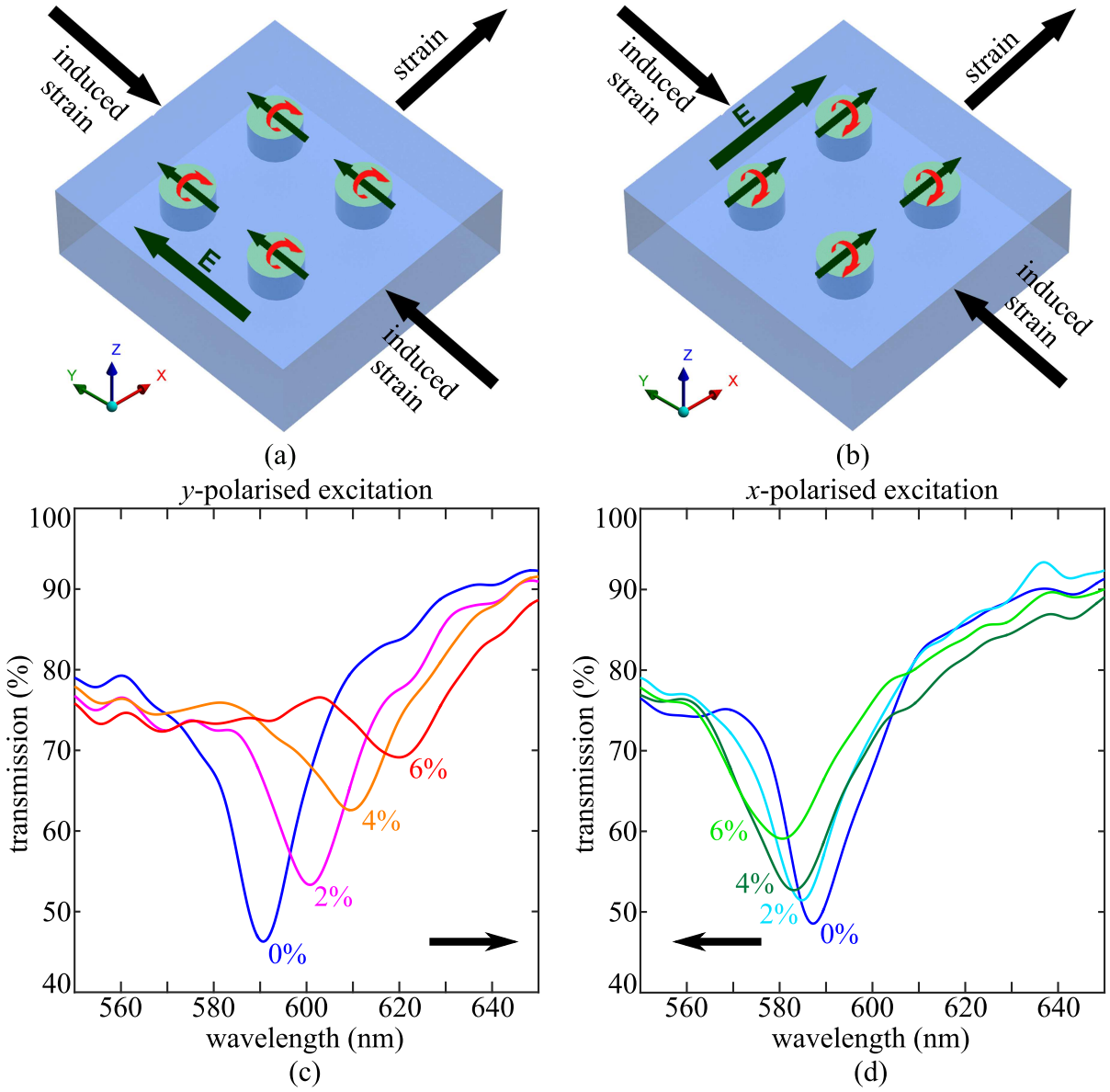

Figure 6.7. Polarisation-dependent transmission spectra of the metasurfaces with increasing applied strain. (a, c) y-polarisation excitation transverse to applied strain. (b, d) x-polarisation excitation parallel to applied strain. Black arrows denote the shifting direction.

the BRC115P Exemplar CCD spectrometer for measurement. During the measurements, a CS01-200 digital microscope is used for observing the sample and for focusing the incident beam onto the centre of the DR array. The sample is measured under 0, 2%, 4% and 6% strain applied along the x-direction with both the x- and y-polarised incident waves.

Figure 6.7(a) presents the measured results under the y-polarised excitation with increasing applied strain. As expected, a clear redshift of the resonance by 30 nm (5.08%)

is observed with the strain increasing from 0% to 6%. The transmission at 591 nm also increases from 46% to 78% as the strain varies from 0% to 6%. Figure 6.7(b) presents the measured transmission under the x-polarised excitation. In this case, the resonance peak slightly shifts by 6 nm (0.96%) towards the blue and the transmission at 587 nm rises from 48% to 77% when the applied strain increases from 0% to 6%. The opposite shifting towards red and blue is caused by the different transverse and longitudinal coupling strengths that will be analysed in greater detail in Section 6.5. The observable resonance arises from the electric dipole mode, since the shifting complies with the simulated electric dipole resonance. Overall, the measured positions of the resonance are in good agreement with simulations. However, the measurement shows a broader resonance linewidth and gradually increased transmission as the applied strain increases. The resonance broadening and weakening is caused by (i) the divergence angle of the focused beam and (ii) the non-uniformity of the resonator shape, both of which result in slightly different modal field distributions among the resonators. The former cause is corroborated by experimental observations made during system alignment, where it has been found that the resonances are further broadened when using a 50× objective (instead of the 20× objective used in the presented results). Further resonance weakening during stretching is mainly attributed to the increased light leakage from the sample edges. It should be noted that the measured weakening strengths are similar in both y- and x-polarised excitations, but are obscured by the baseline variation resulting from increasing intrinsic TiO_2 absorption towards the short visible wavelengths (Kuznetsov and Serpone 2009).

6.5 Lagrangian model analysis

In this section, a Lagrangian model is established to quantitatively investigate the near-field interaction mechanisms amongst DRs and to interpret the numerical and experimental results. For this symmetrical and uniform DR array, the long-distance in-plane interactions are balanced and their impact is significantly less than the near-field interactions (Khunsin *et al.* 2011). Within the considered optical wavelength range, only the fundamental electric dipolar mode is excited due to the small dimensions and moderate permittivity of the TiO_2. Thus, as depicted in Fig. 6.4(a), for the y-polarised excitation, the E-field component of the DR fundamental resonant mode is longitudinally coupled in the y-direction and transversely coupled in the x-direction and vice versa for the H-field. By increasing the applied strain, it can be then inferred

that mainly the E-field transverse coupling and the H-field longitudinal coupling are altered. On the other hand, under the x-polarised excitation, as shown in Fig. 6.4(d), mainly the E-field longitudinal coupling and the H-field transverse coupling are altered with increasing applied strain in the x-direction. Both the impacts of the applied strain and the induced strain are incorporated in the Lagrangian analysis. However, the induced strain has a weaker impact on the near-field couplings than the applied strain since the compression due to induced strain is very limited.

To start the analysis, we first consider a single TiO_2 DR operating in its fundamental electric dipolar mode. It is known that the DR operates via the displacement current. Therefore, the displacement currents and charges can be described as:

$$\text{displacement charge density:} \quad \nabla \cdot D, \tag{6.1}$$

$$\text{displacement current density:} \quad \frac{\partial D}{\partial t} = \dot{D}, \tag{6.2}$$

where D is the electric flux density and Eqs. 6.1 and 6.2 are linked with the continuity equation for the electric current density. From Eqs. 6.1 and 6.2, the displacement charges and current can therefore be expressed as:

$$\text{displacement charge:} \quad Q_d = \int_V \nabla \cdot D dV, \tag{6.3}$$

$$\text{displacement current:} \quad i_d = \oint_S \dot{D} dS, \tag{6.4}$$

where V is the volume of the DR and S is the area of the resonator cross-section orthogonal to the electric dipole direction. Equations 6.3 and 6.4 can be linked with $i_d = dQ_d/dt = \dot{Q}_d$. The Lagrangian model of a single DR is thus formulated as (Powell *et al.* 2010):

$$\mathcal{L} = \frac{L}{2}\dot{Q}_d^2 - \frac{1}{2C}Q_d^2, \tag{6.5}$$

where L and C are effective inductance and capacitance of the DR. The two terms in Eq. 6.5 represent the stored magnetic and electric energy, respectively. Applying the Euler-Lagrangian equation of motion (Morin 2008):

$$\frac{\partial}{\partial t}\left(\frac{\partial \mathcal{L}}{\partial \dot{Q}_d}\right) = \frac{\partial \mathcal{L}}{\partial Q_d}; \tag{6.6}$$

we arrive at:

$$\ddot{Q}_d + Q_d/LC = 0. \tag{6.7}$$

From Eq. 6.7, the fundamental electric dipole mode for a single DR occurs at the frequency $\omega_0 = 1/\sqrt{(LC)}$. For the proposed DR design, a value of $\omega_0 = 142.5$ THz

is obtained from simulation by using unit cell size large enough to approximate a resonator in isolation.

In the following, we analyse the effect of the electromagnetic near-field couplings on the electric dipole resonance in the DR array. From Fig. 6.8(a), the Lagrangian of the

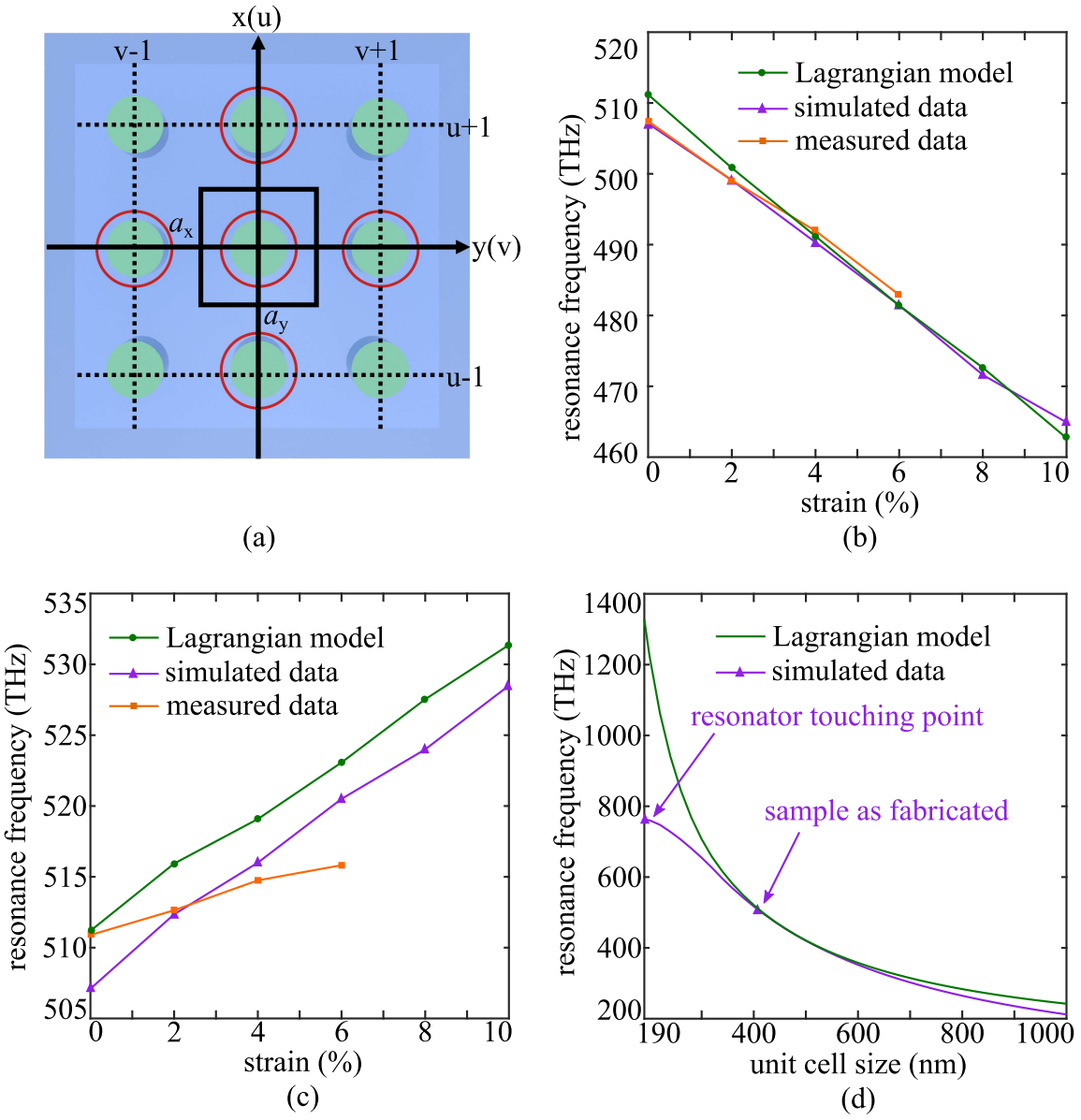

Figure 6.8. Lagrangian model fitting to the resonance frequency. The coupling coefficients are as follows: $h_L = 2.10 \times 10^{13}$ nm^3, $h_T = 2.50 \times 10^{13}$ nm^3, $e_L = 1.40 \times 10^{15}$ nm^3, and $e_T = 1.32 \times 10^{16}$ nm^3. (a) Illustration of near-field coupling among four neighbouring cylindrical TiO_2 DRs. (b) Resonance frequencies when the strain direction is orthogonal to the polarisation. (c) Resonance frequencies when the strain direction is parallel to the polarisation. (d) Resonance frequencies for square unit cells.

coupled resonator system can be expressed as (Withayachumnankul *et al.* 2012):

$$\begin{aligned}\mathcal{L}_x = \sum_{u,v}\Bigg\{ & \frac{L}{2}\left[(\dot{Q}_d)^2_{u,v} - 2\kappa_{HT}(\dot{Q}_d)_{u,v}(\dot{Q}_d)_{u+1,v} + 2\kappa_{HL}(\dot{Q}_d)_{u,v}(\dot{Q}_d)_{u,v+1}\right] \\ & - \frac{1}{2C}\left[(Q_d)^2_{u,v} - 2\kappa_{EL}(Q_d)_{u,v}(Q_d)_{u+1,v} + 2\kappa_{ET}(Q_d)_{u,v}(Q_d)_{u,v+1}\right]\Bigg\}.\end{aligned} \tag{6.8}$$

Equation 6.8 describes the electromagnetic near-field interactions under the x-polarised excitation. The coupling effects described in Eq. 6.8 only take the four nearest neighbouring resonators into consideration, which are marked with red circles in Fig. 6.8(a), and the "+" and "-" signs represent the field attractive and repulsive interactions, respectively. The subscripts for the coupling coefficients κ_{HT}, κ_{HL}, κ_{ET}, and κ_{EL} denote the transverse (T) and longitudinal (L) coupling strengths of the magnetic (H) and electric (E) fields. For the y-polarised excitation, the transverse and longitudinal coupling coefficients together with their signs in Eq. 6.8 should be exchanged. By referring to the dominant term in the near-field expressions for the infinitesimal electric dipole (Balanis 2016), these coefficients can be linked to the unit cell sizes a_x and a_y as well as the wavenumber k in the PDMS via:

$$\begin{aligned}\kappa_{HT} = h_T/(ka_x^3);\ \kappa_{HL} = h_L/(ka_y^3);\\ \kappa_{ET} = e_T/a_y^3;\ \kappa_{EL} = e_L/a_x^3.\end{aligned} \tag{6.9}$$

Equation 6.9 is for the x-polarised incidence, and it is noted that a_x and a_y should be exchanged for the y-polarised incidence. The constants h_T, h_L, e_T and e_L represent the effects of an oscillating current source radiating as an electric dipole in the near-field along transverse and longitudinal directions. Applying the Euler-Lagrangian equation in Eq. 6.6 to the coupled resonator system in Eq. 6.8 yields:

$$\begin{aligned}\left[(\ddot{Q}_d)^2_{u,v} - \kappa_{HT}(\ddot{Q}_d)_{u+1,v} + \kappa_{HL}(\ddot{Q}_d)_{u,v+1}\right] \\ + \frac{1}{LC}\left[(Q_d)^2_{u,v} - \kappa_{EL}(Q_d)_{u+1,v} + \kappa_{ET}(Q_d)_{u,v+1}\right] = 0\end{aligned} \tag{6.10}$$

Since the plane-wave excitation is uniform across the array, the coupled DR array operates in the symmetrical mode. Thus all the resonators have the same charge distributions and they oscillate collectively in phase yielding $(Q_d)_{u,v} = (Q_d)_{u+1,v} = (Q_d)_{u,v+1}$ and $(\ddot{Q}_d)_{u,v} = (\ddot{Q}_d)_{u+1,v} = (\ddot{Q}_d)_{u,v+1}$. Solving Eq. 6.10 yields the resonance frequency of the coupled resonator array:

$$\omega_s = \omega_0\sqrt{\frac{1+\kappa_{ET}-\kappa_{EL}}{1+\kappa_{HL}-\kappa_{HT}}}, \tag{6.11}$$

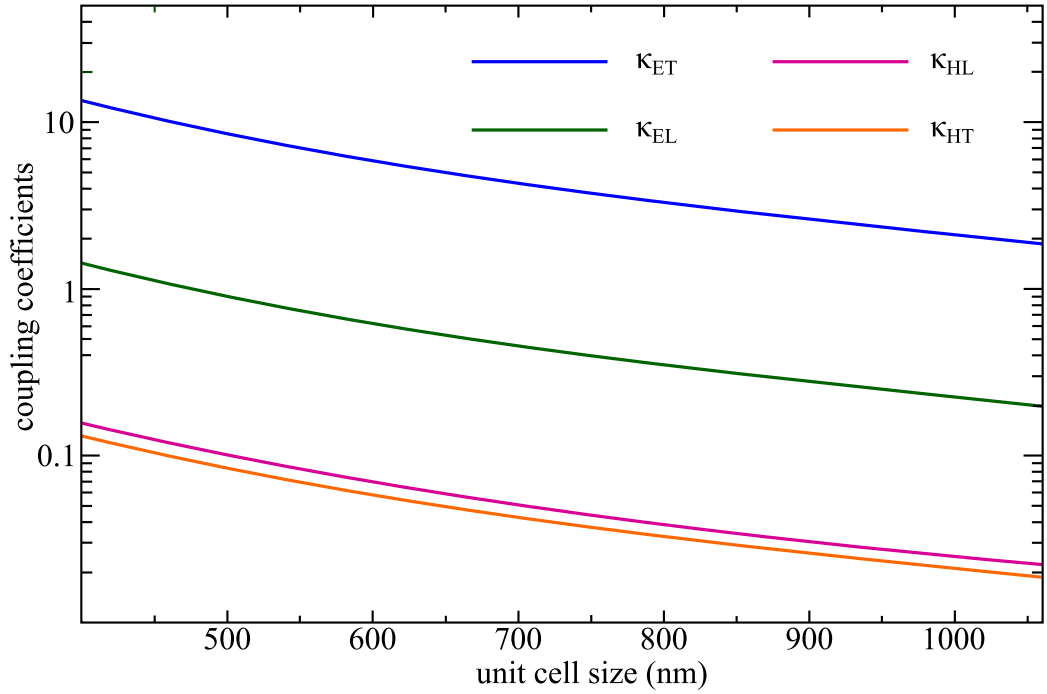

Figure 6.9. Influence of metasurface geometry on coupling coefficients. The coupling coefficients (in logarithmic scale) as a function of the square unit cell size (side length).

where the decoupled resonance frequency $\omega_0 = 142.5$ THz. The unknown constants $h_{T,L}$and $e_{T,L}$ can be obtained by fitting Eq. 6.11 to the simulation and measurement results. From Fig. 6.8(b,c), in general, it can be seen that the Lagrangian results in Eq. 6.11 fits well the simulated and measured results. A small deviation of the measurement results from the simulation and Lagrangian results is seen in Fig. 6.8(c) due to an inherent Poisson ratio variation along the y-direction (Gutruf *et al.* 2015), which affects the x-polarisation results stronger since the dominant transverse coupling is along the y-direction. Figure 6.8(d) presents the simulated and Lagrangian model results for square unit cells with $a_x = a_y$. The simulated unit cell size ranges from 190 nm, where the resonators touch each other, to 1060 nm. It is seen the Lagrangian model results have a good agreement with the simulated results for moderate unit cell sizes ranging from 350 nm to 600 nm. The divergence in the results for smaller unit cells is because the DRs (dipoles) have a finite size, and are not infinitesimally small as assumed in the theoretical model. The limited Lagrangian model accuracy for larger unit cells is mainly because the assumption of near-field interactions in Eq. 6.9 is no longer valid. The coupling coefficients as a function of the unit cell size are plotted in Fig. 6.9 for the case of square unit cells. It is seen that the transverse electric coupling is significantly stronger than the longitudinal electric coupling, while for the magnetic

field couplings, the longitudinal and the transverse coupling strengths are similar and relatively weak. Overall, the electric coupling dominates the near-field interactions of DRs in their electric dipole mode. In effect, the dominant transverse electric coupling results in a clear redshift, when the array is stretched in the direction perpendicular to the polarisation. On the other hand, the resonance undergoes a relatively small blueshift when the strain is applied along the polarisation direction. This quantitative finding sheds light on the dominant coupling mechanism and allows further optimisation of the DR array for maximum tunability.

6.6 Conclusion

This Chapter has presented a mechanically tunable all-dielectric metasurface made of a uniform array of TiO_2 cylindrical resonators embedded in an elastomeric PDMS matrix. Subject to the uniaxial strain, the array has shown a clear resonance shift towards longer wavelengths for the polarisation perpendicular to the strain direction and towards shorter wavelengths for the excitation polarised along the strain direction. With only 6% applied strain, the measured resonance peak shifts 5.08% to red and 0.96% to blue from the base resonance wavelength under different polarisations. This spectral behavior of the TiO_2 resonators has been well predicted with mechanical and electromagnetic FEM modelling. The Lagrangian model has provided an accurate near-field analysis and revealed quantitatively the dominant transverse *E*-field coupling mechanism in the optical DR array. This work has demonstrated an approach to effectively tuning the resonance in all-dielectric low-loss metasurfaces, which suggested a building block for high-efficiency optical devices. The design and analysis provide fundamental understanding on the coupling mechanism of metasurfaces designed with DRs and pave the way for next generation photonic systems.

Chapter 7

Dielectric Resonator Metasurfaces for Selective Thermal Emission

IN this chapter, two designs of metasurfaces for selective thermal emission are proposed and experimentally validated. The designs are based on arrays of metal-loaded dielectric resonators operating at mid-infrared frequencies. The first design demonstrates stable thermal emission at a wavelength of around 8 μm across a wide temperature range. The second design demonstrates strong selective emission from 8 to 13 μm, which is suitable for realising the functionality of radiative cooling. Since the designs are silicon-based, they can be readily integrated with current integrated photonic platforms.

7.1 Introduction

The physical process of thermal radiation is best understood from the concept of blackbody radiation. A blackbody is an idealised physical body that absorbs all incident electromagnetic waves, while its radiation, described by Planck's law, is solely determined by its temperature (Planck 1901). In reality, however, an ideal blackbody does not exist and most objects only have finite absorptivity. The electromagnetic absorptivity of an object can be highly affected by its structure, surface, and material composition. According to Kirchhoff's law of thermal radiation, at thermal equilibrium, the angular and frequency-dependent emissivity of an object is equal to its angular and frequency-dependent absorptivity (Kirchhoff 1860, Schuller *et al.* 2009). Therefore, thermal radiation properties of objects can be engineered by designing and structuring their surfaces at micro/nano-scale (Fu and Zhang 2009).

So far, various nanostructures have been demonstrated for selective thermal emission at infrared (IR) frequencies, where objects at room temperature or higher (up to 3000 K) have their blackbody radiation spectral peak. Among these IR emitters, a number of reported designs are based on photonic crystals (PhCs) (Nagpal *et al.* 2008, Celanovic *et al.* 2008, Rinnerbauer *et al.* 2013). PhCs can demonstrate large bandgaps and allow outstanding control of density of states at IR frequencies, which can be adopted for high absorption (and so emission) at desired wavelengths. Generally, wide-band PhC-based thermal emitters (Fleming *et al.* 2002) are applied to energy harvesting, for example in thermophotovoltaics (TPVs) (Basu *et al.* 2007, Bermel *et al.* 2010), while narrow-band highly-directional thermal emitters are used as infrared light sources for sensing applications (Pralle *et al.* 2002, Chan *et al.* 2006, Inoue *et al.* 2013).

In recent years, selective thermal emission using planar surface structures has attracted extensive research interests. Grating-based optical antennas (Greffet *et al.* 2002, Schuller *et al.* 2009, Klein *et al.* 2008, Puscasu and Schaich 2008) were firstly studied, and have been demonstrated for coherent thermal radiation in the far-field. The coherent emission is mainly created by the decoupling of surface resonance modes, such as surface phonon polaritons, via gratings. Frequency selective surfaces (Puscasu *et al.* 2002, Ginn *et al.* 2010) and metamaterials (Mason *et al.* 2011, Liu *et al.* 2011, Guo and Jacob 2013, Costantini *et al.* 2015) have also been applied to realise thermal emitters. Compared to PhCs, metamaterials can support both local resonances and lattice resonances, which add design flexibility to achieve desired emitting wavelengths, bandwidths, and emission angle spans. With these advantages, metamaterials have been

demonstrated for both ultra-wideband, wide-angle emitters (Argyropoulos *et al.* 2013) and narrow-band, highly directional emitters (Costantini *et al.* 2015).

The possibility of realising selective thermal emission at desired wavelengths opens new perspectives towards a number of promising applications. Apart from the aforementioned TPV emitters and IR light sources, another important application is related to passive radiative cooling (Rephaeli *et al.* 2013, Hossain *et al.* 2015, Hossain and Gu 2016, Chen *et al.* 2016). A high emissivity with an wide angle in the wavelength range from 8 to 13 μm matches a major atmospheric window in the mid-IR range. As such, a thermal emitter can maximise its net heat emission, and can potentially cool an object to a temperature a few to tens of degrees lower than the ambient temperature.

In this chapter, a type of metal-loaded dielectric resonator (DR) metasurfaces is proposed for selective thermal emission. The metal-loaded DRs are fabricated by deep reactive-ion etching (DRIE) on phosphorous-doped silicon wafers (sourced from Sil'tronix), whose optical properties are analysed in Section 7.2. It is noted here that doped-silicon is not a unique solution, while other semiconductors with similar temperature-stable optical properties can also be adopted. The etched patterns are then coated with a thin silver layer (noting that the conducting layer can also be made of other metals such as gold or aluminium) for blocking absorption at wavelengths that are not on resonance. Two metasurfaces based on metal-loaded DRs are proposed in this Chapter. Section 7.3 presents the first design that demonstrates a stable single emission peak at nearly 8 μm when the sample temperature changes from 300 K to 900 K. As a demonstration of possible applications, Section 7.4 presents the second thermal emission metasurface for radiative cooling. This metasurface is designed with two identical rectangular silicon DR arrays oriented orthogonally to each other to allow operation at arbitrary polarisation states. The cooling efficiency analysis shows a high cooling power at room temperature. There are several prominent advantages of this type of thermal emitters. Firstly, as the proposed designs are based on silicon, they are readily available at a low cost, and can be conveniently integrated with current silicon-based integrated photonic platforms. Secondly, due to the micro-scale feature sizes and structure simplicity, the fabrication complexity is largely reduced and the incurred costs are low. Such emitters could alternatively be fabricated over a large area by deep- or extreme-UV photolithography, or nano-imprint lithography (NIL). These advantages suggest that the emitters can be potentially commercialised and manufactured at an industrial scale.

7.2 Optical properties of the doped silicon

As previously mentioned, the proposed metasurfaces are made by etching phosphorous-doped n-type silicon wafers. Doped-silicon is preferred since intrinsic silicon being loss-free at IR frequencies can hardly be used for achieving a high absorption with a desired bandwidth. By changing the dopant concentration, the optical properties of semiconductors can be precisely controlled. The frequency-dependent refractive indices of the selected doped-silicon wafer was measured with an IR ellipsometer at room temperature. The measured results are elaborated in Section B.2 of Appendix B and the corresponding Drude-fitted permittivities at 300 K are presented as red curves in Fig. 7.1. Based on the Drude-fitted results, the carrier concentration of the silicon wafer can be estimated as $n_0 = 7.7 \times 10^{18}$ cm^{-3}, resulting in a calculated electron mobility $\mu_e = 122$ cm^2/(V·s) and a DC resistivity $\rho_{\text{dc}} = 0.0066$ Ω·cm (Baccarani and Ostoja 1975). The calculated plasma frequency of the silicon wafer is $f_p = 48.862$ THz and the collision frequency $\gamma = 8.806$ THz.

Our ellipsometry setup can operate only at room temperature. However, for practical applications it is necessary to understand the impact of temperature on the optical

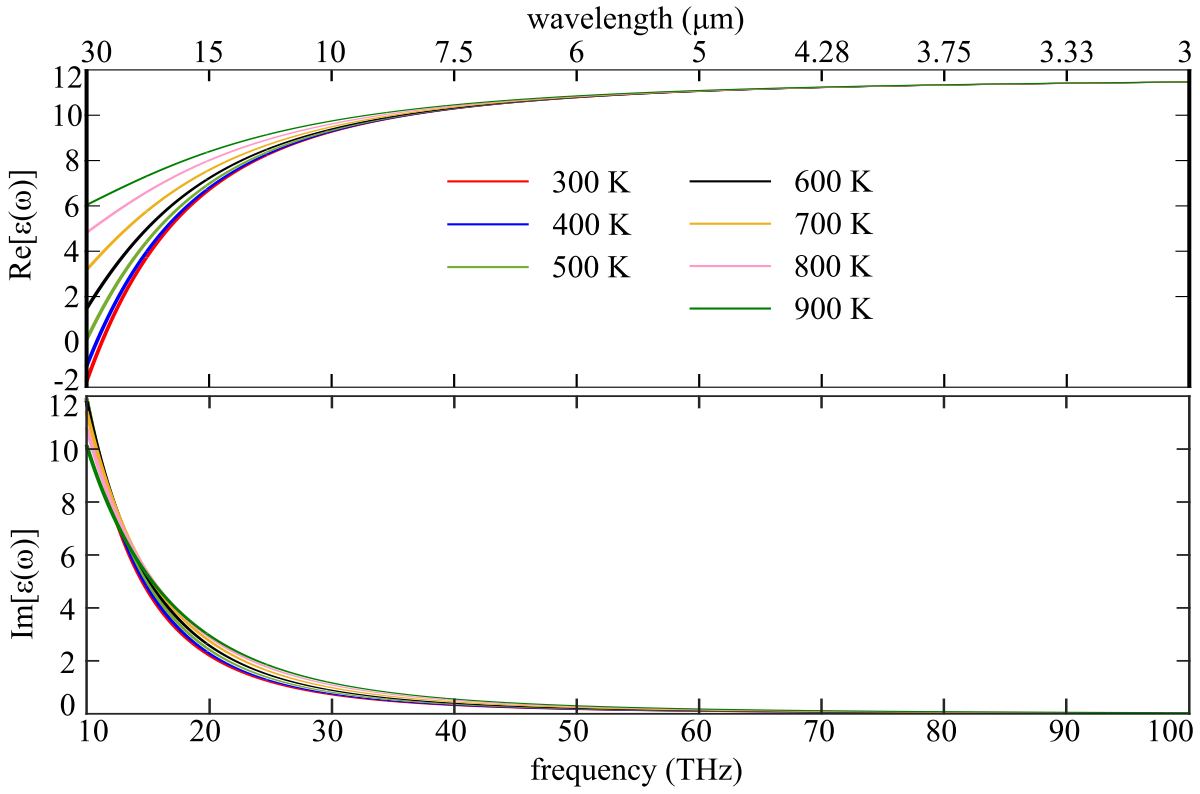

Figure 7.1. Drude-based permittivities of the purchased doped-silicon from 300 K to 900 K.

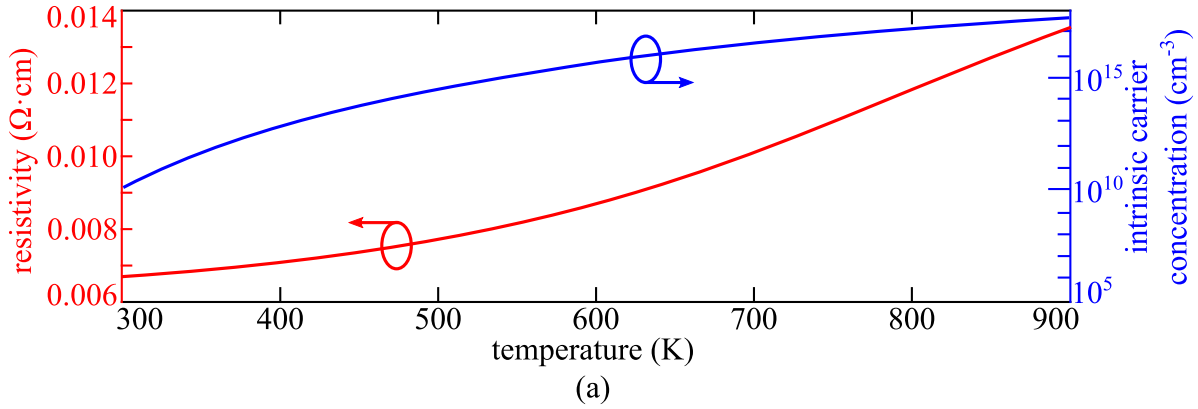

Figure 7.2. Electrical properties of silicon from 300 K to 900 K. The red curve presents the measured resistivity of a phosphorous-doped silicon ($n_0 = 7.8 \times 10^{18}$ cm^{-3}) reported by Chapman *et al.* (1963). The blue curve shows the intrinsic carrier concentration of silicon varying with the temperature according to Neudeck *et al.* (2002).

properties of the doped-silicon wafer. Therefore, the temperature impact is determined from theoretical analysis. Temperature changes mainly affect the carrier concentration n_0 and electron mobility μ_e. It is known that n_0 consists of the intrinsic carriers concentration n_i and donor concentration n_d. The value of n_d is determined by the doping process and generally is not affected by temperature variations. In contrast, the value of intrinsic n_i can increase dramatically as the silicon temperature rises. The blue curve in Fig. 7.2 illustrates n_i of intrinsic silicon varying with its temperature (Neudeck *et al.* 2002). It is observed that n_i is at around 10^{10} cm^{-3} at 300 K, eight orders of magnitude lower than n_0 of the considered silicon wafer. Even up to 900 K, n_i is still an order of magnitude lower than n_0 of the selected wafer. Therefore, the variation in n_i can be considered to have no effect on n_0 from 300 K to 900 K. On the other hand, the temperature impact on the electron mobility μ_e is significant. With increasing temperature, the phonon concentration increases, resulting in a stronger lattice scattering of conduction electrons that can largely decrease μ_e (Cardona and Peter 2005). An accurate value of μ_e can be evaluated via the silicon DC resistivity via $\mu_e = \sigma_\mathrm{dc}/(en_0) = 1/(en\rho_\mathrm{dc})$, where σ_dc is the DC-conductivity and e is the elementary charge. The red curve in Fig. 7.2 presents the measured ρ_dc of a phosphorous-doped silicon (based on a value of $n_0 = 7.8 \times 10^{18}$ cm^{-3}, very close to n_0 of the selected wafer for this design) versus temperature by Chapman *et al.* (1963). As n_0 is unchanged with temperature, μ_e is simply inversely proportional to ρ_dc. The collision frequency γ is also readily known from n_0 and μ_e. Another influence of temperature rise is that the silicon effective mass m_e can also increase, thereby decreasing the plasma frequency. However,

as the increment in m_e is not significant (Green 1990), the variation in f_p is neglected. Based on the analysis above, the Drude-based permittivities of the selected silicon wafer at different temperatures are presented in Fig. 7.1. In general, the variation in the phosphorous-doped silicon permittivities is not significant above 20 THz. It suggests that the proposed emitters could have stable performance across a wide temperature range at mid-IR frequencies. It is worth to mention that silicon has a melting point of 1687 K, which prohibits the use of the proposed emitter at very high temperature.

7.3 Selective thermal emission

With the obtained Drude-based permittivity of the selected silicon, a narrow-band selective thermal emission metasurface is designed, and its performance at different temperatures is examined with simulations. This first design is proposed for discussing the operation principle of the metal-loaded DRs, while a further design is presented in Section 7.4 for realising the practical functionality of radiative cooling. Figure 7.3 presents the unit-cell for the emission metasurface together with its simulated absorptivity (or emissivity) spectra from 300 K to 900 K. The optical simulation is performed with the frequency-domain solver of CST Microwave Studio, using the unit cell boundary conditions and Floquet excitation ports. Due to the four-fold symmetry, the design is polarisation-independent. However, for the discussion, the design is simulated with an arbitrarily chosen x-polarised normally-incident excitation. As shown in Fig. 7.3(a), the simulated absorption spectra from 300 K to 900 K are almost identical, with only a negligible redshift of the resonance peak from 7.83 μm to 7.89 μm, and a slight decrease of the corresponding Q-factor. The stable absorption spectra are expected due to the insignificant change of silicon permittivities with the varying temperature.

Figure 7.3(b,c) illustrates the E-field and H-field distributions of the absorption peak at 300 K. The silver coating is distributed on two different levels separated by the DR's height, creating a gap for virtual magnetic currents. It is seen that the metal-loaded DR resonates as horizontal magnetic dipole with H-field oscillating in the DR centre while E-field concentrating at the gap between the two silver levels. When the DR is on resonance, the resonant fields can extend into the silicon substrate where they are dissipated because of the intrinsically lossy nature of the material. In the considered frequency and temperature range, the skin-depth of the silicon wafer is less than 90 μm, which suggests the minimum wafer thickness that is required in the fabrication to

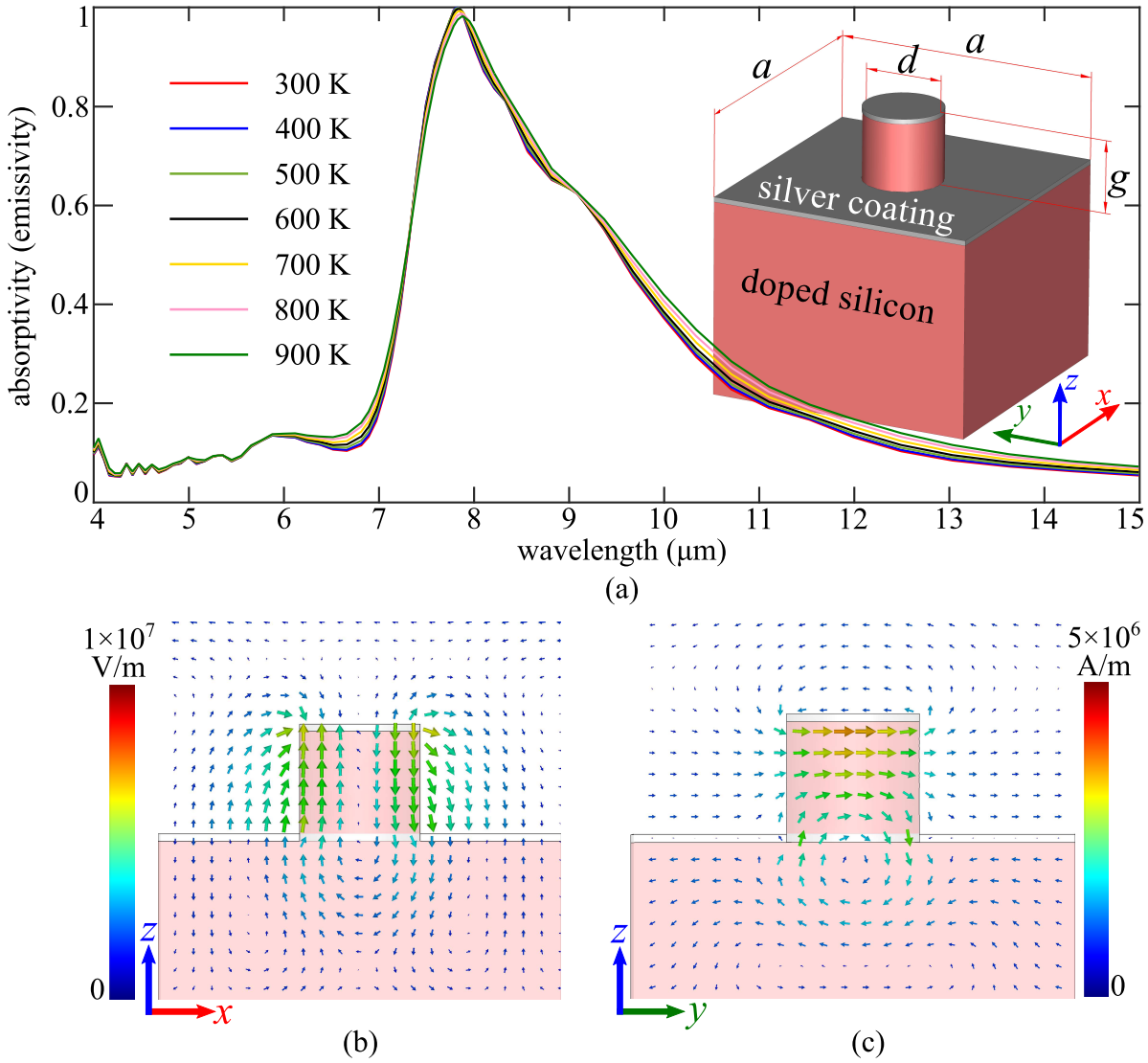

Figure 7.3. Selective thermal emitter and simulation results. (a) Simulated power absorption (or emission) spectra of the designed selective thermal emitter from 300 K to 900 K. A normally-incident excitation with E-field polarised along the x-direction is given. The inset illustrates the unit-cell with parameters: $a = 5.5$ μm, $d = 1.64$ μm, and $g = 1.5$ μm. The coated silver layer is 100 nm thick. The thickness of silicon is assumed to be infinite in the z-direction in simulation. (b-c) Simulated E-field and H-field of the resonance peak at 7.83 μm on the x-z and the y-z cross-sections respectively.

block transmission. It is also revealed in the simulation that at the absorption peak, on average around 80% of the incident power is dissipated inside the silicon while the rest is dissipated in the silver. This in turn suggests that most of the emitted power will also come from silicon.

7.4 Radiative cooling

In this Section, an advanced thermal emission metasurface with selective spectral absorption is demonstrated for realising the functionality of radiative cooling. The general principle of radiative cooling is discussed in the first part. Then the specific design of the radiative cooling metasurface is presented and its cooling efficiency is analysed according to both simulated and measured results.

7.4.1 Principle of radiative cooling

For a radiative cooling structure, the net cooling power, taking all the heat exchange processes into account, can be defined as (Rephaeli *et al.* 2013):

$$P_{\text{net}} = P_{\text{r}} - P_{\text{a}} - P_{\text{nonrad}} - P_{\text{sun}}, \tag{7.1}$$

where

$$P_{\text{r}} = 2\pi \int_0^{\pi/2} \sin\theta \cos\theta \int_0^{\infty} U_{\text{B}}(T_{\text{r}}, \lambda) e_{\text{r}}(\lambda, \theta) \mathrm{d}\lambda \mathrm{d}\theta, \tag{7.2}$$

is the radiative power emitted by the cooling structure and

$$P_{\text{a}} = 2\pi \int_0^{\pi/2} \sin\theta \cos\theta \int_0^{\infty} U_{\text{B}}(T_{\text{a}}, \lambda) e_{\text{r}}(\lambda, \theta) e_{\text{a}}(\lambda, \theta) \mathrm{d}\lambda \mathrm{d}\theta, \tag{7.3}$$

is the amount of the incident atmospheric radiation absorbed by the cooling structure. The angle θ defines the emission direction with respect to the normal direction of the radiative cooling structure surface, which usually faces the zenith direction. The term

$$U_{\text{B}}(T, \lambda) = \frac{2hc^2}{\lambda^5} \frac{1}{e^{hc/\lambda k_{\text{B}} T} - 1}, \tag{7.4}$$

is the spectral radiance of a blackbody at any temperature T according to Planck's law (Planck 1901), where h is the Planck's constant, k_{B} is the Boltzmann constant, c is the speed of light in vacuum, and λ is the wavelength. e_{r} and e_{a} are the emissivities of the cooling structure and the ambient atmosphere respectively. According to Kirchhoff's law of thermal radiation (Kirchhoff 1860), e_{r} can be defined as the absorptivity of the radiative cooling structure at thermal equilibrium. The angle dependent emissivity of the atmosphere can be calculated by $e_{\text{a}} = 1 - t(\lambda)^{1/\cos\theta}$ (Granqvist and Hjortsberg 1981), where $t(\lambda)$ is the atmospheric transmittance in the zenith direction. T_{r} and T_{a} denote the temperature of the cooling structure and the surrounding air respectively.

The third term P_{nonrad} on the right-hand side of Eq. 7.1 represents the non-radiative heat exchange (*i.e.* heat conduction and heat convection) between the cooling structure and its environment. Thus P_{nonrad} can be expressed as:

$$P_{\text{nonrad}} = q(T_{\text{a}} - T_{\text{r}}), \tag{7.5}$$

where $q = q_{\text{cond}} + q_{\text{conv}}$ is the heat exchange coefficient combining contributions from conduction and convection. Metals and silicon are efficient thermal conductors. Therefore, without heat insulation, the non-radiative heat exchange can easily ruin any cooling performance. Quite often, in reported radiative cooling designs (Rephaeli *et al.* 2013, Hossain *et al.* 2015), IR-transparent polyethylene films and polystyrene foams are used as heat insulators. In those cases, a polyethylene films was fixed to the emitting side of the thermal emitter with a small air gap, for suppressing heat convection, while a polystyrene foam was attached to the back side of the cooling structure for reducing heat conduction. However, in practice, the cooling structure should be directly attached to the object that need to be cooled. With heat insulation, the value of q can be limited to a range between 1.0 and 6.9 $\text{W}/(\text{m}^2\cdot\text{K})$ (Hossain and Gu 2016).

The last term P_{sum} on the right-hand side of of Eq. 7.1 expresses the solar input power, which is calculated as:

$$P_{\text{sun}} = \int_0^\infty A_{\text{r}}(\lambda) I_{\text{AM1.5}}(\lambda) \text{d}\lambda, \tag{7.6}$$

where $A_{\text{r}}(\lambda)$ is the absorptivity of the cooling structure at the sun light incidence angle. $I_{\text{AM1.5}}(\lambda)$ is the global tilt solar spectrum with an irradiance of 964 W/m^2 (Rephaeli *et al.* 2013). Usually an IR-transparent solar reflector is also integrated at the top of cooling structures to reflect as much as 97% of the input solar power (Rephaeli *et al.* 2013, Hossain and Gu 2016). In the present design, the 3% absorption of solar irradiance, which is 27 W/m^2 according to Eq. 7.6, is adopted in the daytime cooling efficiency analysis.

7.4.2 Design and simulation

Figure 7.4(a) presents the unit-cell of the proposed radiative cooling metasurface. As shown, the substrate and DRs are made of the phosphorous-doped n-type silicon coated with a 100 nm silver layer. Two identical rectangular DRs are included in one unit-cell, however with orthogonal orientation to each other. As discussed in Section 7.3, a single DR can support horizontal magnetic dipole resonances along either its long side or

the short side, depending on the polarisation of the incident waves. In this case, it is to expect that two resonances will occur at different wavelengths. With the present arrangement, due to the orthogonally orientated DRs, the absorption spectrum of the metasurface is polarisation-independent. Fine-tuning of the dimensions can result in a high-absorption band that matches the main atmospheric transmission window from 8 to 13 µm, and thus makes the design suitable for radiative cooling. Figure 7.5(a) shows the simulated absorptivity (or emissivity) under a normally incident excitation, with a background gray plot presenting the atmosphere transmission spectrum (Gemini Observatory 1992) for comparison. The simulation is performed with the frequency-domain solver of CST Microwave Studio, employing the unit-cell boundaries and Floquet excitation ports. Two absorption peaks are observed at 8.8 µm and 11.3 µm, corresponding to resonances along the short and long sides of the DRs respectively. They form an absorption band generally covering the atmospheric window from 8 to 13 µm. The slightly lower absorption between the two peaks matches the low transmission dip at 9.6 µm. Another absorption peak at around 5 µm, which corresponds to the third-order DR resonance, matches another relatively narrow atmospheric window. The angular-dependent emissivity is critical for the cooling performance. Therefore, the absorptivity the angles ranging from 0 to 90° has been simulated with the result

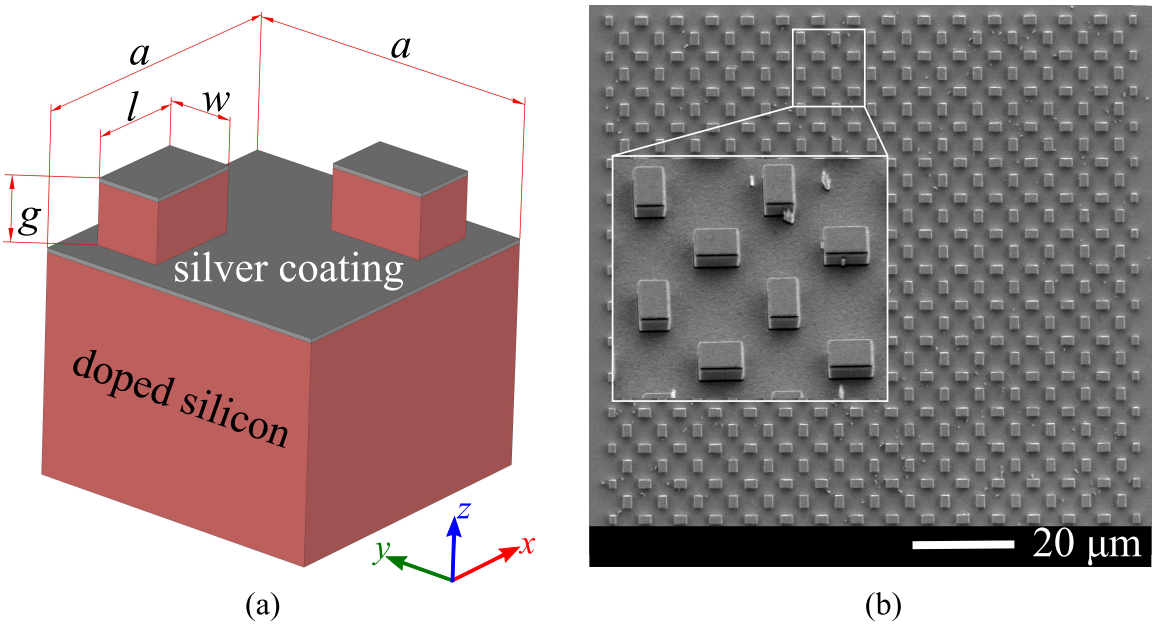

Figure 7.4. Radiative cooling metasurface. (a) The unit-cell of the radiative cooling metasurface is presented with parameters: $a = 6.9$ µm, $l = 2.3$ µm, $w = 1.55$ µm, and $g = 1.5$ µm. The coated silver layer is 100 nm. (b) Scanning electron micrograph of the fabricated sample.

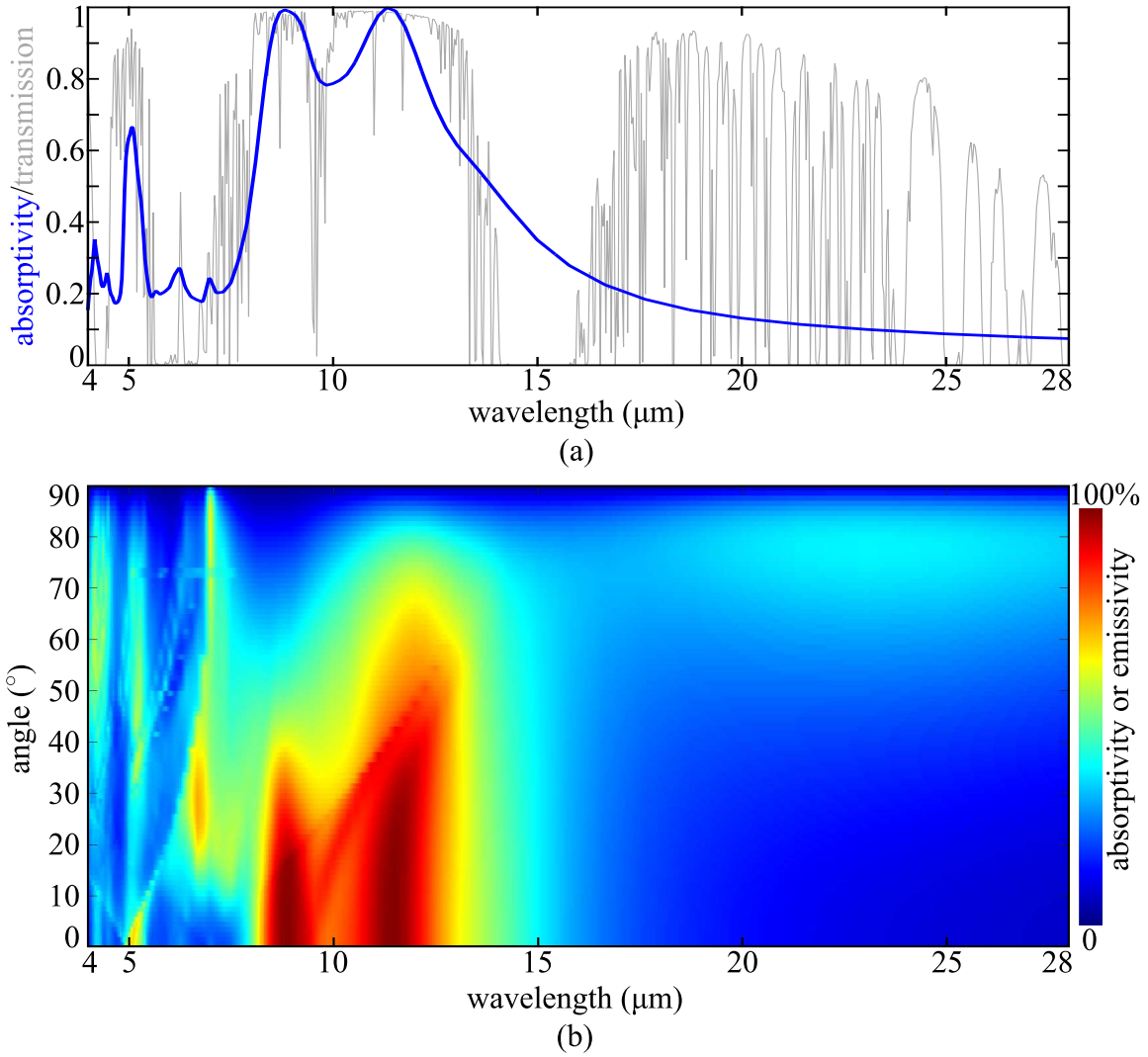

Figure 7.5. Simulated absorptivity (emissivity) of the radiative cooling metasurface. (a) Simulated absorptivity (blue curve) under a normally incident excitation polarised along x-direction. The gray background presents the atmospheric transmission for comparison (Gemini Observatory 1992). (b) Simulated angular-dependent absorptivity (emissivity) of the proposed radiative cooling metasurface. The result is the averaged absorptivity of the simulated absorptivities under TE- and TM-polarised excitations.

presented in Fig. 7.5(b). The result is obtained by arithmetically averaging the simulated absorptivities under TE and TM-polarised excitations, so as to approximate an unpolarised thermal emission. In general, the angular absorption/emission spectrum shows a wide emission angle within the main atmosphere window. Outside of the atmosphere window, the absorption is generally low for all incident angles. This result ensures an efficient and stable radiative cooling performance. In simulation, it is found that the radiative cooling metasurface design demonstrates around 90% reflectivity at visible

frequencies. Although the visible-light absorbtivity is only around 10%, the corresponding solar input power can easily undermine the cooling performance. Therefore, a solar reflector is required above the structure (Rephaeli *et al.* 2013, Hossain and Gu 2016), In this way, only a 3% absorption of the solar input is considered in the analysis of day-time cooling performance.

7.4.3 Fabrication and measurement

A radiative cooling sample is fabricated with electron beam lithography (EBL) for demonstration and testing purposes. The nanofabrication of the metasurface pattern starts with the preparation of the 500 μm thick silicon wafer. The silicon wafer is firstly cleaned with acetone and isopropanol, and dried with high purity, compressed nitrogen. After baking at 120 °C for 10 min for dehydration, the wafer is spin-coated with 200 nm PMMA A4 electron beam resist, and subsequently soft-baked on a hotplate at 170 °C for 5 min. Then the coated wafer is ready for EBL, which is performed by using the Vistec EBPG5000Plus system. After that, 5 nm chromium (Cr) and 25 nm nickel (Ni) are deposited onto the sample with an electron-beam (e-beam) evaporator (Kurt J. Lesker). Then a lift-off process is performed to form a hard Cr/Ni mask for the following dry etching step. The plasma-enhanced deep reactive ion etching (DRIE) is then performed using SF_6/CHF_3 gases (Oxford PlasmaPro 100), resulting an etching depth of 1.5 μm with vertical walls. The Cr/Ni hard mask residual is then removed with a Cr and Ni etching solvent. After cleaning the sample, the pattern is deposited with a 100 nm silver layer with e-beam evaporation (Kurt J. Lesker), configured to ensure line-of-sight deposition. This results in two planar silver layers without covering the side walls of resonators. Figure 7.4(b) shows the scanning electron micrograph of the fabricated sample.

The reflectance of the fabricated sample is measured with Fourier transform infrared microscopy (FTIR, Bruker VERTEX 70 and Hyperion 2000 microscope). The wavelength range of the measurement is from 600 to 3000 cm^{-1} (3.33 to 16.67 μm) with a spectral resolution of 8 cm^{-1}. The reflective 36×, NA 0.5 objective provides a hollow light cone, thereby limiting the incidence angle range from 15° to 30°. The incident excitation is unpolarised and a clean, flat and empty area on the sample (silver surface) is used as the background reference. Figure 7.6(a) presents the measured power absorptivity (or emissivity) spectrum, calculated via $A = 1 - R$, where A denotes the absorptivity and R is the measured reflectance of the radiative cooling sample. It is observed in Fig. 7.6(a)

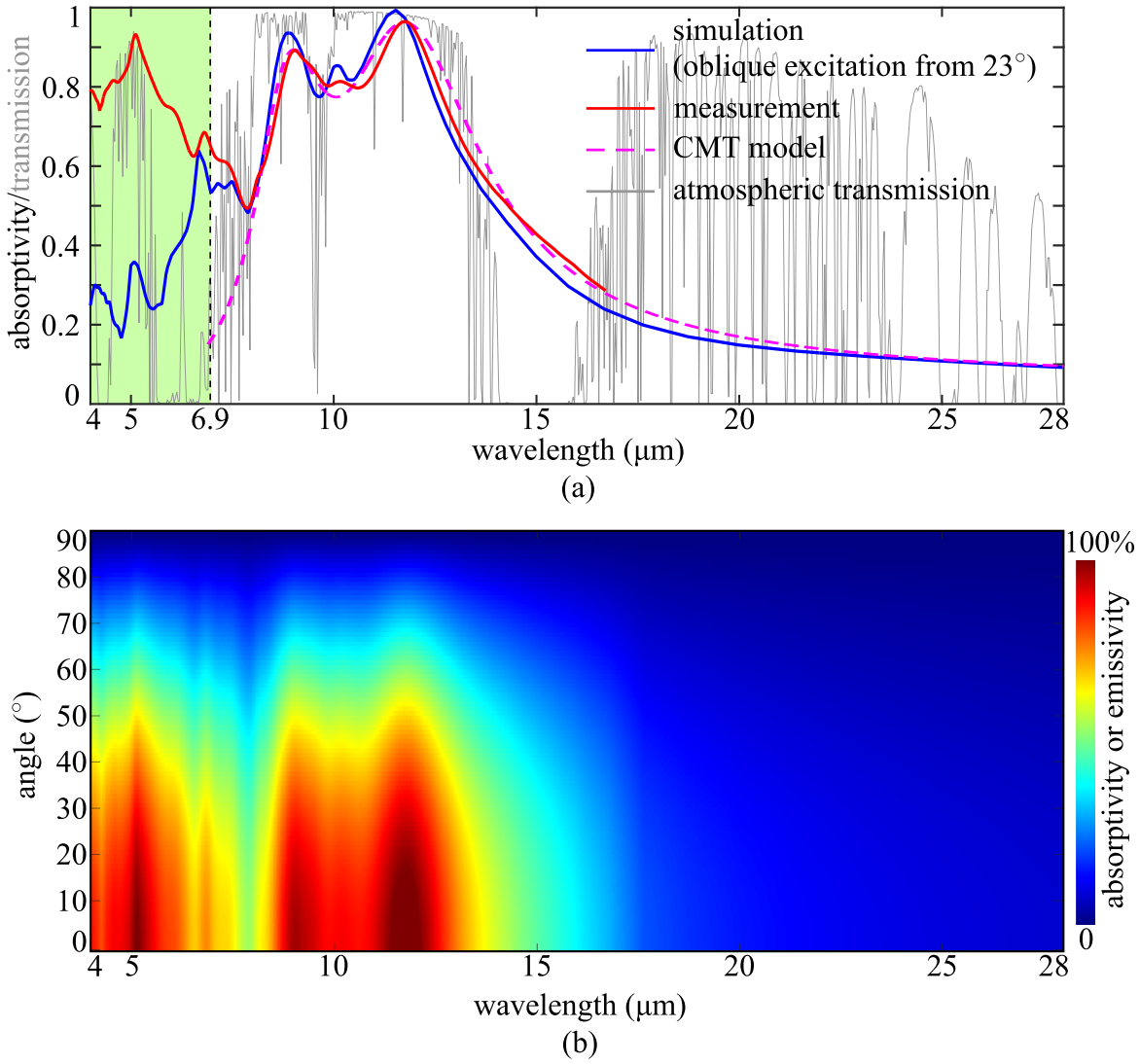

Figure 7.6. Measured power absorptivity of the fabricated radiative cooling sample. (a) Measured absorptivity of the fabricated radiative cooling sample. The magenta dashed line is the coupled mode theory (CMT) model ($N = 2$) fitted to the measured result according to Eq. 5.1. For the peak at around 9 μm, $Q_{a1} = 18.5$ and $Q_{r1} = 5.4$. For the peak at 11.8 μm, $Q_{a2} = 9.4$ and $Q_{r2} = 3.9$. The light-green shading from 4 to 6.9 μm denotes the wavelength range where measurement inaccuracy is caused by the diffracted power loss. (b) The extrapolated angular-dependent absorptivity calculated by fitting the measured result into the Lambertian cosine profile (Smith 1966).

that the measured absorptivity matches reasonably well with the simulated result at wavelength above 7 μm. However, towards the shorter wavelength shaded by light green, although the measured peak is at the same wavelength as the simulated peak, the measured absorptivity is significantly higher. This high absorption is most likely caused by power loss via diffraction as well as excitations of asymmetric modes. As

the designed metasurface has a periodicity of 6.9 μm, higher-order diffractions can occur in the shaded wavelength range. The reflection measurement only captures the reflected power in the angle between 15° to 30°, which leads to a certain amount of diffracted power not being collected. Therefore, the measured absorption in the shaded range is artificially increased. For wavelength longer than 16.7 μm, which is outside the measurement range, the absorption spectrum is extrapolated as the magenta dashed line by using a coupled-mode-theory model fitting to the measurement result according to Eq. 5.1. The error in the following cooling efficiency analysis with this extrapolated absorptivity is expected to be insignificant.

For further cooling efficiency analysis, it is also necessary to know the angular-dependent absorptivity. As the measurement can only be performed from 15° to 30°, the full angle absorptivity has to be extrapolated with a reasonable model. In this case, a Lambertian cosine scattering surface (Smith 1966) is assumed for modelling the full angle absorptivity from 0° to 90°. The corresponding result is shown in Fig. 7.6(b). Comparing to the simulated angular-dependent absorptivity in Fig. 7.5(b), the major difference is that the measurement-based result shows a high absorptivity in the short wavelength range below 7 μm, which has been explained with the diffracted power loss. For the measurement-based angular absorptivity in the major IR atmospheric window, the absorption angle is wider for the peak at 8.8 μm, but narrower for the peak at 11.3 μm, than the corresponding simulation results. Therefore, the cooling performance of the fabricated sample is expected to be similar to that of the simulated design.

7.4.4 Cooling efficiency analysis

Based on the discussions and results presented in the previous sections, the cooling efficiency of the proposed metasurface can be analysed. Both the cooling performances based on the simulation and the measurement are calculated in this section. In the analysis, IR-transparent heat insulators and solar reflectors (wavelength up to 4 μm) are assumed to be integrated into the cooling device. Accordingly, the value of q in Eq. 7.5 is assumed to be within 6.9 $W/m^2/K$ (Hossain and Gu 2016) and the solar input power is taken as 27 W/m^2. For P_r and P_a calculations, a wavelength ranging from 4 to 28 μm is considered. For wavelengths shorter than 4 μm, the blackbody radiation approaches zero, and the integrated solar reflector results in a minimum heat exchange. Therefore, the calculation error from neglecting shorter wavelengths is negligible. For wavelengths longer than 28 μm, the atmosphere transmission data is not available from

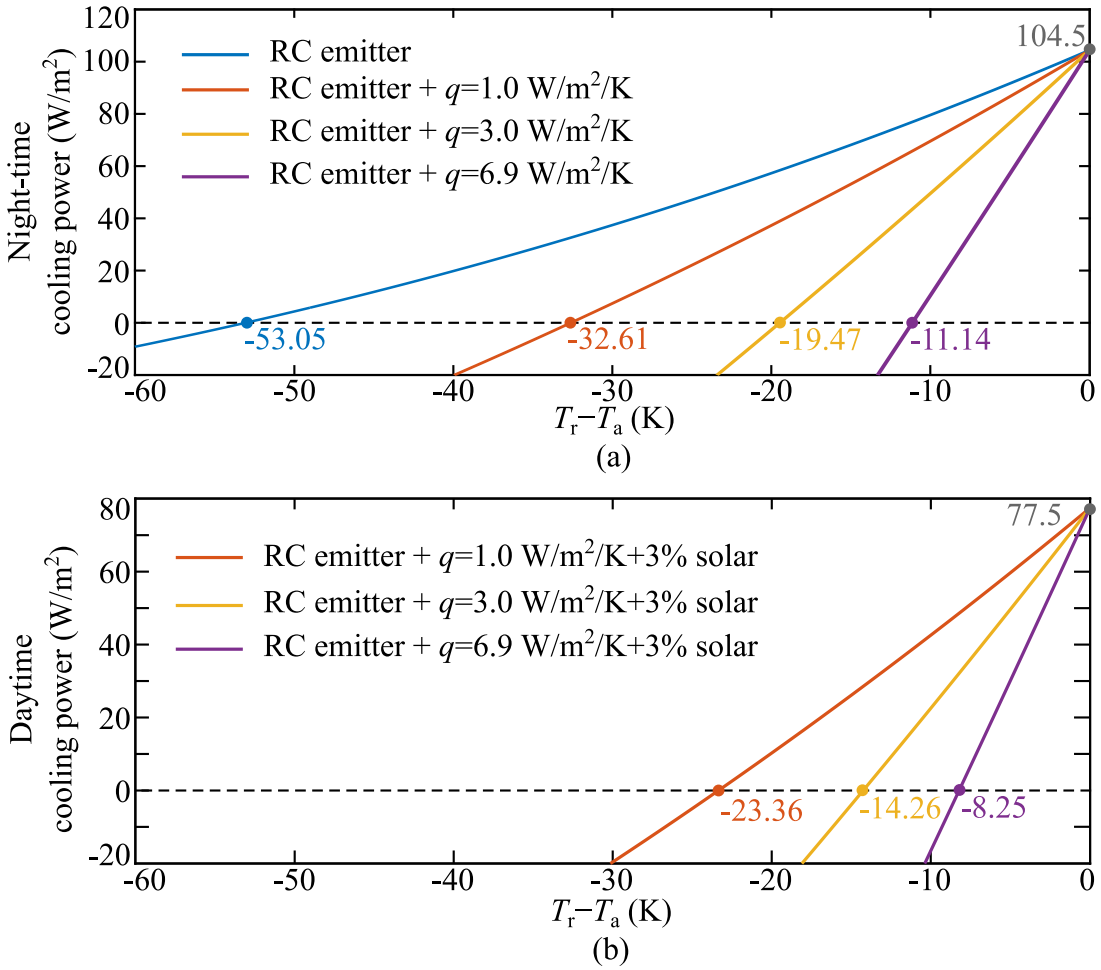

Figure 7.7. Calculated cooling power at night-time and daytime based on the simulation. q represents the combined heat exchange coefficient. Values of 1.0, 3.0, and 6.9 for q is used in calculation. For daytime calculation, a 3% solar power absorption is considered in the calculation. T_a is considered as room temperature of 300 K.

accessible databases. Considering that the blackbody radiation at room temperature is also very limited, and the simulated absorption for the cooling metasurface is less than 8% at wavelength beyond 28 μm, the calculation error from ignoring longer wavelengths can also be neglected. Figure 7.7(a,b) presents the calculated cooling power at night-time and daytime respectively based on the simulated results. T_a is taken as 300 K in both cases. As shown in Fig. 7.7(a), the blue line shows the ideal cooling condition where no non-radiative heat exchange occurs. In this case, a maximum cooling power of 104.5 W/m^2 can be achieved. From the curves, it can be seen that due to the efficient heat emission, the metasurface temperature T_r decreases. This in turn leads to a weaker blackbody radiation from the radiative cooler. Thereby, the cooling power reduces as T_r decreases, and finally reaches zero, namely the thermal

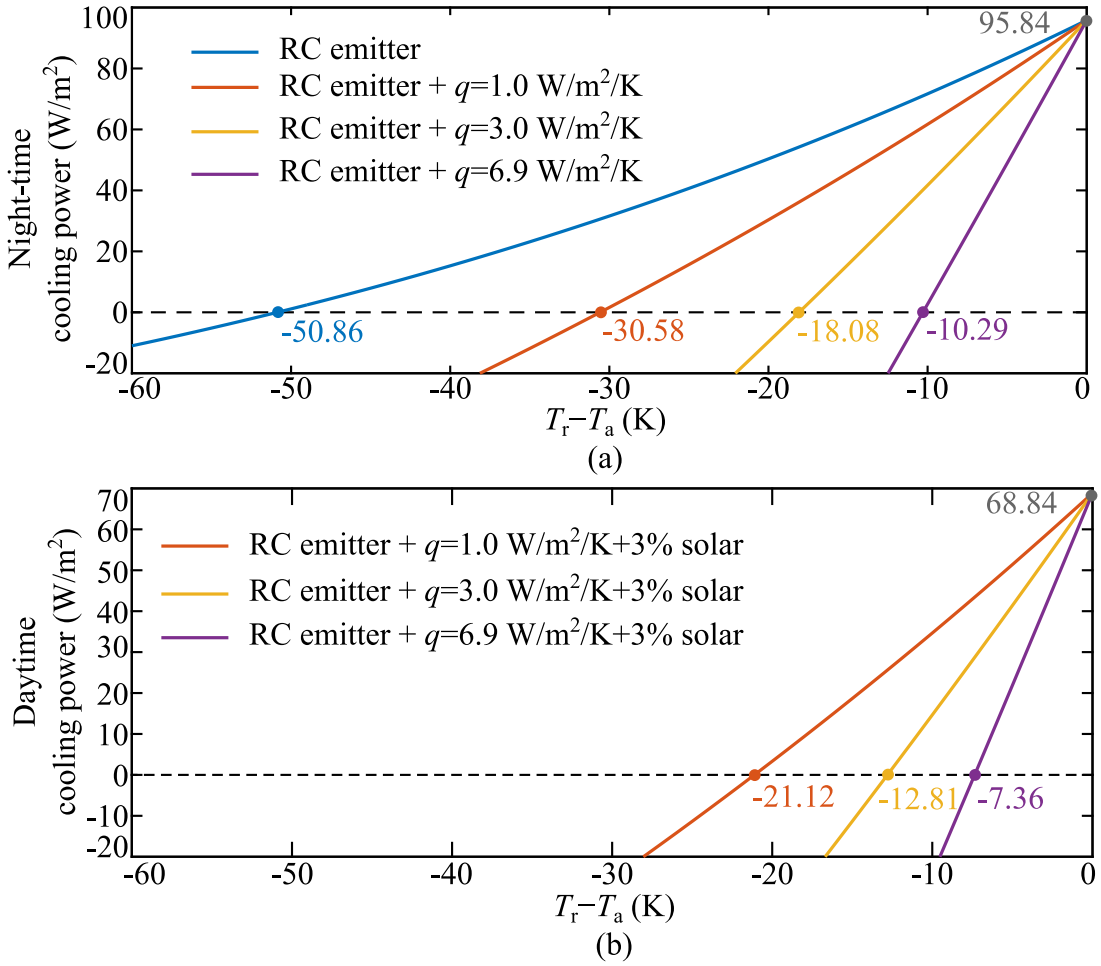

Figure 7.8. Calculated cooling power at night-time and daytime based on the measurement. q represents the combined heat exchange coefficient. Values of 1.0, 3.0, and 6.9 for q is used in calculation. For daytime calculation, a 3% solar power absorption is considered in the calculation. T_a is considered as room temperature of 300 K.

equilibrium temperature. For night-time cooling, by considering the maximum non-radiative heat exchange, the cooling metasurface can create a minimum temperature of 11.14 K below the ambient temperature at thermal equilibrium. While for daytime operation, considering all heat exchanges, the minimum temperature difference is 8.25 K at thermal equilibrium. Similar results are also obtained in the cooling power calculation based on the measurement modelled with a Lambertian profile. Figure 7.8(a,b) presents the corresponding calculated cooling power at night-time and daytime respectively. In this case, a maximum net cooling power of 95.84 W/m^2 is achieved. However, considering the measured artificial high absorption at shorter wavelengths, the real cooling power is expected to be higher. For night-time cooling, by considering the maximum non-radiative heat exchange of 6.9 W/m^2/K, the cooling metasurface can

create a minimum temperature decrease of 10.29 K below the ambient temperature at thermal equilibrium. While for daytime operation, considering all heat exchanges, the minimum temperature decrease is 7.36 K at thermal equilibrium.

7.5 Conclusion

This chapter has proposed and validated a type of metasurface made of metal-loaded DRs for selective thermal emission. This metal-loaded DRs can be conveniently created by etching doped silicon wafers before coating them with a thin metallic layer. Two selective thermal emission metasurfaces have been proposed. The first design consists of a uniform array of cylindrical metal-loaded DRs, and has shown a temperature-stable emission peak at around 8 μm from 300 K to 900 K. The second design has its emissivity matched with an atmospheric window. The design has been fabricated for realising the functionality of radiative cooling. Under a practically accepted heat insulation assumption, the cooling efficiency has been analysed based on simulated and measured results. From the simulation-based analysis of the cooling ability, the minimum temperature decrease is 11.14 K and 8.25 K at thermal equilibrium for night-time and daytime operations, respectively. From the corresponding measurement based analysis, the minimum temperature decrease is 10.29 K and 7.36 K at thermal equilibrium for night-time and daytime operations, respectively. The introduced thermal emission metasurface topology has several prominent advantages. From the perspective of fabrication, the proposed structure is simple and the material and fabrication cost is low compared to aforementioned multi-layer metamaterial structures (Rephaeli *et al.* 2013, Hossain and Gu 2016). With deep-UV photolithography or nano-imprint lithography, the structure can be fabricated on a large area at industrial manufacture scale. From application perspective, the design can be easily integrated with silicon photonic platforms and can be applied to renewable energy, thermal emission control, or IR-sensing.

Chapter 8

Summary and Outlook

THIS Chapter concludes the thesis by firstly summarising the major results and findings of each chapter. Then, an outlook for the future research on optical dielectric resonators and dielectric metasurfaces is presented.

8.1 Thesis summary

Optical metasurfaces are widely seen with tangible potential as the first kind of optical metamaterials to be realisable for real-world applications. By integrating low-loss dielectric resonators (DRs) that can support multi-order Mie resonances with optical metasurfaces, the achieved dielectric metasurfaces can operate with higher efficiency than their metallic counterparts. Moreover, a number of functionalities based on the specificities of Mie resonances, especially magnetic resonances, can be realised. The research in this thesis has explored the application of subwavelength DRs to optical metasurfaces for achieving highly-efficient designs with various functionalities. The major outcomes include two parts: the first part is based on theoretical studies of nano-scale DRs at visible light frequencies, while the second part includes three optical dielectric metasurface designs. These achievements are summarised in the following.

8.1.1 Part I: Theoretical studies

In Chapter 3, the resonance properties of nano-scale DRs on a metallic substrate at visible frequencies have been analysed. The analysis mainly revealed that two types of resonance breakdown can occur. The first type of resonance breakdown is commonly seen in DRs with very low permittivities, where incident electromagnetic energy can hardly resonate in the DR structure because of the low contrast at the DR boundary. On the other hand, the second type of resonance breakdown occurs specifically in the optical domain for DRs with high permittivities, when the real part of the permittivity of a DR negatively matches with that of the DR's metal substrate. In this particular case, the surface plasmon polariton (SPP) wavelength is be extremely short at the DR-metal interface, the plasmonic loss is extremely high, and the electric field becomes de-polarised. For permittivities in between these two extremes, DRs can resonate in their horizontal magnetic dipole mode. By varying its size, a DR can be designed to demonstrate different reflected magnitude and a range of 2π phase responses. The analysis was verified with full-wave simulations, validating that DRs with permittivities from low to high values on a silver surface can be excited by normally incident electromagnetic waves at 622 nm. Importantly, the simulation results demonstrated all predicted phenomena, as the permittivity of the DR increased from low to high values, *i.e.* low-permittivity resonance breakdown, efficient horizontal magnetic dipole resonance, higher-order mode resonance, and negatively-matched resonance breakdown.

Furthermore, it was proposed that the negatively matched resonance breakdown can be mitigated by inserting a low-permittivity thin dielectric layer between the DR and its metallic substrate. This study suggested limited choices of the DR permittivity for optimal operations, which is important for designing metallo-dielectric nanostructures at optical frequencies.

Chapter 4 has extended the idea of DR-based SPP coupling and has proposed to use non-uniform arrays of cylindrical DRs for unidirectional SPP launching. Non-uniform arrays of DRs can create SPP phase gradients along metallic surfaces and thus realise SPP unidirectional launching by manipulating SPPs interferences. Such a launcher can reduce plasmonic losses from SPP couplers themselves. The first part of the chapter looked into determining optimal SPP launching conditions to maximise the coupling efficiency from free-space waves into unidirectional propagating SPPs. By comparing the principles of unidirectional SPP launching and diffraction, it was theoretically concluded that optimal SPP launching occurred along the zeroth-order launching lines located in a so-called non-deflection zone, where the first-order diffraction cannot occur. Moreover, this optimal launching condition was further examined with a linear array model for both infinite-size and finite-size arrays scenarios, also including SPP propagation loss. The analysis showed that the optimal SPP launching can only be achieved along the SPP launching lines for both finite-size and infinite-size arrays. However, for finite-size array, the SPP launched power into the opposite direction is not strictly zero, but is approaching zero when array sizes are large. When considering the propagation loss, the analysis showed that the launched power would saturate when arrays are large enough. Finally, the DR-based launcher and the optimal launching condition were verified with simulations by comparing the coupling efficiency of non-uniform arrays in the deflection zone and non-deflection zone. The simulated examples confirmed that the optimised SPP coupling efficiency can be 20% higher in the non-deflection zone than that in the deflection zone. The analysis and simulation also demonstrated conditions for constructing efficient optical reflectarrays and for SPP standing waves.

8.1.2 Part II: Realisation of optical metasurfaces

Chapter 5 has experimentally demonstrated a narrowband plasmonic absorber based on uniform arrays of cylindrical DRs on metallic substrates at 633 nm. The perfect absorption relied on the SPP standing waves excited by the locally resonant nano-scale

DRs. A sample of this design was fabricated with electron beam lithography and the measurement showed maximum 90% absorption at 636 nm. Both simulation and measurement results were analysed with coupled mode theory to model the absorption and radiation losses based on estimated Q-factors. Further studies on the resonator sizes, periodicity, and incident angles in relation to absorption performance were also discussed.

In Chapter 6, a mechanically tunable visible-frequency DR metasurface has been experimentally demonstrated. The metasurface was fabricated by embedding an array of nano-scale TiO_2 DRs into a polydimethylsiloxane (PDMS) elastomer. In an optical simulation, the unstrained DRs were excited to resonate as electric dipoles at 591 nm under normally incident plane-wave excitations. The deformation of the metasurface under a uniaxial strain was modelled by using finite-element mechanical simulations, which demonstrated that the deformation of the PDMS encapsulation would not affect the shape of the DRs. Based on the simulated unit-cell deformation data, the optical response of the metasurface under an external strain was modelled with optical simulation. When the uniaxial external strain to the PDMS encapsulation is along the electric dipole direction, mainly the near-field longitudinal interactions among DRs is altered, thereby causing a blue-shift of the resonance peak. In contrast, when applying a uniaxial external strain to the PDMS encapsulation perpendicular to the electric dipole direction, the near-field transverse interactions among DRs is mainly altered, resulting in a redshift of the resonance peak. These resonance shifts were confirmed with measurements. With a 6% deformation of the PDMS encapsulation along or perpendicular to the electric dipole direction, the measured resonance peak blue-shifted 0.96% and redshifted 5.08% respectively. These results were further rigorously analysed with a Lagrangian model which confirmed that the alteration of near-field interactions amongst DRs led to the resonance shifts and the traverse coupling of E-fields played the dominant role. Such a design can be used as reconfiguration optical devices in integrated optics, and has potentials for commercial application in smart contact lenses for filtering out unwanted frequencies.

In Chapter 7, a novel concept of metasurfaces made of metal-loaded DRs has been proposed for selective thermal emission. The metasurfaces were realised by etching a depth of 1.5 μm on a phosphorous-doped silicon wafer before coating the structure with a 100 nm silver layer. Two realisations of such selective thermal emission metasurfaces have been presented in Chapter 7. The first metasurface, consisting of a uniform array

of cylindrical metal-loaded DRs, demonstrated a temperature-stable thermal emission peak at around 8 μm from 300 K to 900 K. The second metal-loaded DR metasurface, made by two orthogonally oriented arrays of identical rectangular DRs, was designed to realise the functionality of radiation cooling. A broadband power absorption (or emission) was demonstrated from 8 to 13 μm, which matches the main atmospheric window in the mid-infrared range. The cooling efficiency analysis showed a maximum net cooling power of 95.84 W/m^2 at room temperature based on the Lambertian-modelled measured emissivity, as well as a minimum 10.29 K and 7.36 K temperature decrease at thermal equilibrium for night-time and daytime operations respectively. The proposed metasurfaces have the following advantages: (i) From the perspective of fabrication, the proposed structure is simple and the material and incurred costs are low compared to many other metamaterial structures. With deep-UV photolithography or nano-imprint lithography, the structure can potentially be fabricated over a large area at industrial manufacture scale. (ii) From applications' perspective, the design can be easily integrated with silicon photonic platforms and can be applied to renewable energy, thermal emission control, and infrared-sensing.

8.2 Further work and outlook

8.2.1 Further work

Several important further studies based on the research in this thesis can be carried out in the future, as detailed in the following:

- Uniform arrays of nano-scale DRs on metallic substrates can be excited to resonate as horizontal magnetic dipoles and demonstrate a range of 2π reflection phase responses with varying DR size. However, for non-uniform arrays, the inter-couplings among DRs add asymmetrical excitations to the DRs, resulting in possible excitation of different resonance modes and unpredictable phase responses. As many metasurfaces are based on non-uniform arrays, the impact from inter-resonator couplings is worth of further investigation. Based on such understanding, methods to reduce coupling effects also require further research. A potential solution is to introduce self-coupled resonators. For example, if a unit-cell consists of two resonators (or resonances) that are strongly coupled to each other, then the impacts from inter-cell couplings can be significant reduced.

This technique has been adopted in an achromatic flat lens design by Khorasaninejad *et al.* (2015). By using this technique, however, preventing mode hybridisations in the operation bandwidth in a unit-cell becomes critical.

- DR-based unidirectional SPP launchers need to be fabricated and experimentally demonstrated. The main reason to the absent experimental demonstration of this design was a limited access to fabrication facilities and lack of dedicated optical characterisation systems for this particular geometry. In the near future, several prototype designs are planned, and contacts were made for possible measurements with collaborators. Unfortunately, the timeline of this endeavour is beyond the time of my PhD candidature.
- The type of single-peak thermal emitters proposed in Section 7.2 is worthy of being fabricated and measured. New designs may use other semiconductor and metal materials, and operate at different wavelengths with proper bandwidths. Temperature-dependent absorption or emission measurements should be carried out to fully verify the concept.

8.2.2 Outlook

In the past few years, significant research efforts have been invested in optical dielectric metasurfaces in areas such as flat optics (Kamali *et al.* 2016a, Khorasaninejad *et al.* 2016), active and tunable devices (Sautter *et al.* 2015, Gutruf *et al.* 2016), and sub-diffraction sensors based on field enhancement (Albella *et al.* 2014). Many challenges remains unsolved on these topics, while new research areas for nano-scale DRs can be explored. This section describes my views on some of the research challenges and future prospects of dielectric metasurfaces.

The first area of interest is on flat optics. Although hundreds of publications have focused on this topic, there are still some critical issues requiring further investigations. The initial idea to use nano-scale DRs in flat optical devices is to reduce the significant Ohmic loss in metallic resonators, and thus achieve high efficiencies. However, due to the nature of Mie resonances of DRs, dispersionless and achromatic designs such as achromatic flat lenses, are difficult to achieve. A technique of dispersion compensation (Khorasaninejad *et al.* 2015) has been proposed, which however, only works at a few discrete wavelengths. Another research challenge in this area is to reduce non-Ohmic power loss originated from scattering and diffraction, which have been seen as the

major loss from dielectric metasurfaces measurements. From a broad view, flat optical devices have shown strong potential for the next generation photonic communication systems. To push towards this aim, research on tunable and active flat optical devices with the ability to integrate with photonic platforms is worthy of further investigation. Low-loss flexible materials (Gutruf *et al.* 2016), phase-change materials (Sautter *et al.* 2015, Krishnamoorthy *et al.* 2014), and semiconductors (Liu *et al.* 2016) can be further studied.

Another research topic that I believe worthy of further efforts is on nonlinear dielectric metasurfaces. Plasmonic nanostructures have been extensively investigated for enhancing nonlinear optical process (Kauranen and Zayats 2012). Subwavelength DRs that are intrinsically free from Ohmic loss can promise even higher efficiencies for nonlinear optics. Several dielectric metasurfaces for third harmonic generations (Shcherbakov *et al.* 2014, Shcherbakov *et al.* 2015a) or switching (Shcherbakov *et al.* 2015b) have been preliminarily demonstrated. More investigations can focus on designs that achieve higher conversion efficiency and on exploring dielectric materials with large higher-order susceptibilities. Furthermore, these nonlinear dielectric metasurfaces can be integrated with emitters (Bouchet *et al.* 2016) or waveguides, which can lead to promising applications in integrated photonics and optoelectronics. In addition, dielectric metasurfaces can be explored when combining with 2D materials that have large nonlinear susceptibilities.

I also believe more research can be carried out on hybrid metal-dielectric optical metasurfaces (Guo *et al.* 2016) at optical frequencies. Plasmonic resonators have the advantages of strong field enhancement (Novotny and Van Hulst 2011), which is more pronounced than that in nano-scale DRs. This makes them more suitable for sensing and spectroscopy than optical DRs. However, for fluorescence and enhancement of emission, the non-radiative plasmonic loss can significantly reduce the radiation lifetime (Albella *et al.* 2014), as described by the Purcell factor (Purcell 1946). The purpose of using the hybrid metal-dielectric structure is to balance the advantages of both plasmonic and dielectric materials. For instance, in a hybrid metal-dielectric metasurface, the strong resonant fields should be mainly constrained in the dielectric part (Zou *et al.* 2013), while the areas requiring strong field enhancement can be covered with metals. The hybrid metals and dielectric materials can be further explored in many research topics such as nanoantennas, optical switching, and nano-emitters.

Many DR metasurfaces are demonstrated to operate at near-infrared frequencies based on silicon. To further push the research of DR metasurfaces forward in the visible frequency range, low-loss and high refractive-index dielectric materials at visible frequencies are of critical importance. However, one challenge is that the current visible-light "material library" is small. The designs in this thesis are mainly based on TiO_2. Besides that, only a few other dielectric materials have been used in reported visible DR metasurfaces. To expand the "material library", one type of materials worth further exploration includes semiconductors with bandgaps above visible frequencies, such as gallium phosphide. Similarly, nanofabrication technology is also critical for visible light metasurfaces. To achieve complicated functionalities and push nanostructure devices towards real-world applications, nanofabrication technologies for larger sample size, higher geometrical accuracy, and larger shape aspect-ratio are desired, while lowering the manufacture costs. Potentially, deep-UV photolithography and nano-imprint lithography (NIL) can be adopted for large-sample at low-cost, as reported in a few attempts (Spinelli *et al.* 2012, Bottein *et al.* 2017). Atomic layer deposition (Khorasaninejad *et al.* 2016) and multi-cycle etching (Liu *et al.* 2013) have also been demonstrated for high aspect-ratio and conformal visible frequency DR metasurfaces.

8.3 Concluding statement

Nano-scale DRs with the advantage of low optical loss and the ability to support multi-order optical Mie resonances have shown remarkable ability to efficiently manipulate light. In this thesis, I have presented both theoretical studies and realisations of nano-scale DRs with high-efficiency, tunability and various functionalities. In addition, related literature reviews of current research topics dedicated to dielectric metasurface have been provided in each chapter. The recent years have seen significant research interests and efforts on artificial nanostructures, enabling more precise control to and wider range of applications of light-matter interactions at nano-scale. With further advances in nanofabrication technology, material science, and fundamental research, nanophotonic research will attract further interests and efforts. Meanwhile, pushing nanophotonic research closer to real-world applications will improve our live quality and benefit our society.

Appendix A

Miscellaneous Relations

- The absorption and refraction of electromagnetic waves propagating in medium can be described by the complex refractive index:

$$\tilde{n} = n + i\kappa, \tag{A.1}$$

where n is the normal refractive index and κ is the extinction coefficient. The frequency-dependent $\tilde{n}(\omega)$ and permittivity $\epsilon(\omega) = \epsilon_1(\omega) + i\epsilon_2(\omega)$ are related as:

$$\tilde{n}(\omega) = \epsilon^2(\omega). \tag{A.2}$$

The real and imaginary parts of $\epsilon(\omega)$ can be expressed in terms of $\tilde{n}(\omega)$ as:

$$\epsilon_1(\omega) = n^2(\omega) - \kappa^2(\omega), \tag{A.3}$$

$$\epsilon_2(\omega) = 2n(\omega)\kappa(\omega) \tag{A.4}$$

On the contrary, the real and imaginary parts of $\tilde{n}(\omega)$ can be expressed in terms of $\epsilon(\omega)$ as:

$$n(\omega) = \frac{1}{\sqrt{2}}\sqrt{\epsilon_1(\omega) + \sqrt{\epsilon_1^2(\omega) + i\epsilon_2^2(\omega)}}, \tag{A.5}$$

$$\kappa(\omega) = \frac{1}{\sqrt{2}}\sqrt{-\epsilon_1(\omega) + \sqrt{\epsilon_1^2(\omega) + i\epsilon_2^2(\omega)}}. \tag{A.6}$$

- The absorption coefficient α and the extinction coefficient κ are used interchangeably and are related as:

$$\alpha = \frac{2\kappa\omega}{c}, \tag{A.7}$$

where c is light velocity in vacuum.

- From Eq. A.7, the skin depth δ can be calculated as:

$$\delta = \frac{2}{\alpha} = \frac{c}{\kappa\omega}. \tag{A.8}$$

- The conductivity $\sigma(\omega)$ and permittivity $\epsilon(\omega)$ are related as:

$$\epsilon(\omega) = 1 + \frac{i\sigma(\omega)}{\epsilon_0 \omega}, \tag{A.9}$$

  where ϵ_0 is the vacuum permittivity.

- The wave impedance of electromagnetic waves in medium are calculated as:

$$Z = \sqrt{\frac{j\omega\mu}{\sigma + j\omega\epsilon'}}, \tag{A.10}$$

  where μ is the magnetic permeability.

Appendix B

Characterisation of the Relevant Materials

B.1 Isotropic permittivity of TiO_2

The measured isotropic permittivity of TiO_2 (anatase) used in the mechanically tunable dielectric resonator metasurface in Chapter 6 is presented. TiO_2 actually has uniaxial anisotropic permittivity. However, as the electric dipole resonance mode is excited in DRs of this design, the *E*-field mainly responds to the planar-axis permittivity of TiO_2. Therefore, errors from using isotropic data are not expected to be significant. The measurement is performed with F40-EXR by using unpolarised normally incident beam on a flat 100 nm TiO_2 thin film deposited on a intrinsic silicon wafer. Figure B.1 presents the measured isotropic permittivity, which has little variation for at the wavelength longer than 600 nm and almost no optical loss.

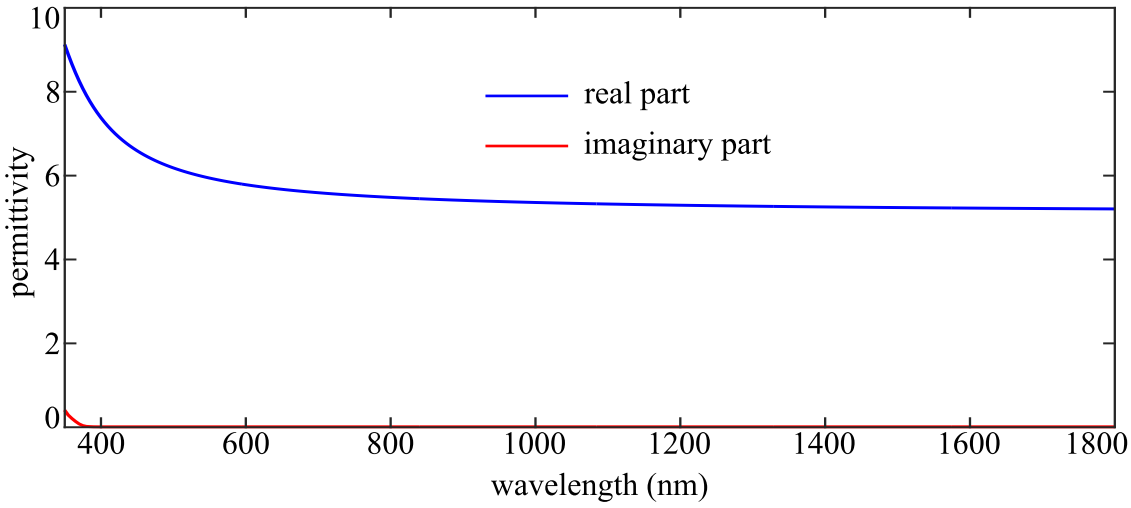

Figure B.1. Measured isotropic permittivity of TiO_2 (anatase).

B.2 Ellipsometry characterisation

The permittivity of phosphorus-doped silicon wafers adopted in Chapter 7 was characterised with an infrared ellipsometer (J.A. Woollam, IR-VASE MARK II). The principle of ellipsometry is to measure the complex ratio betwen the TM-polarised and the TE-polarised complex reflectivities of the test sample. The complex ratio can be expressed as:

$$\rho = \frac{R_{\mathrm{TM}}}{R_{\mathrm{TE}}} = \tan\psi\, e^{i\Delta}, \tag{B.1}$$

where R_{TM} and R_{TE} denotes the TM-polarised and the TE-polarised complex reflectivities respectively. The tangent of ψ denotes the magnitude ratio while Δ denotes the phase difference. A Drude-based dielectric function is adopted to fit the measured data by calculating the reflectivity ratio according to Fresnel's equation (Jackson 1999). The measured and fitted results are presented as the follow:

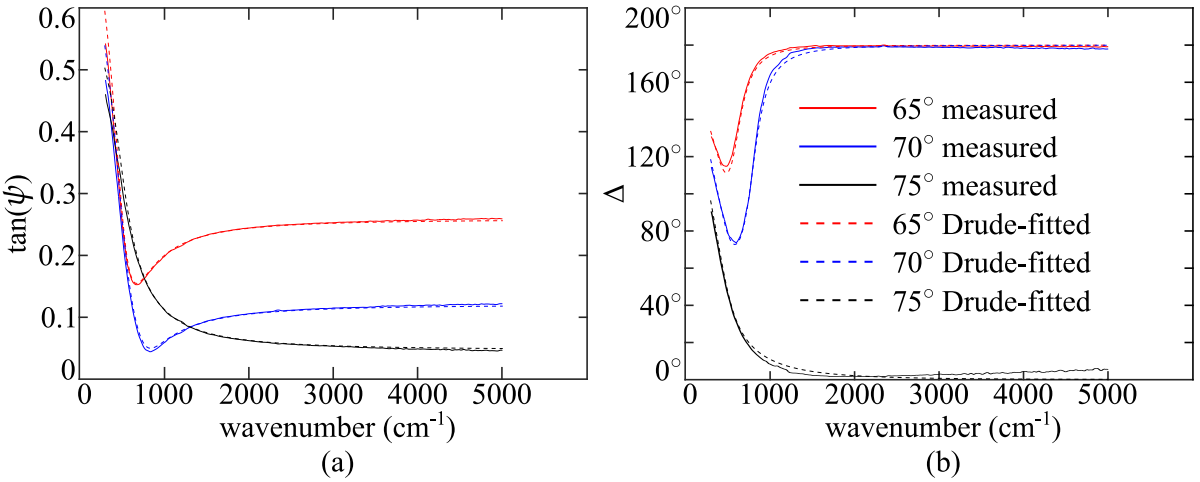

Figure B.2. Ellipsometry measurement results. (a) The magnitude ratio between the p-polarised and the s-polarised reflectivities. The value of $\tan(\psi)$ instead of ψ itself is plotted. (b) The phase difference between the p-polarised and the s-polarised reflectivities.

Bibliography

AIETA-F., GENEVET-P., KATS-M. A., YU-N., BLANCHARD-R., GABURRO-Z., AND CAPASSO-F. (2012a). Aberration-free ultrathin flat lenses and axicons at telecom wavelengths based on plasmonic metasurfaces, *Nano Letters*, **12**(9), pp. 4932–4936.

AIETA-F., GENEVET-P., YU-N., KATS-M. A., GABURRO-Z., AND CAPASSO-F. (2012b). Out-of-plane reflection and refraction of light by anisotropic optical antenna metasurfaces with phase discontinuities, *Nano Letters*, **12**(3), pp. 1702–1706.

AKSU-S., HUANG-M., ARTAR-A., YANIK-A. A., SELVARASAH-S., DOKMECI-M. R., AND ALTUG-H. (2011). Flexible plasmonics on unconventional and nonplanar substrates, *Advanced Materials*, **23**(38), pp. 4422–4430.

ALBELLA-P., ALCARAZ DE LA OSA-R., MORENO-F., AND MAIER-S. A. (2014). Electric and magnetic field enhancement with ultralow heat radiation dielectric nanoantennas: considerations for surface-enhanced spectroscopies, *ACS Photonics*, **1**(6), pp. 524–529.

ALMPANIS-G., FUMEAUX-C., AND VAHLDIECK-R. (2008). The trapezoidal dielectric resonator antenna, *IEEE Transactions on Antennas and Propagation*, **56**(9), pp. 2810–2816.

ARGYROPOULOS-C., LE-K. Q., MATTIUCCI-N., DAGUANNO-G., AND ALU-A. (2013). Broadband absorbers and selective emitters based on plasmonic brewster metasurfaces, *Physical Review B*, **87**(20), art. no. 205112.

ASADCHY-V., ALBOOYEH-M., AND TRETYAKOV-S. (2016). Optical metamirror: all-dielectric frequency-selective mirror with fully controllable reflection phase, *Journal of Optical Society of America B*, **33**(2), pp. A16–A20.

AYDIN-K., FERRY-V. E., BRIGGS-R. M., AND ATWATER-H. A. (2011). Broadband polarization-independent resonant light absorption using ultrathin plasmonic super absorbers, *Nature Communications*, **2**, art. no. 517.

BACCARANI-G., AND OSTOJA-P. (1975). Electron mobility empirically related to the phosphorus concentration in silicon, *Solid-State Electronics*, **18**(6), pp. 579–580.

BALANIS-C. A. (2016). *Antenna Theory: Analysis and Design*, John Wiley & Sons.

BARON-A., DEVAUX-E., RODIER-J.-C., HUGONIN-J.-P., ROUSSEAU-E., GENET-C., EBBESEN-T. W., AND LALANNE-P. (2011). Compact antenna for efficient and unidirectional launching and decoupling of surface plasmons, *Nano Letters*, **11**(10), pp. 4207–4212.

BASU-S., CHEN-Y.-B., AND ZHANG-Z. (2007). Microscale radiation in thermophotovoltaic devices–a review, *International Journal of Energy Research*, **31**(6-7), pp. 689–716.

BAUCH-M., AND DOSTALEK-J. (2013). Collective localized surface plasmons for high performance fluorescence biosensing, *Optics Express*, **21**(17), pp. 20470–20483.

BENSON-O. (2011). Assembly of hybrid photonic architectures from nanophotonic constituents, *Nature*, **480**(7376), pp. 193–199.

BENZ-A., MONTAÑO-I., KLEM-J. F., AND BRENER-I. (2013). Tunable metamaterials based on voltage controlled strong coupling, *Applied Physics Letters*, **103**(26), art. no. 263116.

BERINI-P. (2000). Plasmon-polariton waves guided by thin lossy metal films of finite width: Bound modes of symmetric structures, *Physical Review B*, **61**(15), art. no. 10484.

BERINI-P. (2001). Plasmon-polariton waves guided by thin lossy metal films of finite width: Bound modes of asymmetric structures, *Physical Review B*, **63**(12), art. no. 125417.

BERMEL-P., GHEBREBRHAN-M., CHAN-W., YENG-Y. X., ARAGHCHINI-M., HAMAM-R., MARTON-C. H., JENSEN-K. F., SOLJAČIĆ-M., JOANNOPOULOS-J. D., JOHNSON-S. G., AND IVAN-C. (2010). Design and global optimization of high-efficiency thermophotovoltaic systems, *Optics Express*, **18**(103), pp. A314–A334.

BIAGIONI-P., HUANG-J.-S., AND HECHT-B. (2012). Nanoantennas for visible and infrared radiation, *Reports on Progress in Physics*, **75**(2), art. no. 024402.

BITZER-A., WALLAUER-J., MERBOLD-H., HELM-H., FEURER-T., AND WALTHER-M. (2009). Lattice modes mediate radiative coupling in metamaterial arrays, *Optics Express*, **17**(24), pp. 22108–22113.

BLIOKH-K. Y., BLIOKH-Y. P., FREILIKHER-V., SAVELEV-S., AND NORI-F. (2008). Colloquium: Unusual resonators: Plasmonics, metamaterials, and random media, *Reviews of Modern Physics*, **80**(4), art. no. 1201.

BOARDMAN-A. D., GRIMALSKY-V. V., KIVSHAR-Y. S., KOSHEVAYA-S. V., LAPINE-M., LITCHINITSER-N. M., MALNEV-V. N., NOGINOV-M., RAPOPORT-Y. G., AND SHALAEV-V. M. (2011). Active and tunable metamaterials, *Laser & Photonics Reviews*, **5**(2), pp. 287–307.

BOHREN-C. F., AND HUFFMAN-D. R. (2008). *Absorption and Scattering of Light by Small Particles*, John Wiley & Sons.

BOTTEIN-T., WOOD-T., DAVID-T., CLAUDE-J. B., FAVRE-L., BERBÉZIER-I., RONDA-A., ABBARCHI-M., AND GROSSO-D. (2017). "Black" titania coatings composed of sol-gel imprinted Mie resonators arrays, *Advanced Functional Materials*, **22**(2), art. no. 1604924.

BOUCHET-D., MIVELLE-M., PROUST-J., GALLAS-B., OZEROV-I., GARCIA-PARAJO-M. F., GULINATTI-A., RECH-I., DE WILDE-Y., BONOD-N., KRACHMALNICOFF-V., AND BIDAULT-S. (2016). Enhancement and inhibition of spontaneous photon emission by resonant silicon nanoantennas, *arXiv preprint arXiv:1605.02913*.

BOWDEN-N., BRITTAIN-S., EVANS-A. G., HUTCHINSON-J. W., AND WHITESIDES-G. M. (1998). Spontaneous formation of ordered structures in thin films of metals supported on an elastomeric polymer, *Nature*, **393**(6681), pp. 146–149.

CAI-W., AND SHALAEV-V. M. (2010). *Optical Metamaterials: Fundamentals and Applications*, Vol. 10, Springer.

CAI-W., CHETTIAR-U. K., KILDISHEV-A. V., AND SHALAEV-V. M. (2007a). Optical cloaking with metamaterials, *Nature Photonics*, **1**(4), pp. 224–227.

CAI-W., CHETTIAR-U. K., YUAN-H.-K., DE SILVA-V. C., KILDISHEV-A. V., DRACHEV-V. P., AND SHALAEV-V. M. (2007b). Metamagnetics with rainbow colors, *Optics Express*, **15**(6), pp. 3333–3341.

CARDONA-M., AND PETER-Y. Y. (2005). *Fundamentals of Semiconductors*, Springer.

CELANOVIC-I., JOVANOVIC-N., AND KASSAKIAN-J. (2008). Two-dimensional tungsten photonic crystals as selective thermal emitters, *Applied Physics Letters*, **92**(19), art. no. 193101.

CHAN-D. L., CELANOVIC-I., JOANNOPOULOS-J., AND SOLJAČIĆ-M. (2006). Emulating one-dimensional resonant Q-matching behavior in a two-dimensional system via Fano resonances, *Physical Review A*, **74**(6), art. no. 064901.

CHAPMAN-P., TUFTE-O., ZOOK-J. D., AND LONG-D. (1963). Electrical properties of heavily doped silicon, *Journal of Applied Physics*, **34**(11), pp. 3291–3295.

CHEN-J., LI-Z., YUE-S., AND GONG-Q. (2010). Efficient unidirectional generation of surface plasmon polaritons with asymmetric single-nanoslit, *Applied Physics Letters*, **97**(4), art. no. 041113.

CHEN-Z., ZHU-L., RAMAN-A., AND FAN-S. (2016). Radiative cooling to deep sub-freezing temperatures through a 24-h day–night cycle, *Nature Communications*, **7**, art. no. 13729.

CHU-L. C., GUHA-D., AND ANTAR-Y. M. (2009). Conformal strip-fed shaped cylindrical dielectric resonator: Improved design of a wideband wireless antenna, *IEEE Antennas and Wireless Propagation Letters*, (8), pp. 482–485.

COSTANTINI-D., LEFEBVRE-A., COUTROT-A.-L., MOLDOVAN-DOYEN-I., HUGONIN-J.-P., BOUTAMI-S., MARQUIER-F., BENISTY-H., AND GREFFET-J.-J. (2015). Plasmonic metasurface for directional and frequency-selective thermal emission, *Physical Review Applied*, **4**(1), art. no. 014023.

CUI-Y., HE-Y., JIN-Y., DING-F., YANG-L., YE-Y., ZHONG-S., LIN-Y., AND HE-S. (2014). Plasmonic and metamaterial structures as electromagnetic absorbers, *Laser & Photonics Reviews*, **8**(4), pp. 495–520.

DECKER-M., STAUDE-I., FALKNER-M., DOMINGUEZ-J., NESHEV-D. N., BRENER-I., PERTSCH-T., AND KIVSHAR-Y. S. (2015). High-efficiency dielectric huygens surfaces, *Advanced Optical Materials*, **3**(6), pp. 813–820.

DEVAUX-E., EBBESEN-T. W., WEEBER-J.-C., AND DEREUX-A. (2003). Launching and decoupling surface plasmons via micro-gratings, *Applied Physics Letters*, **83**(24), pp. 4936–4938.

DITLBACHER-H., HOHENAU-A., WAGNER-D., KREIBIG-U., ROGERS-M., HOFER-F., AUSSENEGG-F. R., AND KRENN-J. R. (2005). Silver nanowires as surface plasmon resonators, *Physical Review Letters*, **95**(25), art. no. 257403.

DITLBACHER-H., KRENN-J., SCHIDER-G., LEITNER-A., AND AUSSENEGG-F. (2002). Two-dimensional optics with surface plasmon polaritons, *Applied Physics Letters*, **81**(10), pp. 1762–1764.

DRISCOLL-T., PALIT-S., QAZILBASH-M. M., BREHM-M., KEILMANN-F., CHAE-B.-G., YUN-S.-J., KIM-H.-T., CHO-S., JOKERST-N. M., SMITH-D. R., AND BASOV-D. N. (2008). Dynamic tuning of an infrared hybrid-metamaterial resonance using vanadium dioxide, *Applied Physics Letters*, **93**(2), art. no. 024101.

DRUDE-P. (1900). Zur elektronentheorie der metalle, *Annalen der Physik*, **306**(3), pp. 566–613.

ENOCH-S., AND BONOD-N. (2012). *Plasmonics: From Basics to Advanced Topics*, Vol. 167, Springer.

EVLYUKHIN-A. B., NOVIKOV-S. M., ZYWIETZ-U., ERIKSEN-R. L., REINHARDT-C., BOZHEVOLNYI-S. I., AND CHICHKOV-B. N. (2012). Demonstration of magnetic dipole resonances of dielectric nanospheres in the visible region, *Nano Letters*, **12**(7), pp. 3749–3755.

FANG-Z., ZHEN-Y.-R., FAN-L., ZHU-X., AND NORDLANDER-P. (2012). Tunable wide-angle plasmonic perfect absorber at visible frequencies, *Physical Review B*, **85**(24), art. no. 245401.

FEYNMAN-R. P. (1960). There's plenty of room at the bottom, *Engineering and Science*, **23**(5), pp. 22–36.

FILONOV-D. S., KRASNOK-A. E., SLOBOZHANYUK-A. P., KAPITANOVA-P. V., NENASHEVA-E. A., KIVSHAR-Y. S., AND BELOV-P. A. (2012). Experimental verification of the concept of all-dielectric nanoantennas, *Applied Physics Letters*, **100**(20), art. no. 201113.

FLEMING-J., LIN-S., EL-KADY-I., BISWAS-R., AND HO-K. (2002). All-metallic three-dimensional photonic crystals with a large infrared bandgap, *Nature*, **417**(6884), pp. 52–55.

FU-C., AND ZHANG-Z. M. (2009). Thermal radiative properties of metamaterials and other nanostructured materials: A review, *Frontiers of Energy and Power Engineering in China*, **3**(1), pp. 11–26.

FU-Z., GAN-Q., GAO-K., PAN-Z., AND BARTOLI-F. J. (2008). Numerical investigation of a bidirectional wave coupler based on plasmonic bragg gratings in the near infrared domain, *Journal of Lightwave Technology*, **26**(22), pp. 3699–3703.

GAN-Q., FU-Z., DING-Y. J., AND BARTOLI-F. J. (2007). Bidirectional subwavelength slit splitter for thz surface plasmons, *Optics Express*, **15**(26), pp. 18050–18055.

GE-Y., ESSELLE-K. P., AND BIRD-T. S. (2006). A wideband probe-fed stacked dielectric resonator antenna, *Microwave and Optical Technology Letters*, **48**(8), pp. 1630–1633.

GINN-J., SHELTON-D., KRENZ-P., LAIL-B., AND BOREMAN-G. (2010). Polarized infrared emission using frequency selective surfaces, *Optics Express*, **18**(5), pp. 4557–4563.

GRANQVIST-C., AND HJORTSBERG-A. (1981). Radiative cooling to low temperatures: General considerations and application to selectively emitting sio films, *Journal of Applied Physics*, **52**(6), pp. 4205–4220.

GREEN-M. A. (1990). Intrinsic concentration, effective densities of states, and effective mass in silicon, *Journal of Applied Physics*, **67**(6), pp. 2944–2954.

GREFFET-J.-J., CARMINATI-R., JOULAIN-K., MULET-J.-P., MAINGUY-S., AND CHEN-Y. (2002). Coherent emission of light by thermal sources, *Nature*, **416**(6876), pp. 61–64.

GROSSO-G., AND PASTORI PARRAVICINI-G. (2000). *Solid State Physics*, San Diego, Academic Press.

GUO-R., RUSAK-E., STAUDE-I., DOMINGUEZ-J., DECKER-M., ROCKSTUHL-C., BRENER-I., NESHEV-D. N., AND KIVSHAR-Y. S. (2016). Multipolar coupling in hybrid metal-dielectric metasurfaces, *ACS Photonics*, **3**(3), pp. 349–353.

GUO-Y., AND JACOB-Z. (2013). Thermal hyperbolic metamaterials, *Optics Express*, **21**(12), pp. 15014–15019.

GUTRUF-P., SHAH-C. M., WALIA-S., NILI-H., ZOOLFAKAR-A. S., KARNUTSCH-C., KALANTAR-ZADEH-K., SRIRAM-S., AND BHASKARAN-M. (2013). Transparent functional oxide stretchable electronics: micro-tectonics enabled high strain electrodes, *NPG Asia Materials*, **5**(9), p. e62.

GUTRUF-P., ZELLER-E., WALIA-S., NILI-H., SRIRAM-S., AND BHASKARAN-M. (2015). Stretchable and tunable microtectonic zno-based sensors and photonics, *Small*, **11**(35), pp. 4532–4539.

GUTRUF-P., ZOU-C., WITHAYACHUMNANKUL-W., BHASKARAN-M., SRIRAM-S., AND FUMEAUX-C. (2016). Mechanically tunable dielectric resonator metasurfaces at visible frequencies, *ACS Nano*, **10**(1), pp. 133–141.

HAO-F., SONNEFRAUD-Y., DORPE-P. V., MAIER-S. A., HALAS-N. J., AND NORDLANDER-P. (2008). Symmetry breaking in plasmonic nanocavities: subradiant LSPR sensing and a tunable Fano resonance, *Nano Letters*, **8**(11), pp. 3983–3988.

HAO-J., WANG-J., LIU-X., PADILLA-W. J., ZHOU-L., AND QIU-M. (2010). High performance optical absorber based on a plasmonic metamaterial, *Applied Physics Letters*, **96**(25), art. no. 251104.

HAUS-H. A. (1983). *Waves and Fields in Optoelectronics*, Prentice Hall.

HEADLAND-D., CARRASCO-E., NIRANTAR-S., WITHAYACHUMNANKUL-W., GUTRUF-P., SCHWARZ-J., ABBOTT-D., BHASKARAN-M., SRIRAM-S., PERRUISSEAU-CARRIER-J., AND FUMEAUX-C. (2016). Dielectric resonator reflectarray as high-efficiency non-uniform terahertz metasurface, *ACS Photonics*, **3**(6), pp. 1019–1026.

HEADLAND-D., NIRANTAR-S., WITHAYACHUMNANKUL-W., GUTRUF-P., ABBOTT-D., BHASKARAN-M., FUMEAUX-C., AND SRIRAM-S. (2015). Terahertz magnetic mirror realized with dielectric resonator antennas, *Advanced Materials*, **27**(44), pp. 7137–7144.

HEDAYATI-M. K., JAVAHERIRAHIM-M., MOZOONI-B., ABDELAZIZ-R., TAVASSOLIZADEH-A., CHAKRAVADHANULA-V. S. K., ZAPOROJTCHENKO-V., STRUNKUS-T., FAUPEL-F., AND ELBAHRI-M. (2011). Design of a perfect black absorber at visible frequencies using plasmonic metamaterials, *Advanced Materials*, **23**(45), pp. 5410–5414.

HE-M.-D., LIU-J.-Q., GONG-Z.-Q., LI-S., AND LUO-Y.-F. (2012). Directional excitation of surface plasmon polaritons in structure of subwavelength metallic holes, *Optics Communications*, **285**(2), pp. 182–185.

HOLMGAAR-D-T., CHEN-Z., BOZHEVOLNYI-S. I., MARKEY-L., DEREUX-A., KRASAVIN-A. V., AND ZAYATS-A. V. (2009). Wavelength selection by dielectric-loaded plasmonic components, *Applied Physics Letters*, **94**(5), art. no. 051111.

HOSSAIN-M., AND GU-M. (2016). Radiative cooling: Principles, progress, and potentials, *Advanced Science*, **3**, art. no. 1500360.

HOSSAIN-M. M., JIA-B., AND GU-M. (2015). A metamaterial emitter for highly efficient radiative cooling, *Advanced Optical Materials*, **3**(8), pp. 1047–1051.

HUANG-L., CHEN-X., MÜHLENBERND-H., ZHANG-H., CHEN-S., BAI-B., TAN-Q., JIN-G., CHEAH-K.-W., QIU-C.-W., LI-J., ZENTGRAF-T., AND ZHANG-S. (2013). Three-dimensional optical holography using a plasmonic metasurface, *Nature Communications*, **4**, art. no. 2808.

HUANG-X., AND BRONGERSMA-M. L. (2013). Compact aperiodic metallic groove arrays for unidirectional launching of surface plasmons, *Nano Letters*, **13**(11), pp. 5420–5424.

HUTLEY-M. C., AND MAYSTRE-D. (1976). The total absorption of light by a diffraction grating, *Optics Communications*, **19**(3), pp. 431–436.

INOUE-T., DE ZOYSA-M., ASANO-T., AND NODA-S. (2013). Single-peak narrow-bandwidth mid-infrared thermal emitters based on quantum wells and photonic crystals, *Applied Physics Letters*, **102**(19), art. no. 191110.

GEMINI OBSERVATORY (1992). IR Transmission Spectra, `http://www.gemini.edu/sciops/telescopes-and-sites/observing-condition-constraints/ir-transmission-spectra`. Accessed: July 2016.

ITTIPIBOON-A., CUHACI-M., MONGIA-R., BHARTIA-P., AND ANTAR-Y. (1993). Aperture fed rectangular and triangular dielectric resonators for use as magnetic dipole antennas, *Electronics Letters*, **29**(23), pp. 2001–2002.

JACKSON-J. D. (1999). *Classical Electrodynamics*, Wiley.

KAMALI-S. M., ARBABI-A., ARBABI-E., HORIE-Y., AND FARAON-A. (2016a). Decoupling optical function and geometrical form using conformal flexible dielectric metasurfaces, *Nature Communications*, **7**, art. no. 11618.

KAMALI-S. M., ARBABI-E., ARBABI-A., HORIE-Y., AND FARAON-A. (2016b). Highly tunable elastic dielectric metasurface lenses, *arXiv preprint arXiv:1604.03597*.

KARVOUNIS-A., GHOLIPOUR-B., MACDONALD-K. F., AND ZHELUDEV-N. I. (2016). All-dielectric phase-change reconfigurable metasurface, *arXiv preprint arXiv:1604.01330*.

KATS-M. A., BLANCHARD-R., GENEVET-P., AND CAPASSO-F. (2013). Nanometre optical coatings based on strong interference effects in highly absorbing media, *Nature Materials*, **12**(1), pp. 20–24.

KAURANEN-M., AND ZAYATS-A. V. (2012). Nonlinear plasmonics, *Nature Photonics*, **6**(11), pp. 737–748.

KHORASANINEJAD-M., AIETA-F., KANHAIYA-P., KATS-M. A., GENEVET-P., ROUSSO-D., AND CAPASSO-F. (2015). Achromatic metasurface lens at telecommunication wavelengths, *Nano Letters*, **15**(8), pp. 5358–5362.

KHORASANINEJAD-M., CHEN-W. T., DEVLIN-R. C., OH-J., ZHU-A. Y., AND CAPASSO-F. (2016). Metalenses at visible wavelengths: Diffraction-limited focusing and subwavelength resolution imaging, *Science*, **352**(6290), pp. 1190–1194.

KHUNSIN-W., BRIAN-B., DORFMULLER-J., ESSLINGER-M., VOGELGESANG-R., ETRICH-C., ROCKSTUHL-C., DMITRIEV-A., AND KERN-K. (2011). Long-distance indirect excitation of nanoplasmonic resonances, *Nano Letters*, **11**(7), pp. 2765–2769.

KILDISHEV-A. V., BOLTASSEVA-A., AND SHALAEV-V. M. (2013). Planar photonics with metasurfaces, *Science*, **339**(6125), art. no. 1232009.

KINGSLEY-S., AND O'KEEFE-S. G. (1999). Beam steering and monopulse processing of probe-fed dielectric resonator antennas, *IEE Proceedings - Radar, Sonar and Navigation*, **146**(3), pp. 121–125.

KIRCHAIN-R., AND KIMERLING-L. (2007). A roadmap for nanophotonics, *Nature Photonics*, **1**(6), pp. 303–305.

KIRCHHOFF-G. (1860). Ueber das verhältniss zwischen dem emissionsvermögen und dem absorptionsvermögen der körper für wärme und licht, *Annalen der Physik*, **185**(2), pp. 275–301.

KISHK-A. A. (2005). Experimental study of broadband embedded dielectric resonator antennas excited by a narrow slot, *IEEE Antennas and Wireless Propagation Letters*, **4**, pp. 79–81.

KISHK-A. A., AHN-B., AND KAJFEZ-D. (1989). Broadband stacked dielectric resonator antennas, *Electronics Letters*, **25**(18), pp. 1232–1233.

KLEIN-L. J., HAMANN-H. F., AU-Y.-Y., AND INGVARSSON-S. (2008). Coherence properties of infrared thermal emission from heated metallic nanowires, *Applied Physics Letters*, **92**(21), art. no. 213102.

KNEIPP-K., WANG-Y., KNEIPP-H., PERELMAN-L. T., ITZKAN-I., DASARI-R. R., AND FELD-M. S. (1997). Single molecule detection using surface-enhanced Raman scattering (SERS), *Physical Review Letters*, **78**(9), art. no. 1667.

KRANENBURG-R. A., LONG-S. A., AND WILLIAMS-J. T. (1991). Coplanar waveguide excitation of dielectric resonator antennas, *IEEE Transactions on Antennas and Propagation*, **39**, pp. 119–122.

KRANENBURG-R., AND LONG-S. (1988). Microstrip transmission line excitation of dielectric resonator antennas, *Electronics Letters*, **24**(18), pp. 1156–1157.

KRISHNAMOORTHY-H. N., ZHOU-Y., RAMANATHAN-S., NARIMANOV-E., AND MENON-V. M. (2014). Tunable hyperbolic metamaterials utilizing phase change heterostructures, *Applied Physics Letters*, **104**(12), art. no. 121101.

KUTTGE-M., DE ABAJO-F. J. G., AND POLMAN-A. (2009). How grooves reflect and confine surface plasmon polaritons, *Optics Express*, **17**(12), pp. 10385–10392.

KUZNETSOV-A. I., MIROSHNICHENKO-A. E., FU-Y. H., ZHANG-J., AND LUKYANCHUK-B. (2012). Magnetic light, *Scientific Reports*, **2**, art. no. 492.

KUZNETSOV-V. N., AND SERPONE-N. (2009). On the origin of the spectral bands in the visible absorption spectra of visible-light-active TiO_2 specimens analysis and assignments, *The Journal of Physical Chemistry C*, **113**(34), pp. 15110–15123.

LAI-Q., ALMPANIS-G., FUMEAUX-C., BENEDICKTER-H., AND VAHLDIECK-R. (2008). Comparison of the radiation efficiency for the dielectric resonator antenna and the microstrip antenna at ka band, *IEEE Transactions on Antennas and Propagation*, **56**(11), pp. 3589–3592.

LANDY-N., SAJUYIGBE-S., MOCK-J., SMITH-D., AND PADILLA-W. (2008). Perfect metamaterial absorber, *Physical Review Letters*, **100**(20), art. no. 207402.

LEHMUS-O., OLLIKAINEN-J., AND VAINIKAINEN-P. (1999). Characteristics of half-volume DRAs with different permittivities, *Antennas and Propagation Society International Symposium, 1999. IEEE*, **1**, IEEE, pp. 22–25.

LEUNG-K., AND LEUNG-C. (2003). Wideband dielectric resonator antenna excited by cavity-backed circular aperture with microstrip tuning fork, *Electronics Letters*, **39**(14), p. 1033–1035.

LEUNG-K., CHOW-K., LUK-K. M., AND YUNG-E. (1997). Low-profile circular disk DR antenna of very high permittivity excited by a microstripline, *Electronics Letters*, **33**(12), pp. 1004–1005.

LEUNG-K., LUK-K. M., AND YUNG-E. (1994). Spherical cap dielectric resonator antenna using aperture coupling, *Electronics Letters*, **30**(17), pp. 1366–1367.

LI-B., AND LEUNG-K. W. (2005). Strip-fed rectangular dielectric resonator antennas with/without a parasitic patch, *IEEE Transactions on Antennas and Propagation*, **53**(7), pp. 2200–2207.

LI-J., SHAH-C. M., WITHAYACHUMNANKUL-W., UNG-B. S.-Y., MITCHELL-A., SRIRAM-S., BHASKARAN-M., CHANG-S., AND ABBOTT-D. (2013). Mechanically tunable terahertz metamaterials, *Applied Physics Letters*, **102**(12), art. no. 121101.

LIN-J., MUELLER-J. B., WANG-Q., YUAN-G., ANTONIOU-N., YUAN-X.-C., AND CAPASSO-F. (2013). Polarization-controlled tunable directional coupling of surface plasmon polaritons, *Science*, **340**(6130), pp. 331–334.

LIU-N., LIU-H., ZHU-S., AND GIESSEN-H. (2009). Stereometamaterials, *Nature Photonics*, **3**(3), pp. 157–162.

LIU-N., MESCH-M., WEISS-T., HENTSCHEL-M., AND GIESSEN-H. (2010). Infrared perfect absorber and its application as plasmonic sensor, *Nano Letters*, **10**(7), pp. 2342–2348.

LIU-S., IHLEFELD-J. F., DOMINGUEZ-J., GONZALES-E. F., BOWER-J. E., BURCKEL-D. B., SINCLAIR-M. B., AND BRENER-I. (2013). Realization of tellurium-based all dielectric optical metamaterials using a multi-cycle deposition-etch process, *Applied Physics Letters*, **102**(16), art. no. 161905.

LIU-S., SINCLAIR-M. B., SARAVI-S., KEELER-G. A., YANG-Y., RENO-J., PEAKE-G. M., SETZPFANDT-F., STAUDE-I., PERTSCH-T., AND BRENER-I. (2016). Resonantly enhanced second-harmonic generation using III-V semiconductor all-dielectric metasurfaces, *Nano Letters*, **16**(9), pp. 5426–5432.

LIU-X., TYLER-T., STARR-T., STARR-A. F., JOKERST-N. M., AND PADILLA-W. J. (2011). Taming the blackbody with infrared metamaterials as selective thermal emitters, *Physical Review Letters*, **107**(4), art. no. 045901.

LIU-Y., PALOMBA-S., PARK-Y., ZENTGRAF-T., YIN-X., AND ZHANG-X. (2012). Compact magnetic antennas for directional excitation of surface plasmons, *Nano Letters*, **12**(9), pp. 4853–4858.

LI-Z., PALACIOS-E., BUTUN-S., AND AYDIN-K. (2015). Visible-frequency metasurfaces for broadband anomalous reflection and high-efficiency spectrum splitting, *Nano Letters*, **15**(3), pp. 1615–1621.

LONG-S. A., MCALLISTER-M. W., AND SHEN-L. C. (1983). The resonant cylindrical dielectric cavity antenna, *IEEE Transactions on Antennas and Propagation*, **31**, pp. 406–412.

LÓPEZ-TEJEIRA-F., RODRIGO-S. G., MARTÍN-MORENO-L., GARCÍA-VIDAL-F. J., DEVAUX-E., EBBESEN-T. W., KRENN-J. R., RADKO-I., BOZHEVOLNYI-S. I., GONZÁLEZ-M. U., WEEBER-J. C., AND DEREUX-A. (2007). Efficient unidirectional nanoslit couplers for surface plasmons, *Nature Physics*, **3**(5), pp. 324–328.

LU-C., HU-X., YANG-H., AND GONG-Q. (2013). Ultrawide-band unidirectional surface plasmon polariton launchers, *Advanced Optical Materials*, **1**(11), pp. 792–797.

LUK-K. M., LEUNG-K. W., LUK-K., AND LEUNG-K. (2002). *Dielectric Resonator Antennas*, Research Studies Press.

LUK'YANCHUK-B., ZHELUDEV-N. I., MAIER-S. A., HALAS-N. J., NORDLANDER-P., GIESSEN-H., AND CHONG-C. T. (2010). The Fano resonance in plasmonic nanostructures and metamaterials, *Nature Materials*, **9**(9), pp. 707–715.

MAIER-S. A. (2007). *Plasmonics: Fundamentals and Applications*, Springer Science & Business Media.

MAIER-S. A., KIK-P. G., ATWATER-H. A., MELTZER-S., HAREL-E., KOEL-B. E., AND REQUICHA-A. A. (2003). Local detection of electromagnetic energy transport below the diffraction limit in metal nanoparticle plasmon waveguides, *Nature Materials*, **2**(4), pp. 229–232.

MAILLOUX-R. J. (2005). *Phased Array Antenna Handbook*, Vol. 2, Artech House Boston.

MARANGOS-J. P. (1998). Electromagnetically induced transparency, *Journal of Modern Optics*, **45**(3), pp. 471–503.

MARK-J. E. (2009). *Polymer Data Handbook*, Oxford University Press.

MARQUART-C., BOZHEVOLNYI-S., AND LEOSSON-K. (2005). Near-field imaging of surface plasmon-polariton guiding in band gap structures at telecom wavelengths, *Optics Express*, **13**(9), pp. 3303–3309.

MASON-J., SMITH-S., AND WASSERMAN-D. (2011). Strong absorption and selective thermal emission from a mid-infrared metamaterial, *Applied Physics Letters*, **98**(24), art. no. 241105.

MAYO-M., SIEGEL-R., NARAYANASAMY-A., AND NIX-W. (1990). Mechanical properties of nanophase TiO_2 as determined by nanoindentation, *Journal of Materials Research*, **5**(05), pp. 1073–1082.

MCALLISTER-M., AND LONG-S. A. (1984). Resonant hemispherical dielectric antenna, *Electronics Letters*, **20**(16), pp. 657–659.

MCALLISTER-M., LONG-S. A., AND CONWAY-G. (1983). Rectangular dielectric resonator antenna, *Electronics Letters*, **19**(6), pp. 218–219.

MEINZER-N., BARNES-W. L., AND HOOPER-I. R. (2014). Plasmonic meta-atoms and metasurfaces, *Nature Photonics*, **8**(12), pp. 889–898.

MIAS-C., WEBB-J., AND FERRARI-L. (1999). Finite element modelling of electromagnetic waves in doubly and triply periodic structures, *IEE Proceedings-Optoelectronics*, **146**(2), pp. 111–118.

MILLYARD-M. G., HUANG-F. M., WHITE-R., SPIGONE-E., KIVIOJA-J., AND BAUMBERG-J. J. (2012). Stretch-induced plasmonic anisotropy of self-assembled gold nanoparticle mats, *Applied Physics Letters*, **100**(7), art. no. 073101.

MOITRA-P., SLOVICK-B. A., YU-Z. G., KRISHNAMURTHY-S., AND VALENTINE-J. (2014). Experimental demonstration of a broadband all-dielectric metamaterial perfect reflector, *Applied Physics Letters*, **104**(17), art. no. 171102.

MOLESKY-S., DEWALT-C. J., AND JACOB-Z. (2013). High temperature epsilon-near-zero and epsilon-near-pole metamaterial emitters for thermophotovoltaics, *Optics Express*, **21**(101), pp. A96–A110.

MONGIA-R. K., AND BHARTIA-P. (1994). Dielectric resonator antennas - a review and general design relations for resonant frequency and bandwidth, *International Journal of Microwave and Millimeter-Wave Computer-Aided Engineering*, **4**(3), pp. 230–247.

MONTICONE-F., ESTAKHRI-N. M., AND ALÙ-A. (2013). Full control of nanoscale optical transmission with a composite metascreen, *Physical Review Letters*, **110**(20), art. no. 203903.

MORIN-D. (2008). *Introduction to Classical Mechanics: with Problems and Solutions*, Cambridge University Press.

MUNK-B. A. (2000). Frequency selective surfaces: Theory and design.

NAGPAL-P., HAN-S. E., STEIN-A., AND NORRIS-D. J. (2008). Efficient low-temperature thermophotovoltaic emitters from metallic photonic crystals, *Nano Letters*, **8**(10), pp. 3238–3243.

NEUDECK-P. G., OKOJIE-R. S., AND CHEN-L.-Y. (2002). High-temperature electronics - a role for wide bandgap semiconductors?, *Proceedings of the IEEE*, **90**(6), pp. 1065–1076.

NEUGEBAUER-M., BAUER-T., BANZER-P., AND LEUCHS-G. (2014). Polarization tailored light driven directional optical nanobeacon, *Nano Letters*, **14**(5), pp. 2546–2551.

NISAR-A., AFZULPURKAR-N., MAHAISAVARIYA-B., AND TUANTRANONT-A. (2008). Multifield analysis using multiple code coupling of a MEMS based micropump with biocompatible membrane materials for biomedical applications, *2008 International Conference on BioMedical Engineering and Informatics*, **1**, IEEE, pp. 531–535.

NIU-T., WITHAYACHUMNANKUL-W., UNG-B. S.-Y., MENEKSE-H., BHASKARAN-M., SRIRAM-S., AND FUMEAUX-C. (2013). Experimental demonstration of reflectarray antennas at terahertz frequencies, *Optics Express*, **21**(3), pp. 2875–2889.

NI-X., KILDISHEV-A. V., AND SHALAEV-V. M. (2013). Metasurface holograms for visible light, *Nature Communications*, **4**, art. no. 2807.

NOVOTNY-L., AND HECHT-B. (2012). *Principles of Nano-optics*, Cambridge University Press.

NOVOTNY-L., AND VAN HULST-N. (2011). Antennas for light, *Nature Photonics*, **5**(2), pp. 83–90.

OTTERMANN-C., KUSCHNEREIT-R., ANDERSON-O., HESS-P., AND BANGE-K. (1996). Young's modulus and density of thin TiO_2 films produced by different methods, *MRS Proceedings*, Vol. 436, Cambridge University Press, art. no. 251.

OU-J.-Y., PLUM-E., JIANG-L., AND ZHELUDEV-N. I. (2011). Reconfigurable photonic metamaterials, *Nano Letters*, **11**(5), pp. 2142–2144.

PALIK-E. D. (1998). *Handbook of Optical Constants of Solids*, Vol. 3, Academic Press.

PALMER-C. A., AND LOEWEN-E. G. (2005). *Diffraction Grating Handbook*, Newport Corporation Springfield, Ohio, USA.

PENDRY-J. B. (2000). Negative refraction makes a perfect lens, *Physical Review Letters*, **85**(18), art. no. 3966.

PERRON-A., DENIDNI-T. A., AND SEBAK-A.-R. (2009). High-gain hybrid dielectric resonator antenna for millimeter-wave applications: Design and implementation, *IEEE Transactions on Antennas and Propagation*, **57**(10), pp. 2882–2892.

PETOSA-A. (2007). *Dielectric Resonator Antenna Handbook*, Artech House Publishers.

PLANCK-M. (1901). Ueber das gesetz der energieverteilung im normalspectrum, *Annalen der physik*, **309**(3), pp. 553–563.

POLYAKOV-A., THOMPSON-K., DHUEY-S., OLYNICK-D., CABRINI-S., SCHUCK-P., AND PADMORE-H. (2012). Plasmon resonance tuning in metallic nanocavities, *Scientific Reports*, **2**, art. no. 933.

PORS-A., NIELSEN-M. G., ERIKSEN-R. L., AND BOZHEVOLNYI-S. I. (2013). Broadband focusing flat mirrors based on plasmonic gradient metasurfaces, *Nano Letters*, **13**(2), pp. 829–834.

POUTRINA-E., HUANG-D., AND SMITH-D. R. (2010). Analysis of nonlinear electromagnetic metamaterials, *New Journal of Physics*, **12**(9), art. no. 093010.

POWELL-D. A., HANNAM-K., SHADRIVOV-I. V., AND KIVSHAR-Y. S. (2011). Near-field interaction of twisted split-ring resonators, *Physical Review B*, **83**(23), art. no. 235420.

POWELL-D. A., LAPINE-M., GORKUNOV-M. V., SHADRIVOV-I. V., AND KIVSHAR-Y. S. (2010). Metamaterial tuning by manipulation of near-field interaction, *Physical Review B*, **82**(15), art. no. 155128.

PRALLE-M., MOELDERS-N., MCNEAL-M., PUSCASU-I., GREENWALD-A., DALY-J., JOHNSON-E., GEORGE-T., CHOI-D., EL-KADY-I., AND BISWAS-R. (2002). Photonic crystal enhanced narrow-band infrared emitters, *Applied Physics Letters*, **81**(25), pp. 4685–4687.

PRASAD-P. N. (2004). *Nanophotonics*, John Wiley & Sons.

PRODAN-E., RADLOFF-C., HALAS-N. J., AND NORDLANDER-P. (2003). A hybridization model for the plasmon response of complex nanostructures, *Science*, **302**(5644), pp. 419–422.

PRYCE-I. M., AYDIN-K., KELAITA-Y. A., BRIGGS-R. M., AND ATWATER-H. A. (2010). Highly strained compliant optical metamaterials with large frequency tunability, *Nano Letters*, **10**(10), pp. 4222–4227.

PURCELL-E. M. (1946). Spontaneous emission probabilities at radio frequencies, *Physical Review*, **69**, art. no. 681.

PUSCASU-I., AND SCHAICH-W. L. (2008). Narrow-band, tunable infrared emission from arrays of microstrip patches, *Applied Physics Letters*, **92**(23), art. no. 233102.

PUSCASU-I., SCHAICH-W., AND BOREMAN-G. D. (2002). Resonant enhancement of emission and absorption using frequency selective surfaces in the infrared, *Infrared Physics & Technology*, **43**(2), pp. 101–107.

QU-C., MA-S., HAO-J., QIU-M., LI-X., XIAO-S., MIAO-Z., DAI-N., HE-Q., SUN-S., AND ZHOU-L. (2015). Tailor the functionalities of metasurfaces based on a complete phase diagram, *Physical Review Letters*, **115**(23), art. no. 235503.

RADKO-I. P., VOLKOV-V. S., BEERMANN-J., EVLYUKHIN-A. B., SØNDERGAARD-T., BOLTASSEVA-A., AND BOZHEVOLNYI-S. I. (2009). Plasmonic metasurfaces for waveguiding and field enhancement, *Laser & Photonics Reviews*, **3**(6), pp. 575–590.

REDDY-M., RAO-V. V., REDDY-B., SARADA-S. N., AND RAMESH-L. (2012). Thermal conductivity measurements of ethylene glycol water based TiO_2 nanofluids, *Nanoscience and Nanotechnology Letters*, **4**(1), pp. 105–109.

REPHAELI-E., AND FAN-S. (2009). Absorber and emitter for solar thermo-photovoltaic systems to achieve efficiency exceeding the shockley-queisser limit, *Optics Express*, **17**(17), pp. 15145–15159.

REPHAELI-E., RAMAN-A., AND FAN-S. (2013). Ultrabroadband photonic structures to achieve high-performance daytime radiative cooling, *Nano Letters*, **13**(4), pp. 1457–1461.

RICHTMYER-R. (1939). Dielectric resonators, *Journal of Applied Physics*, **10**(6), pp. 391–398.

RINNERBAUER-V., YENG-Y. X., CHAN-W. R., SENKEVICH-J. J., JOANNOPOULOS-J. D., SOLJAČIĆ-M., AND CELANOVIC-I. (2013). High-temperature stability and selective thermal emission of polycrystalline tantalum photonic crystals, *Optics Express*, **21**(9), pp. 11482–11491.

SAI-H., YUGAMI-H., KANAMORI-Y., AND HANE-K. (2003). Solar selective absorbers based on two-dimensional W surface gratings with submicron periods for high-temperature photothermal conversion, *Solar Energy Materials and Solar Cells*, **79**(1), pp. 35–49.

SALEH-B. E., TEICH-M. C., AND SALEH-B. E. (1991). *Fundamentals of Photonics*, Vol. 22, Wiley New York.

SAUTTER-J., STAUDE-I., DECKER-M., RUSAK-E., NESHEV-D. N., BRENER-I., AND KIVSHAR-Y. S. (2015). Active tuning of all-dielectric metasurfaces, *ACS Nano*, **9**(4), pp. 4308–4315.

SCHULLER-J. A., TAUBNER-T., AND BRONGERSMA-M. L. (2009). Optical antenna thermal emitters, *Nature Photonics*, **3**(11), pp. 658–661.

SEGHIR-R., AND ARSCOTT-S. (2015). Mechanically robust, electrically stable metal arrays on plasma-oxidized polydimethylsiloxane for stretchable technologies, *Journal of Applied Physics*, **118**(4), art. no. 045309.

SEO-M., KYOUNG-J., PARK-H., KOO-S., KIM-H.-S., BERNIEN-H., KIM-B. J., CHOE-J. H., AHN-Y. H., KIM-H.-T., PARK-N., PARK-Q.-H., AHN-K., AND KIM-D.-S. (2010). Active terahertz nanoantennas based on VO_2 phase transition, *Nano Letters*, **10**(6), pp. 2064–2068.

SERGEANT-N. P., PINCON-O., AGRAWAL-M., AND PEUMANS-P. (2009). Design of wide-angle solar-selective absorbers using aperiodic metal-dielectric stacks, *Optics Express*, **17**(25), pp. 22800–22812.

SERSIC-I., FRIMMER-M., VERHAGEN-E., AND KOENDERINK-A. F. (2009). Electric and magnetic dipole coupling in near-infrared split-ring metamaterial arrays, *Physical Review Letters*, **103**(21), art. no. 213902.

SHALAEV-V. M., AND KAWATA-S. (2006). *Nanophotonics with Surface Plasmons*, Elsevier.

SHARON-A., GLASBERG-S., ROSENBLATT-D., AND FRIESEM-A. (1997). Metal-based resonant grating waveguide structures, *Journal of Optical Society of America, A*, **14**(3), pp. 588–595.

SHCHERBAKOV-M. R., NESHEV-D. N., HOPKINS-B., SHOROKHOV-A. S., STAUDE-I., MELIK-GAYKAZYAN-E. V., DECKER-M., EZHOV-A. A., MIROSHNICHENKO-A. E., BRENER-I., FEDYANIN-A. A., AND KIVSHAR-Y. S. (2014). Enhanced third-harmonic generation in silicon nanoparticles driven by magnetic response, *Nano Letters*, **14**(11), pp. 6488–6492.

SHCHERBAKOV-M. R., SHOROKHOV-A. S., NESHEV-D. N., HOPKINS-B., STAUDE-I., MELIK-GAYKAZYAN-E. V., EZHOV-A. A., MIROSHNICHENKO-A. E., BRENER-I., FEDYANIN-A. A., AND KIVSHAR-Y. S. (2015a). Nonlinear interference and tailorable third-harmonic generation from dielectric oligomers, *ACS Photonics*, **2**(5), pp. 578–582.

SHCHERBAKOV-M. R., VABISHCHEVICH-P. P., SHOROKHOV-A. S., CHONG-K. E., CHOI-D.-Y., STAUDE-I., MIROSHNICHENKO-A. E., NESHEV-D. N., FEDYANIN-A. A., AND KIVSHAR-Y. S. (2015b). Ultrafast all-optical switching with magnetic resonances in nonlinear dielectric nanostructures, *Nano Letters*, **15**(10), pp. 6985–6990.

SINGH-R., CAO-W., AL-NAIB-I., CONG-L., WITHAYACHUMNANKUL-W., AND ZHANG-W. (2014). Ultrasensitive terahertz sensing with high-q fano resonances in metasurfaces, *Applied Physics Letters*, **105**(17), art. no. 171101.

SMITH-D. R., AND PENDRY-J. B. (2006). Homogenization of metamaterials by field averaging, *Journal of Optical Society of America, B*, **23**(3), pp. 391–403.

SMITH-D. R., PENDRY-J. B., AND WILTSHIRE-M. C. (2004). Metamaterials and negative refractive index, *Science*, **305**(5685), pp. 788–792.

SMITH-W. J. (1966). *Modern Optical Engineering*, Tata McGraw-Hill Education.

SØNDERGAARD-T., NOVIKOV-S. M., HOLMGAARD-T., ERIKSEN-R. L., BEERMANN-J., HAN-Z., PEDERSEN-K., AND BOZHEVOLNYI-S. I. (2012). Plasmonic black gold by adiabatic nanofocusing and absorption of light in ultra-sharp convex grooves, *Nature Communications*, **3**, art. no. 969.

SPINELLI-P., VERSCHUUREN-M., AND POLMAN-A. (2012). Broadband omnidirectional antireflection coating based on subwavelength surface mie resonators, *Nature Communications*, **3**, art. no. 692.

STAUDE-I., MIROSHNICHENKO-A. E., DECKER-M., FOFANG-N. T., LIU-S., GONZALES-E., DOMINGUEZ-J., LUK-T. S., NESHEV-D. N., BRENER-I., AND KIVSHAR-Y. S. (2013). Tailoring directional scattering through magnetic and electric resonances in subwavelength silicon nanodisks, *ACS Nano*, **7**(9), pp. 7824–7832.

STOCKMAN-M. I. (2011). Spaser action, loss compensation, and stability in plasmonic systems with gain, *Physical Review Letters*, **106**(15), art. no. 156802.

SUN-S., HE-Q., XIAO-S., XU-Q., LI-X., AND ZHOU-L. (2012a). Gradient-index meta-surfaces as a bridge linking propagating waves and surface waves, *Nature Materials*, **11**(5), pp. 426–431.

SUN-S., YANG-K.-Y., WANG-C.-M., JUAN-T.-K., CHEN-W. T., LIAO-C. Y., HE-Q., XIAO-S., KUNG-W.-T., GUO, GUANG-YU-L. Z., AND TSAI-D. P. (2012b). High-efficiency broadband anomalous reflection by gradient meta-surfaces, *Nano Letters*, **12**(12), pp. 6223–6229.

SZE-J.-Y., WONG-K.-L., AND HUANG-C.-C. (2003). Coplanar waveguide-fed square slot antenna for broadband circularly polarized radiation, *IEEE Transactions on Antennas and Propagation*, **51**(8), pp. 2141–2144.

TAM-M. T., AND MURCH-R. D. (1999). Compact circular sector and annular sector dielectric resonator antennas, *IEEE Transactions on Antennas and Propagation*, **47**(5), pp. 837–842.

TAN-W.-C., PREIST-T., SAMBLES-J., AND WANSTALL-N. (1999). Flat surface-plasmon-polariton bands and resonant optical absorption on short-pitch metal gratings, *Physical Review B*, **59**(19), art. no. 12661.

TAO-H., LANDY-N. I., BINGHAM-C. M., ZHANG-X., AVERITT-R. D., AND PADILLA-W. J. (2008). A metamaterial absorber for the terahertz regime: Design, fabrication and characterization, *Optics Express*, **16**(10), pp. 7181–7188.

THORESON-M. D., LIU-Z., CHETTIAR-U. K., NYGA-P., KILDISHEV-A. V., DRACHEV-V. P., PACK-M. V., AND SHALAEV-V. M. (2010). Studies on metal-dielectric plasmonic structures, *Sandia Report SAND2009-7034, Sandia National Laboratories, United States*, **41**(20), pp. 1–68.

TUCKER-E., DARCHANGEL-J., RASCHKE-M. B., AND BOREMAN-G. (2015). Near-field investigation of the effect of the array edge on the resonance of loop frequency selective surface elements at mid-infrared wavelengths, *Optics Express*, **23**(9), pp. 10974–10985.

VECCHI-G., GIANNINI-V., AND RIVAS-J. G. (2009). Shaping the fluorescent emission by lattice resonances in plasmonic crystals of nanoantennas, *Physical Review Letters*, **102**(14), art. no. 146807.

WANG-Z., CHIAU-C., CHEN-X., COLLINS-B., AND KINGSLEY-S. (2006). A miniature broadband dielectric resonator antenna (dra) operating at 2.4 GHz, *IEEE International Workshop on Antenna Technology: small Antennas and Novel Metamaterials*, pp. 104–107.

WATTS-C. M., LIU-X., AND PADILLA-W. J. (2012). Metamaterial electromagnetic wave absorbers, *Advanced Materials*, **24**(23), pp. OP98–OP120.

WEEBER-J.-C., LACROUTE-Y., AND DEREUX-A. (2003). Optical near-field distributions of surface plasmon waveguide modes, *Physical Review B*, **68**(11), art. no. 115401.

WILD-B., CAO-L., SUN-Y., KHANAL-B. P., ZUBAREV-E. R., GRAY-S. K., SCHERER-N. F., AND PELTON-M. (2012). Propagation lengths and group velocities of plasmons in chemically synthesized gold and silver nanowires, *ACS Nano*, **6**(1), pp. 472–482.

WILLETS-K. A., AND VAN DUYNE-R. P. (2007). Localized surface plasmon resonance spectroscopy and sensing, *Annual Review of Physical Chemistry*, **58**, pp. 267–297.

WITHAYACHUMNANKUL-W., FUMEAUX-C., AND ABBOTT-D. (2012). Near-field interactions in electric inductive - capacitive resonators for metamaterials, *Journal of Physics D: Applied Physics*, **45**(48), art. no. 485101.

WITHAYACHUMNANKUL-W., SHAH-C. M., FUMEAUX-C., UNG-B. S.-Y., PADILLA-W. J., BHASKARAN-M., ABBOTT-D., AND SRIRAM-S. (2014). Plasmonic resonance toward terahertz perfect absorbers, *ACS Photonics*, **1**(7), pp. 625–630.

WOOD-R. W. (1902). On a remarkable case of uneven distribution of light in a diffraction grating spectrum, *Proceedings of the Physical Society of London*, **18**(1), pp. 269–275.

WU-M. C., SOLGAARD-O., AND FORD-J. E. (2006). Optical mems for lightwave communication, *Journal of Lightwave Technology*, **24**(12), pp. 4433–4454.

XIA-Y., KIM-E., ZHAO-X.-M., ROGERS-J. A., PRENTISS-M., AND WHITESIDES-G. M. (1996). Complex optical surfaces formed by replica molding against elastomeric masters, *Science*, **273**(5273), pp. 347–349.

XI-Z., LU-Y., YU-W., WANG-P., AND MING-H. (2014). Unidirectional surface plasmon launcher: rotating dipole mimicked by optical antennas, *Journal of Optics*, **16**(10), art. no. 105002.

YANG-Y., KRAVCHENKO-I. I., BRIGGS-D. P., AND VALENTINE-J. (2014a). All-dielectric metasurface analogue of electromagnetically induced transparency, *Nature Communications*, **5**, art. no. 5753.

YANG-Y., WANG-W., MOITRA-P., KRAVCHENKO-I. I., BRIGGS-D. P., AND VALENTINE-J. (2014b). Dielectric meta-reflectarray for broadband linear polarization conversion and optical vortex generation, *Nano Letters*, **14**(3), pp. 1394–1399.

YAO-Y., SHANKAR-R., KATS-M. A., SONG-Y., KONG-J., LONCAR-M., AND CAPASSO-F. (2014). Electrically tunable metasurface perfect absorbers for ultrathin mid-infrared optical modulators, *Nano Letters*, **14**(11), pp. 6526–6532.

YE-F., BURNS-M. J., AND NAUGHTON-M. J. (2014). Symmetry-broken metamaterial absorbers as reflectionless directional couplers for surface plasmon polaritons in the visible range, *Advanced Optical Materials*, **2**(10), pp. 957–965.

YIN-L., VLASKO-VLASOV-V., RYDH-A., PEARSON-J., WELP-U., CHANG-S.-H., GRAY-S., SCHATZ-G. C., BROWN-D., AND KIMBALL-C. W. (2004). Surface plasmons at single nanoholes in Au films, *Applied Physics Letters*, **85**(3), pp. 467–469.

YU-N., AND CAPASSO-F. (2014). Flat optics with designer metasurfaces, *Nature Materials*, **13**(2), pp. 139–150.

YU-N., GENEVET-P., KATS-M. A., AIETA-F., TETIENNE-J.-P., CAPASSO-F., AND GABURRO-Z. (2011). Light propagation with phase discontinuities: generalized laws of reflection and refraction, *Science*, **334**(6054), pp. 333–337.

ZAYATS-A. V., SMOLYANINOV-I. I., AND MARADUDIN-A. A. (2005). Nano-optics of surface plasmon polaritons, *Physics Reports*, **408**(3), pp. 131–314.

ZHANG-J., OU-J., MACDONALD-K., AND ZHELUDEV-N. (2012). Optical response of plasmonic relief meta-surfaces, *Journal of Optics*, **14**(11), art. no. 114002.

ZHANG-S., GENOV-D. A., WANG-Y., LIU-M., AND ZHANG-X. (2008). Plasmon-induced transparency in metamaterials, *Physical Review Letters*, **101**(4), art. no. 047401.

ZHELUDEV-N. I., AND KIVSHAR-Y. S. (2012). From metamaterials to metadevices, *Nature Materials*, **11**(11), pp. 917–924.

ZHU-L., KAPRAUN-J., FERRARA-J., AND CHANG-HASNAIN-C. J. (2015). Flexible photonic metastructures for tunable coloration, *Optica*, **2**(3), pp. 255–258.

ZOU-C., GUTRUF-P., WITHAYACHUMNANKUL-W., ZOU-L., BHASKARAN-M., SRIRAM-S., AND FUMEAUX-C. (2016). Nanoscale TiO_2 dielectric resonator absorbers, *Optics Letters*, **41**(15), pp. 3391–3394.

ZOU-C., WITHAYACHUMNANKUL-W., SHADRIVOV-I. V., KIVSHAR-Y. S., AND FUMEAUX-C. (2015a). Directional excitation of surface plasmons by dielectric resonators, *Physical Review B*, **91**(8), art. no. 085433.

ZOU-C., WITHAYACHUMNANKUL-W., ZOU-L., AND FUMEAUX-C. (2015b). Resonance breakdown of dielectric resonator antennas on ground plane at visible frequencies, *SPIE Micro+ Nano Materials, Devices, and Applications*, International Society for Optics and Photonics, pp. 966820–966820.

ZOU-L., WITHAYACHUMNANKUL-W., SHAH-C. M., MITCHELL-A., BHASKARAN-M., SRIRAM-S., AND FUMEAUX-C. (2013). Dielectric resonator nanoantennas at visible frequencies, *Optics Express*, **21**(1), pp. 1344–1352.

ZOU-L., WITHAYACHUMNANKUL-W., SHAH-C. M., MITCHELL-A., KLEMM-M., BHASKARAN-M., SRIRAM-S., AND FUMEAUX-C. (2014). Efficiency and scalability of dielectric resonator antennas at optical frequencies, *IEEE Photonics Journal*, **6**(4), pp. 1–10.